HIGH ENERGY DENSITY PROPULSION SYSTEMS AND SMALL ENGINE DYNAMOMETER

By

THOMAS HAYS

Bachelor of Science in Mechanical and Aerospace Engineering

Oklahoma State University

Stillwater, Oklahoma

2007

Submitted to the Faculty of the
Graduate College of the
Oklahoma State University
in partial fulfillment of
the requirements for
the Degree of
MASTER OF SCIENCE
July, 2009

HIGH ENERGY DENSITY PROPULSION SYSTEMS AND SMALL ENGINE DYNAMOMETER

Thesis Approved:

Dr. Andrew S. Arena

Thesis Adviser

Dr. Jamey D. Jacob

Dr. Richard L. Lowery

Dr. A. Gordon Emslie

Dean of the Graduate College

ACKNOWLEDGMENTS

Before any other, I must thank my parents for supporting me throughout my college career. They have encouraged me during my years at Oklahoma State to go beyond the minimum requirements of the program, and have provided endless support in pursuing that goal. Any student would have to pursue failure to find anything less than absolute success given the support my parents have offered through my life thus far.

There has been no greater contributor to my education at Oklahoma State University than my advisor Dr. Andrew Arena. Working for, and with him on the Dragonfly project gave me the confidence to challenge continually harder questions as my studies progressed. Not enough can be said for his ability to simplify both engineering problems, and contractual politics. The lessons learned in both areas will guide me for years to come wherever I may be.

I would also like to acknowledge Joseph Conner, whose work on small propeller dynamometers preceded this work on small scale engine dynamometers. The lessons learned from using his dynamometer were invaluable while designing and testing my own. His exemplary work surely saved many weeks of mistakes, and improved the final quality of the engine dynamometer.

Finally I must thank my friend and colleague Dustin Gamble. As a fellow ignorant undergraduate during the early years of our design build fly career, a partner in the dragonfly project, consulting friend during my capstone project, a coworker during my second internship, and most of all a friend. Dustin has always challenged me to work faster, longer, and more efficiently. His tenacity to get things working, and worry about the details later, is a large reason for the success of both the dragonfly and Pterosoar projects. His aerospace personality and drive can only be compared with Kelly, Paul, and Burt so I hope to see his career flourish to an equal extent.

TABLE OF CONTENTS

Chapter Page

Contents

LIST OF FIGURES

Figure Page

CHAPTER I

INTRODUCTION

How long, how far, and what can it carry are the three most important questions pertaining to aircraft. Range is nothing without payload, payload is useless without endurance, and endurance is pointless without range. Most current small unmanned aircraft are balanced in these areas, but suffers in all of them when compared to the performance of their larger brothers. Many designers blindly accept that small vehicles cannot fly as long or as far as full size aircraft, but this is simply not the case. This thesis focuses on the driving factor of aircraft performance, energy density. Making an optimal aircraft is simply solving a set of equations. Making a higher energy density propulsion system is expanding the capabilities of an entire class of aircraft.

This study begins with an overview of all feasible small aircraft energy systems. The systems are broken into three groups: direct energy, harvesting, and conversion type sources. The benefits and comprehensive energy densities are discussed. All necessary weights are considered when determining total system energy density. Finally the energy system data is compared on the same chart exposing the true capabilities of systems when compared to one another.

Next, a small engine dynamometer is constructed to study and verify the true energy density of small engines. The design of the dynamometer is discussed along with lessons learned during construction and testing of the device. Uncertainty, repeatability, and accuracy are all discussed and thoroughly proven. All sensors, data acquisition, data reduction techniques and equations are reviewed to provide any future user of the dynamometer a complete knowledge of its operating theory and calibration procedure. Finally test values for an assortment of engines are presented as examples of the dynamometers capability.

Lastly a conceptual study of small aircraft propelled by small, efficient engines is conducted to show the relative difference in performance based on the results of engine testing. Also, future improvements to the dynamometer and small engines in general are proposed to serve as a guide for future work toward actually creating one of the aircraft described in the conceptual study

The goal of this work is to do nothing short of redefine the capabilities of small aircraft. The base study has been done. A device for verifying theories has been created, tested, and verified. The path to a mature end product has been paid out in detail. And a taste of what is possible with mature small engine technology is discussed to keep one's eye on the prize of an aircraft that can fit in a standard car, prepared by a single person, and launched on a mission to circumnavigate the globe.

CHAPTER II

REVIEW OF LITERATURE

Menon Dynamometer

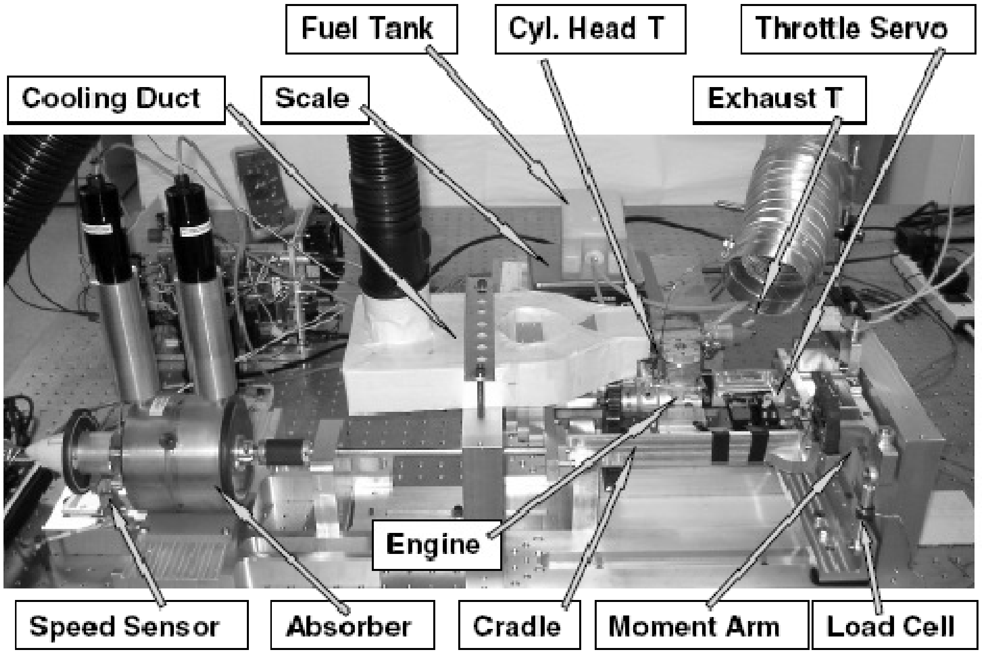

Figure 1 - Menon Dynamometer (Menon 2007)

The Menon Dynamometer is a hysteresis brake type dynamometer created for the purposes for gathering horsepower torque and fuel flow data on small engines. This dynamometer also detects airflow into the engine using a TSI 4021 mass flow meter which allows for scavenging measurements, and data presentation based on fuel to air ratio. The Menon Dynamometer uses a reaction torque cradle to pass engine torque into a rigidly mounted 5 lb capacity load cell. Because the load cell is rigidly mounted, the cradle must be locked down each time the engine passes through the resonant frequency of the rotating system or else the load cell will be destroyed. Also, because a 5 lb load cell is used to reduce the chance of overload, torque uncertainty rises rapidly and is stated as +- 2.5%. Overall power and torque measurements are stated to be accurate to +- 8.5 %. Overall U.S. Army Research Office funded Menon dynamometer is capable of delivering many types of high quality data thanks to its sophisticated sensors.

This dynamometer is also used in another publication regarding micro engines by Sookdeo. In this paper the moment arm based torque measurement system is replaced by correlating the output of a connected generator to true output horsepower. This method is inaccurate but necessary because of the large uncertainty of the load cell based system.

Korean Aerospace Research Institute Dynamometer

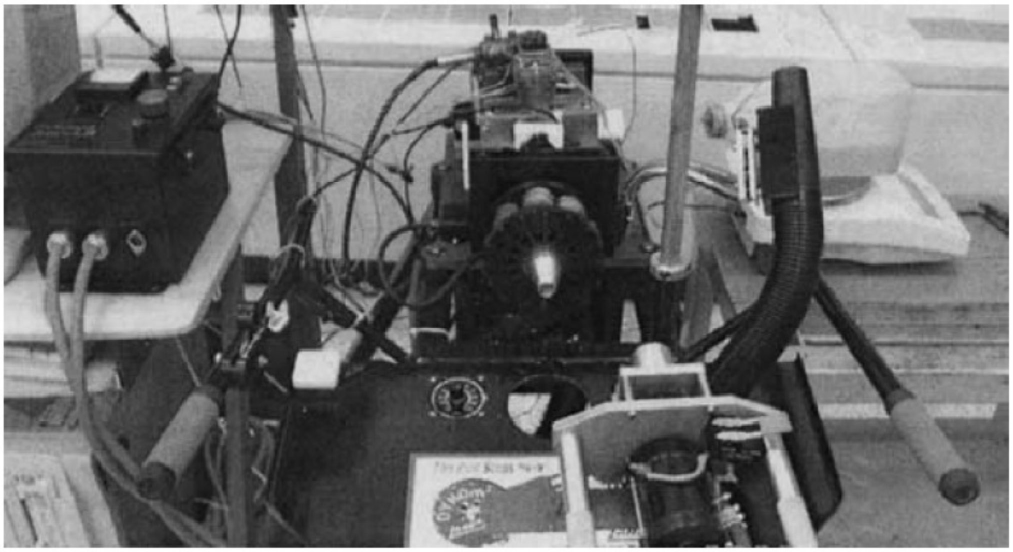

Figure 2 - Korean Dynamometer (Shin 2004)

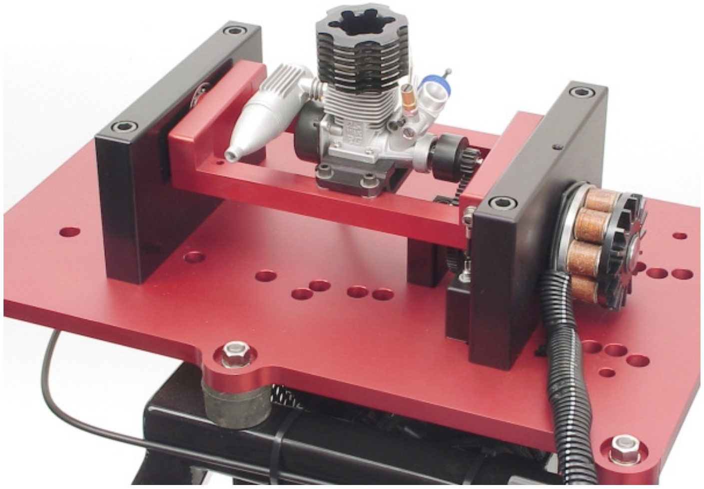

Figure 3 - Land and Sea Dynamometer

The dynamometer built by the Korean Aerospace Research Institute is an eddy current brake dynamometer making use of the land and sea dynamometer system. This system supports the engine in a cradle similar to the Menon dynamometer, and passes torque into a directly connected load cell. Most of the work done by Shin Et. Al. revolves around comparing engine test results with those predicted by a program developed at the Sloan automotive engine laboratory at MIT over many years. The software package predicted horsepower output as a function of RPM very well, but was considerably off when trying to compute BSFC. This dynamometer would have similar problems with cradle resonance destroying load cells. Additionally, the land and sea dynamometer has an entry cost of 13,500 dollars, which does not include the engine starter, computer, auxiliary sensors, and other accessories.

CHAPTER III

ENERGY SYSTEMS SURVEY

The overarching purpose of all studies and research conducted in this document is to increase the maximum performance envelope of small unmanned aircraft. With specific interest placed on endurance, range, and excess power in order of importance. A potential benefit study was conducted on the four main factors that determine performance of small aircraft, propulsive efficiency, profile drag, structural weight, and energy density.

The low subsonic speeds that most small aircraft fly at generally favors propellers to give maximum propulsive efficiency. This is a result of the increase in propulsive efficiency as the change in velocity across the thrust plane decreases. Ducted fan and turbojet UAV thrust systems create equivalent momentum differences with smaller radius thrust disks than propellers thus lowering their comparative propulsive efficiency at slow speed. A properly implemented low Reynolds number propeller can achieve cruise efficiencies of 70-80%, while full scale propellers make use of their higher operating Reynolds numbers to commonly reach efficiencies in the 80-90% range. The increased efficiency in transferring power to the flow both increases maximum power, and maximum endurance proportional to the change in efficiency. Therefore the best improvement that could be hoped for by conducting small aircraft propeller research would be a 10 to 20 percent increase in range, endurance, and maximum power. This increase is by no means negligible, and is in need of detailed and practical study.

The profile drag coefficient of small aircraft is generally much higher than man carrying craft for two reasons. First, the lower flight speed, and smaller scale, results in much lower Reynolds numbers which in turn increases drag. Secondly, the aerodynamics of small aircraft is often neglected in favor of electronic improvements. A general trend of adding fuel and increasing size instead of making the airplane more aerodynamically efficient results in most small aircraft having much higher drag than required. Application of previously proven aerodynamic theory to a sub-par aerodynamic design would hardly constitute a research project, so the possible improvement should be gauged against the state of the art, and not the aircraft drawings of electrical engineers. Many alternative aerodynamic techniques for boundary layer control would be especially suitable for low Reynolds number aircraft since their drag rise is primarily due to boundary layer effects. Suction, pulsing, electro-magneto-hydrodynamics, carefully placed boundary layer trips, and other methods have all been shown to reduce drag, but most consume power, and add weight to a system and as such may negate any benefit in reducing drag. The maximum expected reduction in profile drag could be between 20% and 50%, and would require a large amount of application specific work. Even if one were able to reduce drag by a factor of two, range would double, endurance would increase anywhere from 40% to 70% depending on the initial parameters of the aircraft. A simplified plot of Endurance factor vs. Cdo is shown below. The maximum available excess power would also vary with $\frac{Cl^{\frac{3}{2}}}{Cd}$ making the curve below representative of excess power as well.

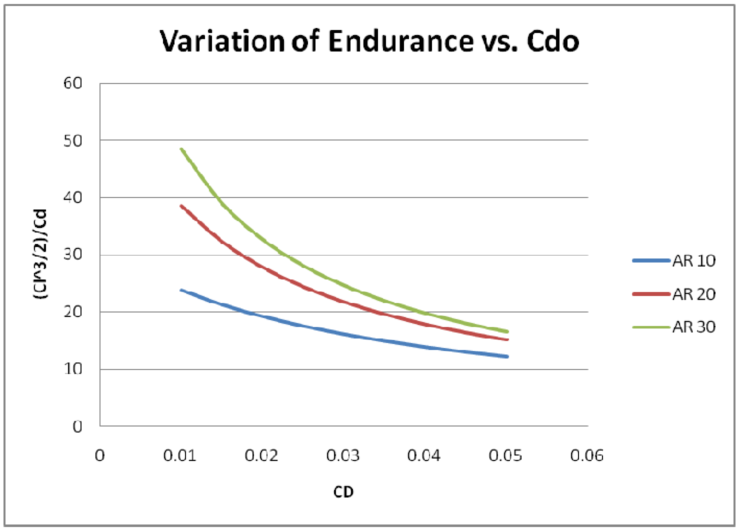

Figure 4 - Variation of Endurance with Cdo

Aerodynamic improvements may seem to offer considerable gains, but one must consider the added weight of any proposed system, the increased induced drag that weight would generate, and the true increase in system performance, not simply drag alone. It is for these reasons, barring a major revelation, that one should expect no more than 20% gain in ideal performance through creative aerodynamic methods.

Any structural weight savings in an aerodynamically optimized aircraft can immediately be replaced with an equivalent amount of extra fuel, making the aircraft fly proportionally longer and farther than before. Small aircraft's structures are most often determined by landing and ground handling loads, as the stresses seen in flight are often much less than those of an operator picking one up, or an aircraft performing a belly landing onto rock. Research aircraft such as the Oklahoma State Dragonfly exhibit weights nearly half those of production UAV's only because of the luxury of soft landings from slow descent rates. The maximum increase in single use range and endurance from weight savings alone would be nearly 200%, but such an airplane would never see practical use as it would be destroyed by landing loads, if not previously destroyed due to transportation loads. The maximum expected increase is therefore highly dependent on application.

Comparing the theoretical energy density of fuel cells, and combustion engines to that of the current aircraft battery standard immediately exposes the reason for focusing on energy density. Currently batteries in small aircraft contain 75 Watt Hours of energy per pound. Most small aircraft use battery packs weighing anywhere from three to five pounds, resulting in a total energy storage of 225 to 375 WH. Common pressurized fuel cell systems contain up to 480 WH/lb, and after accounting for buy in weight would provide between 330 and 1300 WH, an immediate increase in flight time between 1.5 and 3.5 time greater. Finally, a 25% efficient combustion engine would supply between 990 and 3200 WH, giving flights times of 4.4 to 8.5 times greater than that of lithium polymer batteries.

While propellers give a maximum increase of 20%, aerodynamic improvements give 20%-70%, and structure up to 200%, an increase in energy density can bring an 800% improvement to range and endurance to any battery powered aircraft regardless of its present design. It is important to remember that the aerodynamic, and structural improvement numbers are very dependent on application, and require application specific work. Propellers are a near universal option, but cannot provide a significant increase in performance. A maximization of stored energy will make an efficient airplane increase from 12 to 100 hours of flight, and even an inefficient UAV increase from one hour to 4.4 hours of flight. There is plenty of head room for energy density increase, and it provides the largest benefit to the largest number of systems.

NASA Technology Readiness Levels

NASA created the technology readiness level (TRL) grading system as a method for judging what stage of development an emerging technology is at. The system reduces ambiguity through a well defined set of states a technology can exist in ranging from observation of enabling principles, to actual flight implementation. These TRL's will be used in the following energy system discussion to indicate by NASA's definitions the perceived state of that technology as of June 2008. The various levels can be summarized as follows:

Technology Readiness Levels Summary

TRL 1 Basic principles observed and reported

TRL 2 Technology concept and/or application formulated

TRL 3 Analytical and experimental critical function and/or characteristic proof-of concept.

TRL 4 Component and/or breadboard validation in laboratory environment

TRL 5 Component and/or breadboard validation in relevant environment

TRL 6 System/subsystem model or prototype demonstration in a relevant environment (ground or space)

TRL 7 System prototype demonstration in a space environment

TRL 8 Actual system completed and “flight qualified” through test and demonstration (ground or space)

TRL 9 Actual system “flight proven” through successful mission operations

Common Terms for Evaluating Energy Systems

Energy systems discussed herein will be described through two governing parameters; Energy Density, and buy in weight. Energy density will be expressed in units of Watt hours per pound, and buy in weight in pounds. The energy density of the system is a result of the energy content of its fuel, the maximum charge its plates can carry, or the amount of time it is exposed to the source it is harvesting. Energy density for most systems is linearly proportional to fuel weight, but may vary with altitude, temperature, humidity, etc...

Buy in weight becomes a very important and difficult to predict value for evaluating the applicability of a given energy system on a specific platform. It represents the minimum unused weight for the system necessary to provide the required power. For an engine based system this would include the weight of the engine, fuel tubing, fuel tank, ignition system, etc. Any mass that cannot be turned into energy (within the abilities of that energy conversion system) must be listed as buy in weight. This parameter shows why micro aerial vehicles (MAV) primarily use batteries instead of cryogenic hydrogen fuel cells like Aerovironment's Global Observer.

Target Power Class

As the relative importance of buy in weight and energy density vary with overall mass allowance it is important to define a target power range for this energy study. A small unmanned aircraft will be defined as being between three and twenty pounds, having a wingspan of two to 15 feet, payloads of up to three pounds, a 200 watt cruise, and a 1000 watt maximum power requirement. Example vehicles in this range include the Lockheed Martin Stalker UAS, Aerovironment PUMA (pointer Upgraded Mission Ability), and the Oklahoma State Dragonfly and Pterosoar research aircraft.

Categories of Energy Storage

All energy systems studied in this paper can be categorized into three main groups. Direct energy storage systems, conversion based energy systems, and harvesting energy devices.

Direct energy storage methods like batteries and capacitors store electrical energy in ways that allow for the energy to be easily and directly harvested. This most often leads to the potential being stored chemically (in the case of batteries), or electromagnetically (in the case of the charged plates of a capacitor). This type of energy storage is the easiest to implement, is most often rechargeable by simply applying a driving voltage, but delivers average power density and very poor overall energy density. One of the main benefits of this storage type is the complete lack of buy in weight. Even a one ounce battery will begin to provide a small amount of useful energy.

Conversion based energy storage systems such as an internal combustion engine take fuel that is in an otherwise useless state, and through various processes convert that fuel into electrical energy. Many times these conversion systems create primarily rotational or translational kinetic energy that must then be converted to electrical through the use of a generator. Fuel cells and Metabolic conversion systems are also included in this group as examples of a conversion device who's direct output is electrical potential.

Conversion type devices are characterized by having considerable buy in weights that are accompanied by very high energy densities, and a wide range of power densities.

Harvesting type energy systems like solar cells are the newest type of energy system, and as a result are also the least developed. These type of energy systems have a time dependent energy density. For short missions where they may only be exposed to the sun for minutes, the energy density is near zero. However, for long duration missions (satellites, high altitude observation, etc...) their energy density approaches infinity. Their power density also varies based on the presence of whatever wavelength or type of energy they are harvesting. In general this is one of the most impractical, unreliable, and yet most theoretically enabling type of energy system.

Direct Energy Storage

Direct energy storage systems are currently the most common method of providing power to small unmanned systems on the ground or in the air. Industrially designed UAV's have benefitted from a hobbyist driven boom in battery technology and refinement. Hobbyists began with simplistic glow powered engines burning low ratio nitro methane, but many found the noise and the mess to troublesome and began making the best of available battery technology in the 80's. It is not until recently that battery technology has progressed enough to seriously challenge even the most inefficient hobby engine.

Nickel Cadmium

TRL 9

As the first Nickel Cadmium batteries became available to consumers, RC modelers were finally able to store enough energy to fly with brushed DC motors for short periods of time. The Nickel Cadmium battery chemistry was plagued by horrific energy density (25 WH/lb), bad charge memory problems, generation of flammable gases when overcharged, and the possibility of cell polarity reversal. They did however offer a low enough internal resistance that a few enterprising hobbyists enjoyed short flights.

The NiCd cells use a nickel hydroxide positive electrode, and a cadmium negative electrode in combination with potassium hydroxide to act as the electrolyte. The chemical reactions that take place in the cell during discharge are as follows:

$$Cd + 2OH^- \rightarrow Cd(OH)_2 + 2e^-$$

At the Cadmium Electrode

$$2NiO(OH) + 2H_2O + 2e^- \rightarrow 2Ni(OH)_2 + 2OH^-$$

At the Nickel Electrode

$$2NiO(OH) + Cd + 2H_2O \rightarrow 2Ni(OH)_2 + Cd(OH)_2$$

Net reaction

When electrodes in NiCd type batteries are overcharged, they dissipate the excess energy by creating either hydrogen or oxygen gas dependent on which electrode is overcharged. It is for this reason that the anode is regularly oversized to prevent the generation of hydrogen gas inside the battery. The excess oxygen gas is still quite flammable and must be released from the cell properly. Some cell construction types store the coiled electrodes in an effective pressure vessel to contain the gases until they can recombine into water. If the pressure limit is exceeded the cell vents, releasing the flammable gases, and looses a large portion of its capacity as the products necessary to generate electricity are now unbalanced.

When multiple NiCd cells are assembled into battery packs, some cells inevitably have lower capacities than the rest. When the overall battery pack approaches zero volts, these lower capacity cells can have a negative voltage across their terminals which generates hydrogen gas that damages the cell in ways similar to overcharging.

One of the many arguments against NiCd batteries is their apparent "memory effect" , where the battery essentially "remembers" the points it was repeatedly charged and discharged to. This argument is most likely a myth that has its origins in consumers continually overcharging batteries which reduces their overall capacity even though the battery will appear fully charged as it leaves the charger.

Dendritic shorting is a condition where crystals form in the battery that create conductive pathways between the electrodes. This causes the battery to short internally and radically decreases its useful lifespan. An extreme burst of current can break apart the crystals and restore the battery nearly to its original working condition, but the dendrites will rapidly reform, and the cell will "die" in a matter of days following the high current cleansing.

Nickel Metal Hydride

TRL 9

Nickel metal hydride batteries (NIMH) should be considered the second generation of practical rechargeable batteries for flight. They had slightly greater energy density than NiCad's (32 vs 25 WH/lb), lacked "memory" effects, but exhibit slightly higher internal resistance than NiCad.

The "metal" in NIMH batteries can actually be several different types of inter-metallic compounds with the most common being AB_5 with the A standing for a mixture of Lanthanum, Cerium, Neodymium, praseodymium, and B is Nickel, Cobalt, Manganese, or Aluminum. Some other compounds are available that deliver slightly higher energy densities, but are not commonly found in commercial batteries because that extra energy comes at the expense of longevity.

The chemical reactions that occur in NIMH batteries can be found below. When the battery is overcharged at low rates the oxygen that is produced at the positive electrode is able to recombine at the negative electrode resulting in the battery dissipating the overcharge energy harmlessly as heat. This makes NIMH batteries much more tolerant of overcharging, which is often interpreted as having less of a "memory" effect.

Negative Electrode

Positive Electrode

Lithium Ion/Polymer

<u>TRL 9</u>

Lithium Ion batteries provided an effective doubling (75 WH/lb) of energy density when they reached the consumer market. The battery type was initially proposed in the 1970's but needed considerable research to make the battery type less volatile. Original cells used lithium metal as the anode, and as a result were much too volatile for widespread use on the consumer market. Once a suitable graphite anode was found to replace the lithium metal, the batteries became much safer to use and saw entry into the consumer market. Research is continuing on this battery type to increase its cycle life, decrease the internal resistance, and further raise the end product energy density.

Lithium batteries have higher internal resistances than equivalently sized NiCad or NIMH batteries. However most battery packs in current generation small aircraft require many cells in parallel to provide sufficient flight times, and this resulting decrease in effective resistance makes the battery type more than suitable for high power applications.

The anode and cathode in lithium batteries can be made from many different compounds. Common Cathode materials include $LiCoO_2$, $LiMnO_4$, $LiFePO_4$, Li_2FePO_4F while common anode materials include graphite, silicon, germanium, and titanium oxide. The generalized reactions occur as follows:

Cathode Reaction

Anode Reaction

The reaction has limits with deep discharging leading to super saturation of the lithium cobalt oxide which in turn produces Lithium oxide

$$Li^{+} + LiCoO_2 \rightarrow Li_2O + CoO$$

Production of Lithium Oxide

Overcharging leads to the formation of Cobalt Oxide as shown in the following reaction.

$$LiCoO_2 \rightarrow Li^{+} + CoO_2$$

Production of Cobalt Oxide

These limitations on charging and discharging result in the common guidelines of not discharging batteries below 3.0 volts per cell, and never charging them over 5.2 volts per cell. Passing either condition will irreversibly damage the cell, and could lead to a dangerous meltdown.

Lithium Sulfur

TRL 9

Lithium sulfur batteries represent the current state of the art in consumer rechargeable battery technology. This chemistry should allow for energy densities approaching 180 WH/lb while also increasing the volumetric energy density over lithium ion type batteries. Current prototype cells from Sion are achieving 160 WH/lb energy densities at discharge rates up to 2C. The increase in energy is a simple result of the higher energy components used. The theoretical energy densities of base materials can be seen below. In 2007 the British company QinetiQ test flew their Zephyr Solar airplane to a new world unmanned duration record of 54 hours. The aircraft operated on high efficiency solar cells that charged lithium sulfur battery packs in the wings during the day, and used that energy to fly through the night.

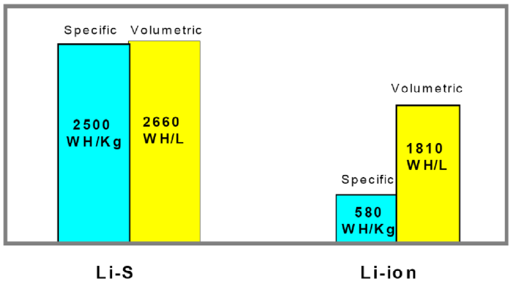

Figure 5 - Component Energy Densities (Turdon 2004)

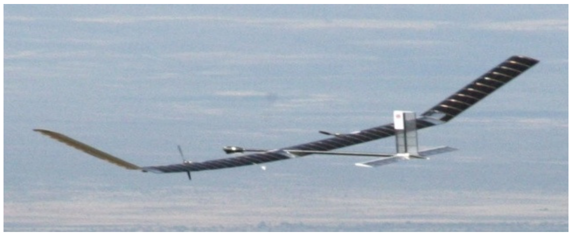

Figure 6 - QinetiQ's Zephyr Solar Lithium Sulfur Hybrid

Lithium Sulfur batteries utilize a two stage reaction during their discharge which increases their capacity, but requires the use of dedicated microcontrollers to control the load and output of the battery at different operating points. The variable system voltage also complicates propulsion system design for small aircraft, as the early voltage peak assists takeoff, but means the optimal cruise condition must be a compromise as the voltage varies 10% between the initial and secondary plateau.

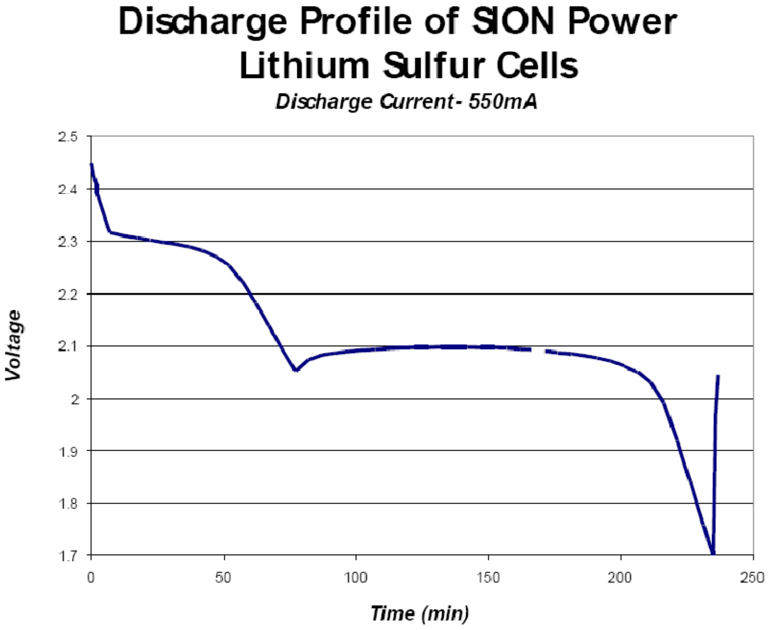

Figure 7 - Example of dual stage discharge curve (Sion 2005)

Capacitive Storage

TRL 5

Instead of storing electrical energy in chemical compounds, capacitors store energy in the form of electro-statically charged plates. This configuration most often results in a near negligible energy density, but new technologies are allowing capacitive storage to approach the levels of 1980's battery technology while providing power densities two orders of magnitude greater than modern battery technology. Current super capacitor energy densities range from 0.22 to 13 WH/lb with near term technologies promising 25 WH/lb. This type of energy storage is capable of millions of cycles before noticeable degradation whereas battery technologies are limited to between 200-1000 cycles before their performance significantly degrades. Capacitive storage is best suited to short duration high power situations such as power smoothing during transition between battery and engine power in a hybrid powered vehicle.

Figure 8 - Super capacitors made by Maxwell Technologies

Summary of Direct Energy

Direct energy storage methods are simple solid state solutions to providing dependable energy across a widely varying range of operating conditions. Their ability to act independently of most surrounding conditions, with the exception of their moderate sensitivity to temperature, makes them wonderful solutions to remote aircraft and ground vehicle power supplies, as those platforms participate in long duration missions that may cover a variety of atmospheric conditions. Portability, versatility, and a virtual lack of buy in weight is the main reason for batteries powering all mainstream laptops, cell phones, and other small devices. When the weight budget for power is quite small, no other solution is able to provide similar power levels. A plot of total energy vs. weight is shown below to display the relative difference between direct energy technologies. Note that all technologies pass through the origin, which is indicative of their lack of buy in weight. When comparing electrical energy to shaft energy, one should apply an 20% efficiency loss to represent the motor, and 5% efficiency loss to represent the speed controller. This reduces all direct energy systems' densities and output power by approximately 24%. Using the data gathered from the OSU Dragonfly program that in

2005 broke the FAI 5Kg world flight duration record. The increase in energy density of LiS over Li-polymer would double the possible flight time, assuming equal payload fraction and parasite drag, meaning that electric only flights of 20+ hours from man portable UAV's are now possible for low power levels, and with more work from Sion, the technology will surely progress to enable higher discharge rates, marginally higher energy densities, and better temperature tolerance.

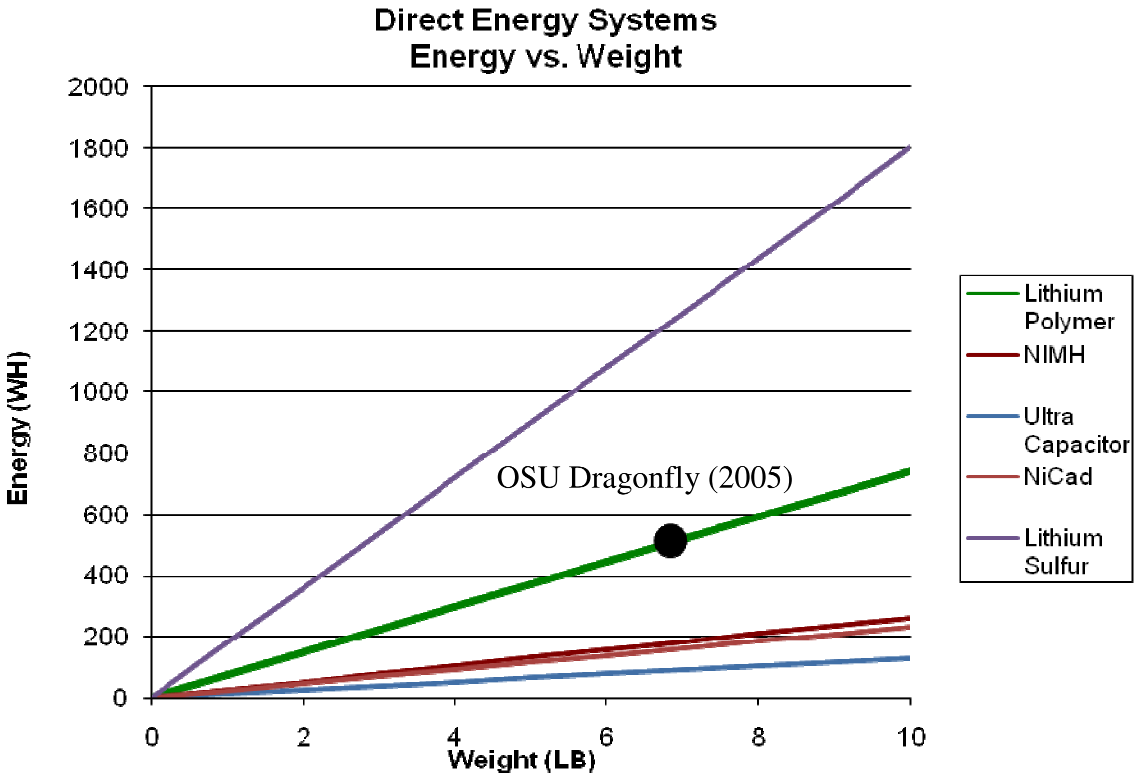

Figure 9 - Direct Energy Methods, Energy Density vs. System weight

Harvesting Energy Sources

Harvesting type energy systems consist of any type of device that absorbs energy from its surroundings to repurpose it for the designers means. The research momentum behind this category of energy has grown significantly in the past ten years because of Harvesting's inherent "green" connotation. Harvesting energy sources include everything from solar panels, piezoelectric devices, to hydroelectric dams, and provide power ranging from milli. through Megawatts. Harvesting type energy sources cannot be evaluated on the same total energy vs. system weight chart as direct energy and conversion types. They can have infinite energy density as long as power requirements stay below what is provided by the surrounding environment.

Solar Cells

TRL 9

Easily the most popular and widespread harvesting energy source, solar cells were also the first device in this category to achieve human powered flight. Dr. Paul MacCready designed the "Solar Challenger" in 1981 and his team flew it nonstop between Paris France and Manston RAF base in the United Kingdom. The flight lasted 5 hours and 23 minutes, and was limited only by mechanical degradation of the electric motor, and pilot endurance. The Solar challenger is an excellent example of the Achilles heel of Solar Cells. The regimes of flight where an aircraft regularly needs the most power, takeoff and climb, are the points in the flight where the least power is available. In the case of the solar challenger the low level dust in the atmosphere combined with the natural reflective properties of air, severely reduced the power output of their solar array until they could climb above the interference.

Solar cells also require what is known as a maximum power tracker to make best use of their available power. As shown in the figure to the right, a typical solar cell does not have a linear relationship between voltage and output power. For this reason a digital duty cycle controller is normally used to continually modify the duty cycle of the cells to deliver the maximum output power. To further complicate things, if cells are mounted on the vehicle at varying angles, each region will be producing a different output voltage. If these cells were simply wired together and passed through a single maximum power tracker, the best result that could be hoped for is a compromise between those cells receiving direct sunlight, and those that are at large angles to the oncoming light. Each similarly oriented group of cells must have its own maximum power tracker, and then the various voltage levels from each individual bank is combined through a secondary rectifier so that the total summed power may be delivered to the propeller.

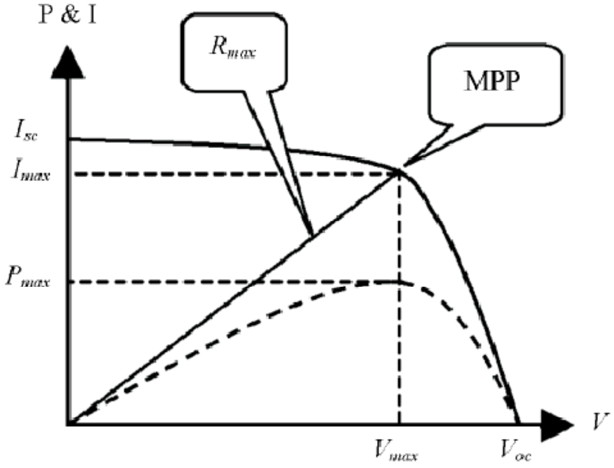

Figure 10 - Solar cell power profile - Jiang Et. Al.

The total solar energy that hits earth per square meter of the upper atmosphere is approximately 1.3 KW per square meter. After accounting for atmospheric attenuation 1KW is left to be harvested near the earths surface assuming no cloud cover or smog in the air. For fixed platform cells like solar farms, the cells are often tilted to account for their latitude, but most often do not track the sun as it passes overhead. This reduces the total useable insolation in the United States to anywhere between 80 watts per square meter, to 330 watts per square meter, depending on the location and time of year. The annual average, June, and December average insolation charts as measured by the NREL are shown below. The total power available to a flying solar powered aircraft is even below the levels shown in the following NREL data as the cells on an aircraft are most often laid over its wings, which except for special designs, do not account for changes in latitude.

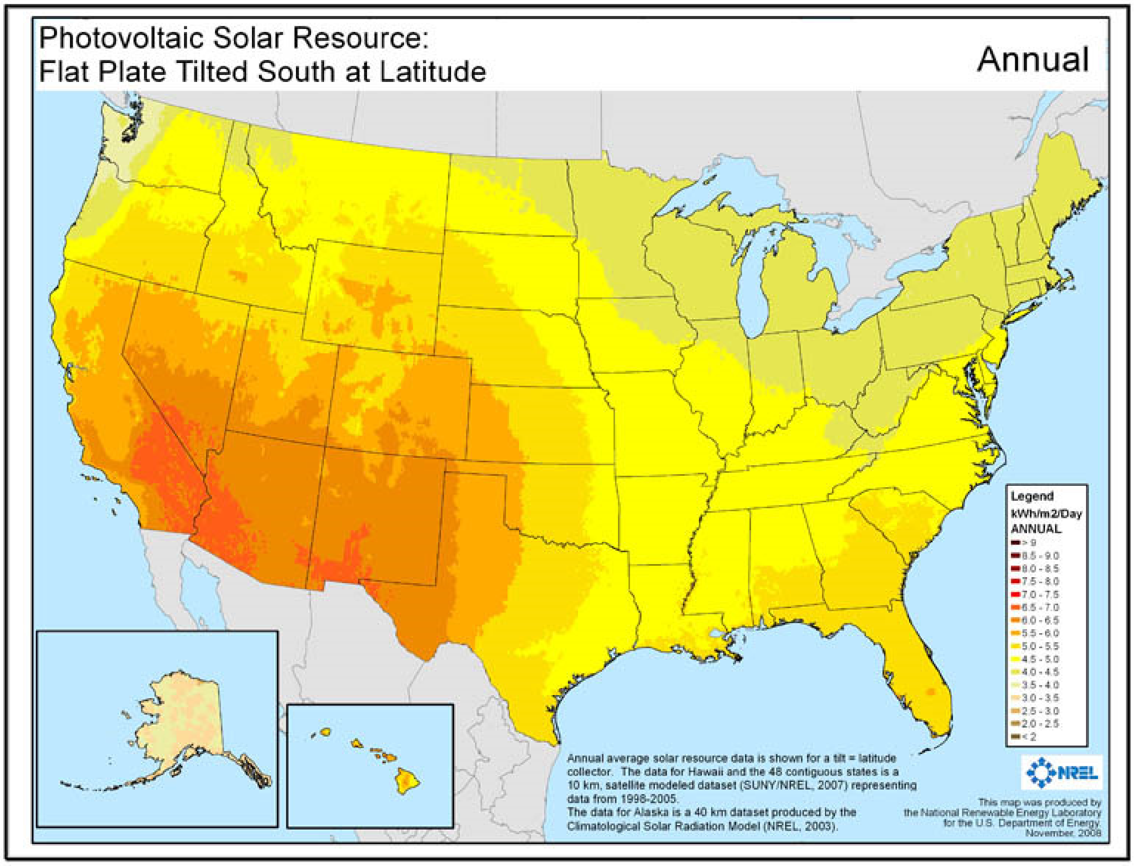

Annual average solar resource data is shown for a tilt = latitude collector. The data for Hawaii and the 48 contiguous states is a 10 km, satellite modeled dataset (SUNY/NREL, 2007) representing data from 1998-2005.
The data for Alaska is a 40 km dataset produced by the Climatological Solar Radiation Model (NREL, 2003).

This map was produced by the National Renewable Energy Laboratory for the U.S. Department of Energy. November, 2008

Figure 11 - Annual Insolation for non tracking latitude compensated plates (NREL)

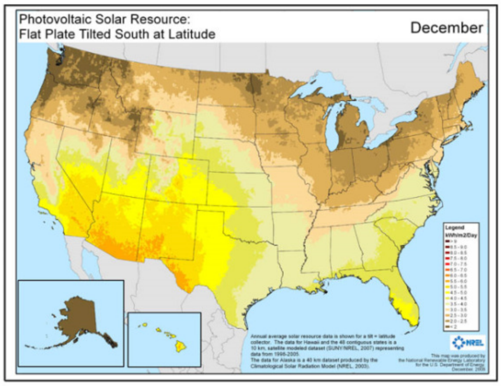

Figure 12 - December Average Insolation

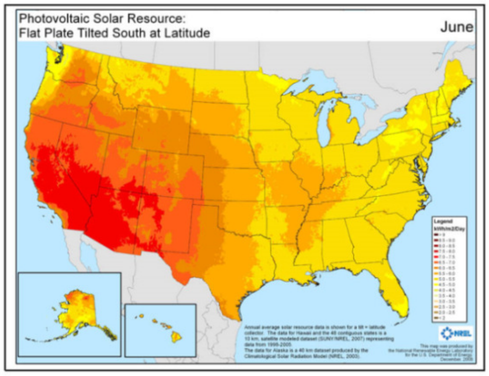

Figure 13 - June Average Insolation

The available power output of solar cell is determined by the combination of available irradiation, and the overall efficiency of the cell involved.

$$Power = Total\ Insolation \times \eta cell$$

The maximum efficiency of solar cells has steady increased since their beginning, with research grade cells now exceeding 40% efficiency. The mechanism by which the cells efficiency has been increased lie outside the scope of this paper.

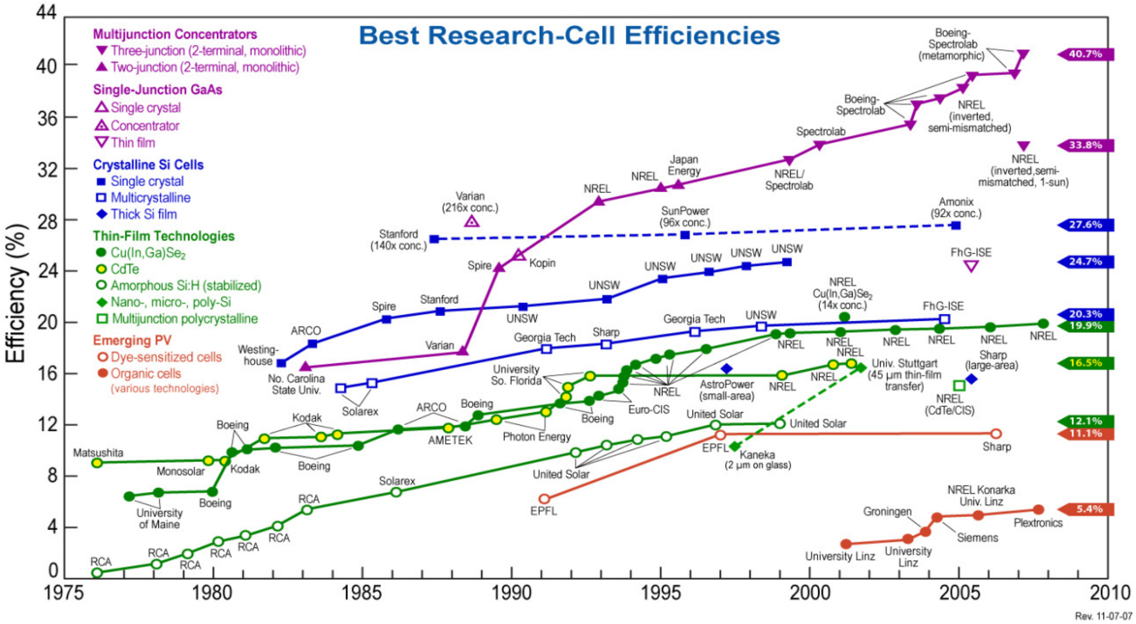

Figure 14 - Research Solar Cell Efficiency (DOE)

Thermoelectric Conversion

<u>TRL 4</u>

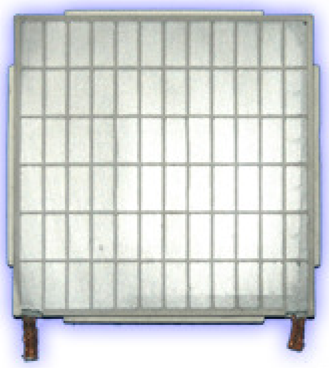

Thermoelectric energy harvesting is the direct conversion of heat into electricity. The power generation is a result of the seebeck effect, where dissimilar metals produce a potential difference when exposed to a thermal gradient. It is the same effect thermocouples use to measure temperature. The governing design decision for thermoelectric's is what type of materials to use to create the power source. The figure of merit used to rate different materials in their ability to be effective thermoelectric devices is simply labeled ZT.

—

Where

$\sigma = electrical\ conductivity, S = Seebeck\ Coeffecient, \lambda = thermal\ conductivity$, and T is the average junction temperature of the given material. In general, a highly conductive, and yet thermally insulating material will be the best thermoelectric device. The relation between Z and overall efficiency is given by the equation below. (Yoshida Et. Al.)

ΔT = *Temperature Differential*

T_h = *Hot Junction Temperature*

T_b = *Average Hot and Cold Junction Temperature*

T_c = *Cold Junction Temperature*

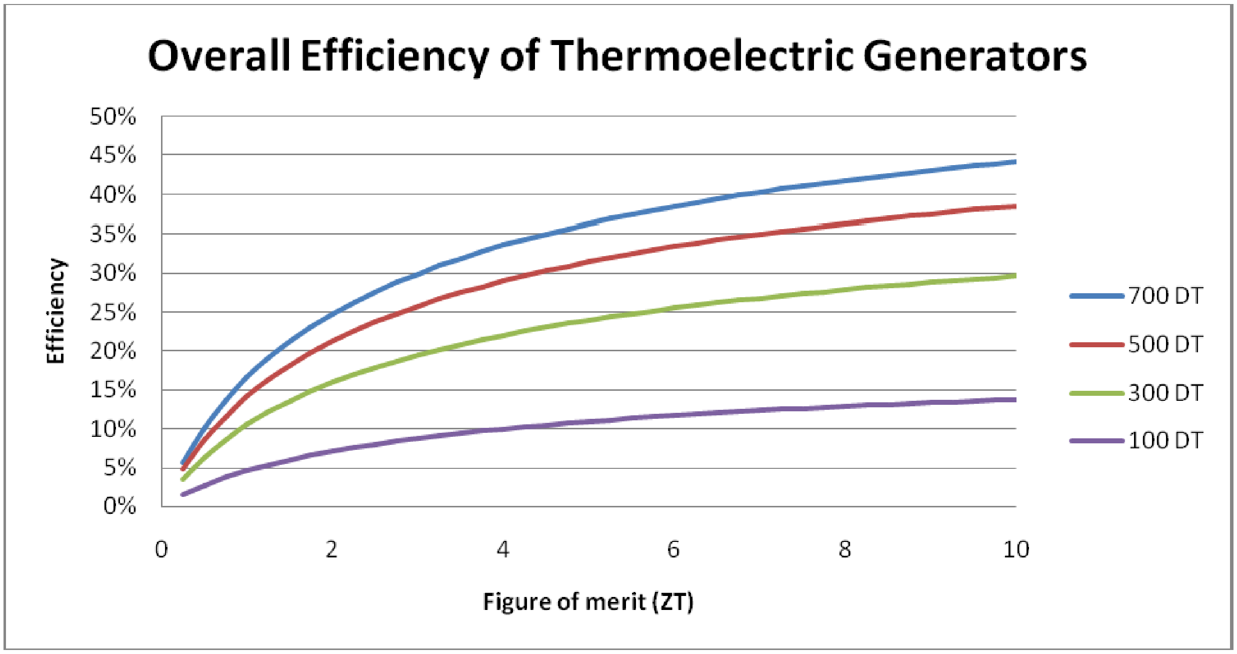

Figure 15 - Efficiency of Thermoelectic Generators

Thermoelectrics can be thought of as peltier devices running in reverse. Instead of applying power to create a temperature difference between plates. A temperature difference between plates provides power. It is the same Seebeck effect that drives both a peltier cooler and a thermoelectric generator.

Current thermoelectric devices are very inefficient, with all production models exhibiting less than 5% efficiency. Research efforts to implement thermoelectric devices suffer even greater efficiency losses. Yoshida Et. Al. measured a maximum of 2.5%

efficiency in their test device. The decreased efficiency is due to heat loss to other sources. Manufacturers of thermoelectric devices measure only the heat travelling through the device to determine its efficiency. In real applications, there will always be some level of heat loss outside of that which passes through the thermoelectric device.

The company Hi-Z implemented a heat regeneration system on heavy diesel trucks that was able to recycle 1KW of energy from waste heat around the trucks exhaust. The system is much too heavy to be used in SUAV's at its specific power levels (2.72 watts per lb), but works just fine for satellites that carry onboard radioisotope heating devices to generate electrical power in space for years. radioisotope thermal generators (RTG's) have been used in numerous space missions (Apollo 12-17, Cassini, and Voyager) as well as terrestrial uses like remote lighthouses. Current devices range in output from 2.7 to 300 watts.

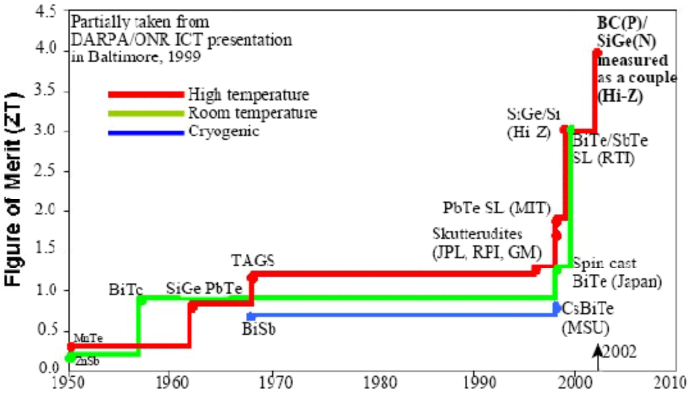

Figure 16 - Figure of Merit Timeline (Jovanovic Et. Al.)

Many startup and well established thermoelectric producers are researching quantum well thermoelectric devices. Jovanovic Et. Al. have published data showing the next generation of thermoelectric devices to be 15% efficient, and have included test data proving their claim. The continue in the paper to say "Based on the current experimental work, thermal to electric conversion efficiencies of 20-40%... are anticipated" (Jovanovic Et. Al.) If thermoelectric generators with those efficiencies are able to be produced at reasonable cost, they will revolutionize the way the world creates power. At that conversion efficiency, a thermoelectric solar concentrator would be roughly equivalent to the performance of a top tier solar cell. The true place for a high efficiency TEG in the SUAV world would be as a chemical energy conversion device, which will be covered in the conversion section of this paper.

Soaring

TRL 9

Soaring is by far the most green, and currently the most common source of flying aircraft off harvesting type power sources. It is impossible to give an energy density for soaring because of its naturally varying nature. A pilot (or autopilots) ability to extract energy from the surrounding atmosphere will govern the maximum power output from that flow, while the energy density of soaring flight is effectively infinite because no extra equipment is required to enable the aircraft to soar. Some aircraft are better than others at using the relatively low levels of energy in the atmosphere to stay aloft, but any design can benefit from un updraft without any additional weight, thus making the energy density of this flight type infinite. The most basic type of soaring uses an upward moving air mass, an aircraft extracts energy from the flow as it moves upward over a mountain, due to thermal gradients, or other obstruction. The only criteria for sustained soaring in such an updraft is that the aircrafts sink rate is lower than the vertical velocity of the airmass it is flying in. The aircraft may seek its optimal angle of attack through the rising air mass by flying through it in an S pattern of varying horizontal amplitude to fly at its minimum sink rate.

The second most common method of extracting energy from the flow in an aircraft is dynamic soaring. This method requires a sizeable velocity gradient to be present. This could be the result of vortex formation on the leeward side of mountains, flow around the corners of buildings, or any other environment with two differently moving bodies of fluid. The method is easiest to understand in its extreme circumstance where the flow velocity gradient across a shear plane varies so greatly that the direction of flow is reversed. In that circumstance, an aircraft flying in a circular pattern centered on the shear layer would be given a kinetic energy boost each time it passed between regions as its inertial reference frame is accelerated to match the local wind’s reference frame. As long as this boost provides more energy than the aircraft spends during its time in that moving air mass, it will accelerate each time it makes the transition. This acceleration is not limited to the velocity of either air mass. The aircraft’s acceleration is only dependent on the intensity of the shear layer it is passing through, and the energy it dissipates as it loops around. The current unofficial world record for dynamic soaring stands at 357 miles per hour. There is an immense amount of energy to be had through soaring of all types, whether it be thermal, slope, or dynamic soaring. But the aircraft utilizing such methods will always be bound to only short excursions away from its power source, if atmospheric conditions are acceptable at all.

Conversion Type Energy Sources

Conversion type energy sources store energy in some sort of fuel that is then converted using various reactions and devices into useable energy. Combustion engines, fuel cells, and thermoelectric converters are all forms of conversion energy devices. Conversion systems are characterized by large buy in weights associated with whatever device is necessary to change its fuel into useable energy. Many methods create kinetic energy that must be converted to electrical if it is to be stored with any appreciable density. This extra step adds to overall buy in weight which in turn significantly reduces the systems energy density. The drawbacks of large buy in weight are more than offset by the extreme energy density offered by conversion type systems. Recall that the mainstream battery chemistry, lithium polymer, typically achieves an energy density of 75 WH/lb. The stored energy in one pound of gasoline is approximately 5680 WH. This is a difference of over 80 times. If hydrogen is used as a fuel, the available energy increases to 18,000 WH/lb, a difference of over 250 times that of lithium polymer batteries. The large difference between the energy density of common fuels, and batteries is often used inappropriately to scale aircraft performance by the corresponding ratio of energy densities. And the difference in the energy of hydrogen fuels, and carbon fuels is also abused to encourage the development and use of fuel cells. The weight associated with storing these fuels is often overlooked. It is also important to remember that the type of fuel that is being burned means nothing unless it's energy can be harvested efficiently. Most conversion type devices are theoretically limited by Carnot efficiency, but seldom approach that idealized result because of cycle imperfections. This section will cover in detail the overall energy density of each conversion power system including everything up to the point of electrical energy output and/or rotational kinetic energy.

Hydrogen Fuel Cells

TRL 9

Hydrogen fuel cells have become a very popular target power source for small UAV's recently as a result of hydrogen fuels incredible energy density, and the fuel cells overall efficiency. The most common type of fuel cell designed to power UAV's is the proton exchange membrane fuel cell (PEM). This type of cell was used in Oklahoma State's Pterosaur aircraft to power it to an unmanned aircraft distance world record. The PEM fuel cell's buy in weight will scale with required power, and its fuel tank weight interestingly scales linearly with volume when accounting for an optimized tank wall thickness, making the reduction in overall energy density caused by tank weight even easier to calculate. The linear relation between stored energy and tank weight is shown below. The development should be considered an absolute theoretical limit on the energy density of a pressurized fuel system.

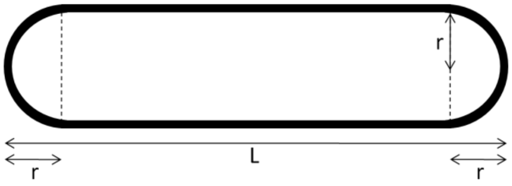

Figure 17 - Schematic of Tank

Figure 18 - Schematic Representation of tank Geometry

$$\frac{P \cdot r}{\sigma_{max}} = T$$

Hoop Stress Equation for Cylindrical Pressure Vessels

$$[4\pi r^2 + 2\pi r(L - 2r)] = S$$

Surface area of defined tank geometry

$$S \cdot T \cdot \rho_{wall} + V \cdot \rho_{fuel} = W$$

Weight of tank and enclosed fuel

$$\frac{4\pi r^3}{3} + (L - 2r)\pi r^2 = V$$

Enclosed volume of defined tank geometry

$$V \cdot \rho_{fuel} \cdot E_{\rho\ fuel} = E_{stored}$$

Total Stored Energy

$$\frac{L}{2r} = AR_{tank}$$

Definition of tank aspect ratio

$$\frac{E_{stored}}{W} = \frac{\left[\left(\frac{1}{3\pi r^3} + (L - 2r)\pi r^2\right) \cdot \rho_{fuel} \cdot E_{\rho\ fuel}\right]}{\left[[4\pi r^2 + 2\pi r(L - 2r)]\frac{P \cdot r}{\sigma_{max}} \cdot \rho_{wall} + \left(\frac{1}{3\pi r^3} + (L - 2r)\pi r^2\right) \cdot \rho_{fuel}\right]}$$

Expanded tank and fuel energy density

$$\rho_{fuel} \cdot E_{\rho\ fuel} = E_{\rho\ volumetric}$$

Fuel property Identity

$$\frac{E_{stored}}{W} = \frac{\left[V \cdot E_{\rho\ volumetric}\right]}{\left[S\frac{P \cdot r}{\sigma_{max}} \cdot \rho_{wall} + V \cdot \rho_{fuel}\right]}$$

Collapsed tank and fuel energy density

$$\frac{S}{V} = \frac{[4\pi r^2 + \pi r(L - 2r)]}{\frac{4\pi r^3}{3} + (L - 2r)\pi r^2}$$

Surface to volume ratio development for defined tank geometry

$$\frac{S}{V} = \frac{\left[4\pi r^2 + \pi \frac{L}{AR}\left(L - \frac{L}{AR}\right)\right]}{\frac{4\pi r^3}{3} + \left(L - \frac{L}{AR}\right)\pi r^2}$$

$$\frac{S}{V} = \frac{\left[4\pi r^2 + \frac{\pi L^2}{AR} - \frac{\pi L^2}{AR^2}\right]}{\frac{4\pi r^3}{3} + L\pi r^2 - \frac{L\pi r^2}{AR}}$$

$$\frac{S}{V} = \frac{\frac{4\pi r^2 AR^2 + \pi L^2 AR - \pi L^2}{AR^2}}{\frac{\frac{4}{3}\pi r^3 AR^2 + L\pi r^2 AR^2 - L\pi r^2 AR}{AR^2}}$$

$$\frac{S}{V} = \frac{4\pi r^2 AR^2 + \pi L^2 AR - \pi L^2}{\frac{4}{3}\pi r^3 AR^2 + L\pi r^2 AR^2 - L\pi r^2 AR}$$

$$L = 2rAR$$

$$\frac{S}{V} = \frac{4\pi r^2 AR^2 + 4\pi r^2 AR^3 - 4\pi r^2 AR^2}{\frac{4}{3}\pi r^3 AR^2 + 2\pi r^3 AR^3 - 2\pi r^3 AR^2}$$

$$\frac{S}{V} = \frac{R^2(4\pi AR^3)}{r^3\left(\left(\frac{4}{3}\pi - 2\pi\right)AR^2 + 2\pi AR^3\right)}$$

$$\frac{S}{V} = \frac{K_{AR}}{r}$$

Simplified surface to volume ratio for defined tank geometry, note that for a constant aspect ratio the relation is simply $\frac{1}{r}$.

$$K_{AR} = \frac{4\pi AR^3}{\left(\frac{4}{3}\pi - 2\pi\right)AR^2 + 2\pi AR^3}$$

Definition of aspect ratio constant for use in the surface to volume equation

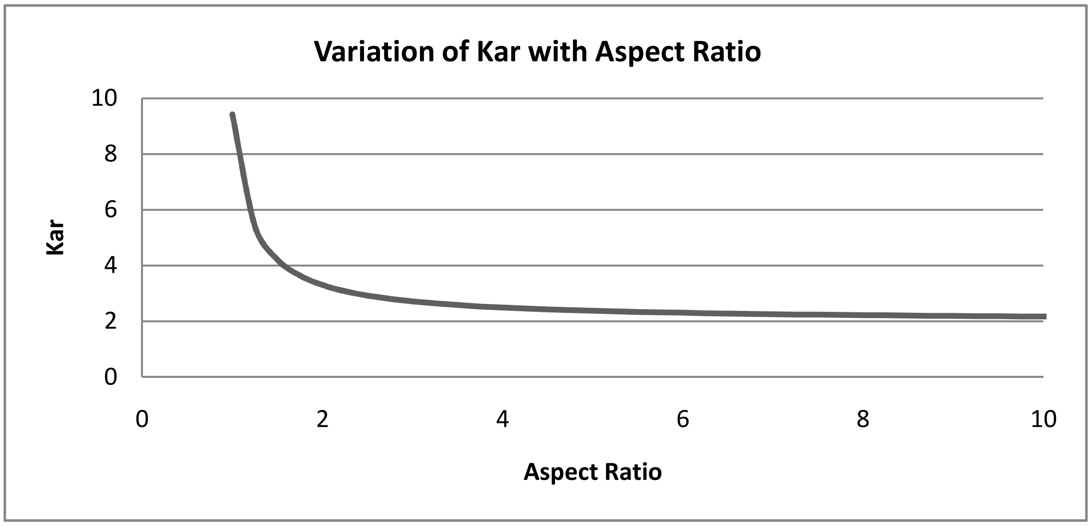

Figure 19 - Variation of Kar with Aspect Ratio

The chart above shows the large increase in surface to volume ratio for low aspect ratio tanks. An aspect ratio of 1 signifies a cylindrical pressure vessel, and K_{AR}converges to 2.0 for large values of AR.

$$V = \frac{S \cdot r}{K_{AR}}$$

$$\frac{E_{stored}}{W} = \frac{\left[\frac{S \cdot r}{K_{AR}} \cdot E_{\rho\ volumetric}\right]}{\left[S \frac{P \cdot R}{\sigma_{max}} \cdot \rho_{wall} + \frac{S \cdot r}{K_{AR}} \cdot \rho_{fuel}\right]}$$

Tank energy density equation with surface to volume ratio equations substituted.

$$\frac{E_{stored}}{W} = \frac{S \cdot r \left[\frac{1}{K_{AR}} \cdot E_{\rho\ volumetric}\right]}{S \cdot r \left[\frac{P \cdot \rho_{wall}}{\sigma_{max}} + \frac{\rho_{fuel}}{K_{AR}}\right]}$$

$$\frac{E_{stored}}{W} = \frac{\frac{E_{\rho\ volumetric}}{K_{AR}}}{\frac{P \cdot \rho_{wall}}{\sigma_{max}} + \frac{\rho_{fuel}}{K_{AR}}}$$

Simplified energy density equation shows total energy density to be a linear function of tank and fuel weight.

$$\frac{E_{stored}}{W} = \frac{E_{\rho\ volumetric} \cdot \frac{1}{K_{AR}}}{\rho_{fuel} \left[\frac{P \cdot \rho_{wall}}{\sigma_{max} \cdot \rho_{fuel}} + \frac{1}{K_{AR}}\right]}$$

$$E_{\rho\ m} = \frac{E_{\rho\ volumetric}}{\rho_{fuel}}$$

$$\frac{E_{stored}}{W} = \frac{\frac{E_{\rho\ m}}{K_{AR}}}{\frac{P \cdot \rho_{wall} \cdot K_{AR} + \sigma_{max} \cdot \rho_{fuel}}{\sigma_{max} \cdot \rho_{fuel} \cdot K_{AR}}}$$

$$\frac{E_{stored}}{W} = \frac{E_{\rho\ m} \cdot \sigma_{max} \cdot \rho_{fuel}}{P \cdot \rho_{wall} \cdot K_{AR} + \sigma_{max} \cdot \rho_{fuel}}$$

Final simplified form of energy density equation. While this equation shows pressure to decrease the total energy density of a tank system, one must remember that the density of the fuel increases with pressure. The final equation shows the importance of the energy density of the fuel, the strength to weight ratio of the tank material used, and the overall density of the fuel. The ultimate strength of carbon/graphite composites was assumed to be 650KSI, and any necessary linings for the tank were ignored. The total energy stored as a function of weight is shown in the graph below after solving the previous equations and applying a 2.3 lb buy in weight. The hydrogen was assumed to be in a gaseous state, stored at 5000 psi giving it a density of 1.2 lb/ft^3. A safety factor of 3.6 was used to correspond with European standards.

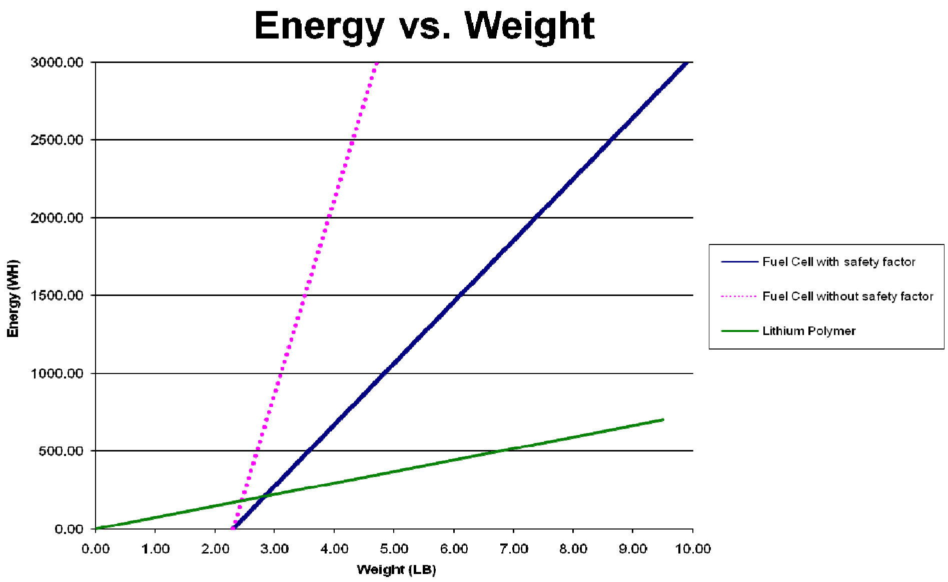

Figure 20 - Stored Energy vs. system weight (without minimum thickness)

Allowing the wall thickness to be automatically optimized for varying tank size resulted in infeasible tanks with walls thinner than a single layer of carbon. The numerical solver was forced to use at least a 0.1 inch thick wall so the tank could be self supporting when empty, and sufficiently thick to prevent leaks. Because the tank wall thickness was constrained, the energy density curve regained the 1/r characteristic of the tank geometry. Once the required wall thickness exceeds 0.1 inches, the curve returns to being linear.

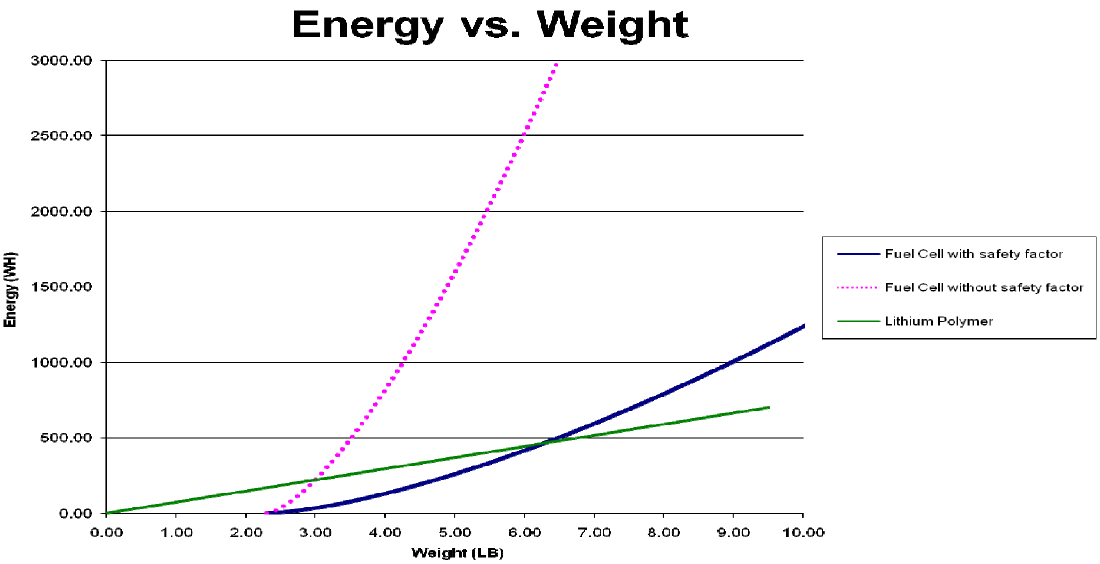

Figure 21 - Stored Energy vs. system weight (with 0.1 inch minimum thickness)

The PEM fuel cell that was a part of the Pterosaur project operated at an impressive 41% efficiency, which combined with pure hydrogen would produce an overall energy density of 7402 WH/lb if it were not for the excessively heavy storage of hydrogen gas. Pressurized solutions only achieve a hydrogen to tank mass percentage of 5.7%. This reduction in stored hydrogen reduces the overall energy density to only 395 WH/lb. The storage of hydrogen is a very well known and common research topic. The following are research areas trying to address how to store hydrogen with a higher weight percentage.

Cryogenic Storage

TRL 9

Cryogenic hydrogen storage is without question the most energy dense system available today. It combines the high energy density of Hydrogen, converts it to electricity efficiently by using a fuel cell, and avoids much of the tank weight by compressing the hydrogen with temperature instead of pressure. The resulting system delivers an astonishing 85% mass fraction of hydrogen for very large tanks, which results in an energy density over 15,300 WH/lb. Based on conversion efficiency, storage weight, and energy density alone, that is over 200 times the energy of lithium polymer batteries that currently power small scale vehicles.

Cryogenic hydrogen storage has some serious drawbacks that prevent it from being an ideal power source. The tanks are sensitive, if excessive heat leaks in by any means, the boiled off gasses must be exhausted which creates a fire hazard. Alternatively the boiled off gas can be held inside the tank, but the building pressure creates an explosion risk unless the tank is made as heavy as the previously mentioned pressure vessels. Also, cryogenic systems have an incredibly large buy in weight as they most often require active cooling to keep the hydrogen liquefied. The smallest stirling cryocooler would use up most of the weight budget for an SUAV power system leaving little for the fuel cell, tank, hydrogen, and other necessary equipment. The large buy in weight associated with cryogenic hydrogen storage means that the method will only be accessible to larger aircraft for some time.

Glass Microspheres

TRL 4

Glass microspheres utilize the natural ability of hydrogen to travel through the glass wall as a way of filling and evacuating the microspheres. The microspheres work in exactly the same way as macro scale pressure vessels, but have wall thicknesses on the order of 0.68 micrometers, and can withstand pressures up to 9000psi inside. The rate it which hydrogen passes through the walls of the microsphere is very temperature dependent. At room temperature the fill rate is on the order of 5000 hours, while at 300 degrees C. the fill rate drops to only 15 minutes. Mass fractions of up to 10% are achievable with high strength spheres which results in an energy density of 1800 WH/lb before accounting for the storage area of the spheres, their heating apparatus, any heat exchanger between the spheres and the fuel cell, etc. All of those additional pieces of hardware will increase the buy in weight of the system making the glass microsphere solution less practical. [Colozza – NASA]

Chemically bound (reformation type)

TRL 9

Chemically bound hydrogen reformers use common fuels like propane, methane, and gasoline to store hydrogen in reasonably high mass fraction molecules. The fuel is passed through a reactor before being used in the fuel cell where a catalyst converts the chemical compounds into hydrogen to use in the fuel cell. One must take care when selecting this type of energy system while seeking maximum energy density. In some cases it is possible that the energy required by the reforming reactor, combined with its additional weight would make it more beneficial to burn the fuel directly instead of passing it through a fuel cell. Common fuel types, their Hydrogen weight fraction and volumetric energy density are shown in the table below.

Fuel (in liquid state)	*Hydrogen Weight Fraction*
Hydrogen	100%
Methane	25%
Ethane	20%
Propane	18%
Gasoline	16%

Ethanol	13%
Methanol	12%

The reformation of logistics fuels like JP-8 has proven problematic as the high carbon and sulfur content of these fuels saturates and poisons the catalyst that normally drives the reaction. The current longest flight by a fuel cell man-portable UAV is the aerovironment Puma, which stayed in the air for over nine hours utilizing a Protonex Sodium Borohydride reforming fuel cell in combination with a battery hybrid setup for high power segments of flight.

Carbon Nanotubes/Graphene Sheets.

TRL 2

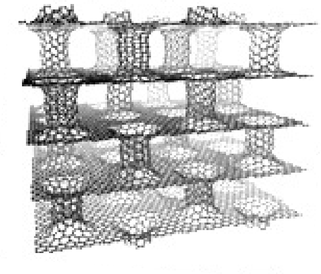

Carbon nanotubes are proposed to store hydrogen through a method similar to metal hydrides albeit at much greater mass fractions. Early research suggests that nanotubes can store anywhere from 4% to 65% of their mass in hydrogen. Another similar research line suggests storing hydrogen between thin layers of graphene. Simulations of graphene sheets in combination with buckyballs show storage percentages exceeding 6% by mass (Froudakis).

Metal Hydride

TRL 9

Metal hydride stores hydrogen by temporarily bonding it with metals, and then using waste heat from the fuel cell to release that hydrogen for use. This is currently the safest form of hydrogen storage, capable of being punctured, dropped, and otherwise abused without exploding. The metal hydride is very susceptible to contamination, where other elements work their way into the storage cell, taking up bonding locations where the hydrogen would normally reside. This reduces the overall capacity of the metal hydride bank. Metal hydrides are capable of large volumetric energy densities (168 KWH/ft^3), but only achieves mass percentages of 0.5 to 1% currently. That mass percentage corresponds to an energy density of 90 WH/lb which is less than current lithium sulfur battery technology even before accounting for the fuel cell buy in weight. Future research suggests this percentage may rise as high as 5%, which would make it an excellent solution for safe, reasonably dense energy storage.

Conclusions on Fuel Cells

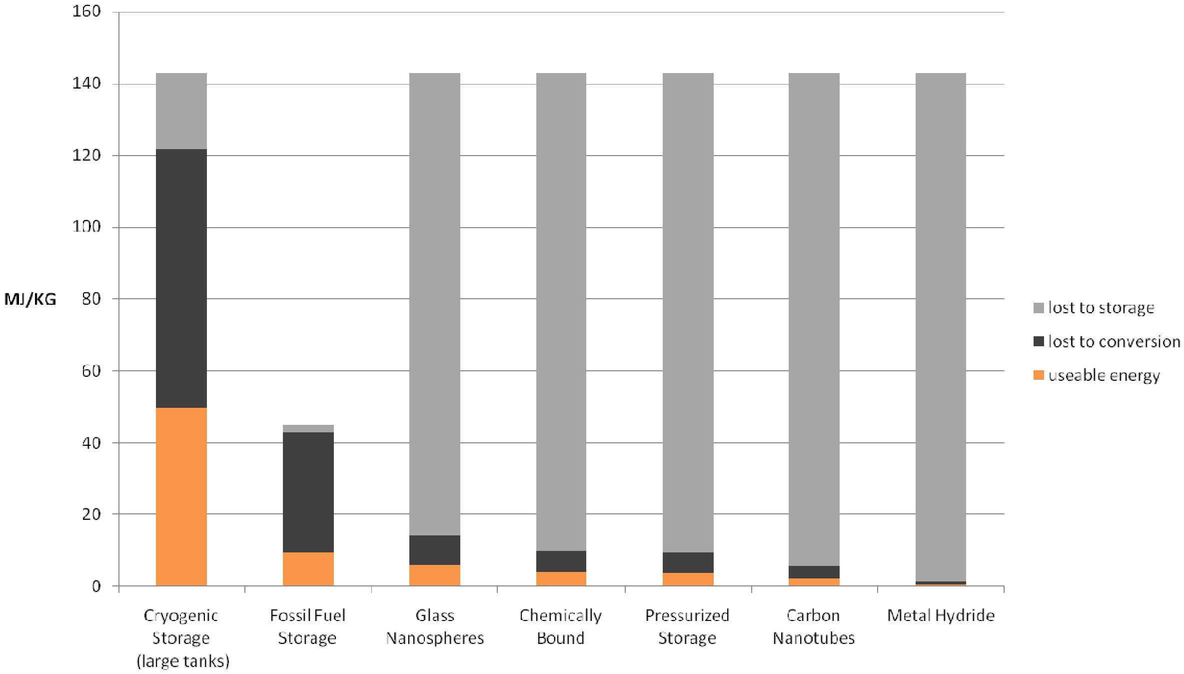

Figure 22 - Losses associated with Hydrogen fuels

When the various methods of storing hydrogen are plotted against one another with similar fuel cell conversion efficiencies, the drawback to all hydrogen based systems becomes apparent. The loss associated with storing hydrogen gas eliminates most of its energy potential. Cryogenic storage is currently the only system that can surpass the energy density of a common fossil fuel based engine, but the hardware involved with cryogenics is too massive for use on SUAV's. Once Cryogenic storage is eliminated from consideration, engines are the most energy dense systems that are compatible with small aircraft. Although the energy density of gasoline is approximately one third that of hydrogen, its ease of storage makes up for the energy it naturally lacks.

Generalized Thermodynamic Conversion Systems

All of the following systems operate off the expansion and contraction of gasses. Whether it is internal or external combustion, no matter the fuel type, or mechanical sophistication, no following engine can surpass Carnot efficiency. To determine the upper limit on efficiency the equation $\eta = 1 - \frac{T_c}{T_h}$ is used. T_c and T_h indicate the respective hot and cold reservoir temperatures that the cycle operates in-between. For external combustion it would be the temperature difference between the inner surfaces of the heat exchangers, for internal combustion the variation of the internal gas temperature would be used in determining the maximum possible efficiency. As shown previously, efficiency is very important because it is the term that scales the energy density of the fuel as it is converted to useable energy. The Carnot cycle is only a theoretical cycle, and all practical engines vary significantly from its prescribed pressure to volume relationships. One must be careful when comparing shaft output power to electrical power as is generated in direct energy systems. If the purpose is to generate electrical power, all energy densities and output power numbers should be reduced by approximately 28% to represent generation and rectification losses.

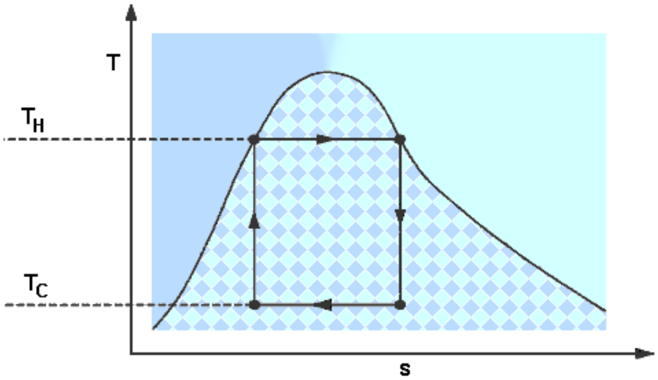

Figure 23 –Carnot Ideal Cycle (USDOE)

Two Stroke Combustion Engine

<u>TRL 9</u>

Two stroke engines are defined by firing once per revolution of the crankshaft. They utilize passive valves that are opened and closed by the very motion of the piston traveling up and down. Because of this, the engines are not as well scavenged (evacuation of previously combusted material) as their four stroke counterparts. The motion of the piston is also used to draw air into the intake, and then drive it into the cylinder. Because two stroke engines effectively have their intake and exhaust valves open simultaneously, sometimes fuel can escape from the combustion chamber without ever being burned. Since a two stroke engine fires on each revolution it can theoretically produce twice the power of a four stroke engine at any given speed.

Two stroke engines' performance is predicted with either the Otto, or Diesel cycle, depending on the type of ignition the engines use. Diesel is commonly known as compression ignition as the gasses are compressed to the point they auto ignite, which

Figure 24 - Diesel Cycle

then drives the next revolution of the engine. The figure to the right shows the P-V diagram of the ideal Diesel cycle. Combustion is represented as constant pressure heating in segment 1-2, the retraction of the piston from top dead center (TDC) is modeled as an adiabatic expansion in segment 2-3, segment 3-4 simulates the exhaust of hot gasses, and the addition of a cool air charge, and finally 4-1 is the adiabatic compression stroke of the engine. Using common ideal gas relations the overall efficiency of the diesel cycle can be reduced to the following expression:

$$\eta_{th} = 1 - \frac{1}{\gamma}\frac{1}{r_c^{\gamma-1}}\left[\frac{r_t^{\gamma}-1}{r_t-1}\right]$$

Where $r_c = \frac{V_2}{V_1}$ and $r_t = \frac{T_2}{T_1}$

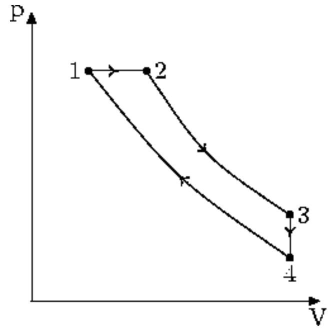

The above diesel cycle efficiency equations show cycle efficiency is dependent on both the compression and cutoff ratio. Efficiency increases with compression ratio and decreases with cutoff ratio. It is important to consider that in Carbureted, or throttle body injected diesel engines, the fuel air mix will spontaneously combust at a certain compression ratio that forces the mixture to its auto ignition temperature. To raise the compression ratio beyond that point, the use of a fuel injection system is required to prevent the cylinder from prematurely combusting. The cutoff ratio is simply the volume ratio that the combustion process is assumed to occur across. As the cutoff ratio increases the cycle power also increases, but at the cost of efficiency.

The Otto Cycle's combustion process is assumed to occur at constant volume, which greatly simplifies the governing efficiency formula. The formula is only dependent on the compression ratio of the system as a result of the combustion assumption.

$$\eta_{th} = 1 - r_c^{1-\gamma}$$

Where $r_c = \frac{V_2}{V_1}$ and $\gamma = \frac{C_p}{C_v}$

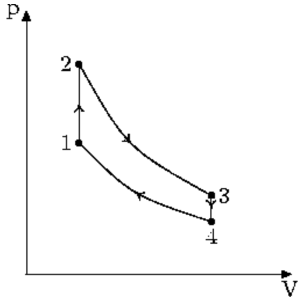

A third type of theoretical approximation is used to better simulate what a real P-V diagram performs like. In this dual cycle process combustion takes place at both constant volume and constant pressure segments to better represent real life combustion processes.

$$\eta_{th} = 1 - \left(\frac{1}{r_c}\right)^{\gamma-1}\left[\frac{\alpha\beta^{\gamma} - 1}{(\alpha - 1) + \gamma\alpha(\beta - 1)}\right]$$

Where $\alpha = \frac{P_3}{P_2}$ and $\beta = \frac{V_3}{B_{2.5}}$

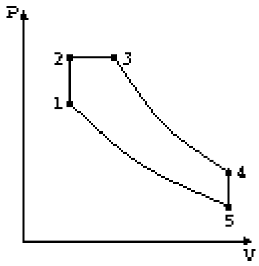

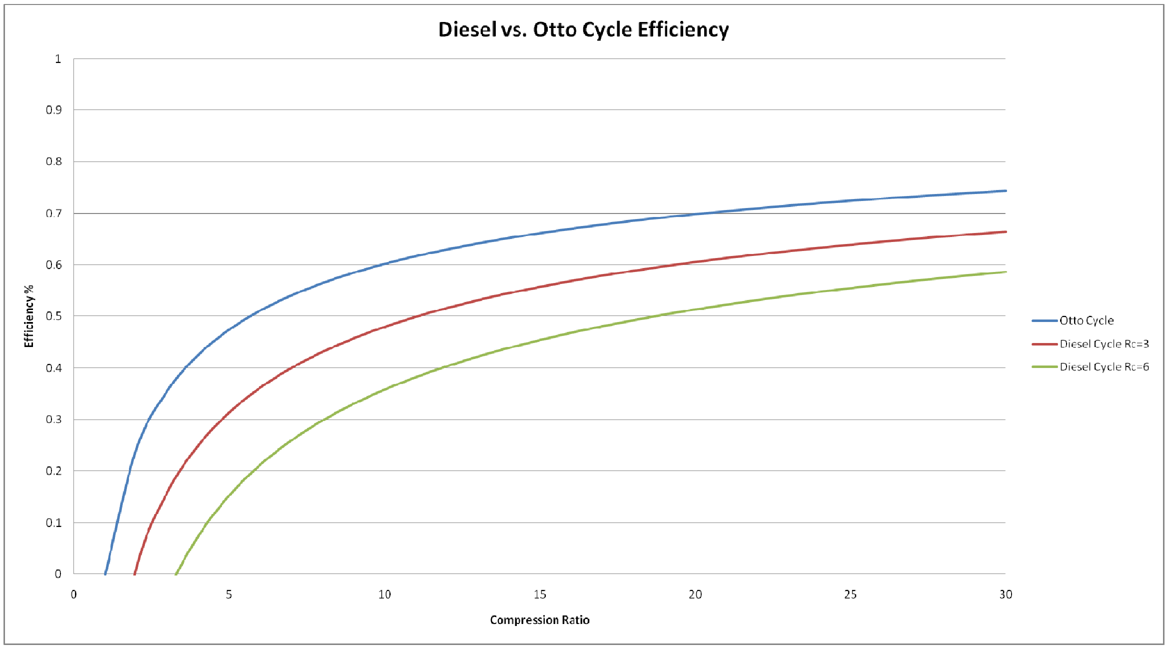

Figure 25 - Variation of Efficiency in Thermodynamic Cycles

The above chart shows the theoretical limit to the efficiency of both the Otto and Diesel Cycles. It can be seen that as the cutoff ratio of the diesel cycle increases, its efficiency for a given compression ratio decreases. Also, the efficiency for an Otto cycle engine is higher than that of a diesel cycle engine at the same compression ratio.

4 Stroke Combustion Engine

TRL 9

Four stroke engines are represented by the same cycle as two stroke engines, but with the addition of an extra "loop" that represents the intake and exhaust strokes of the engine. While the cycle representation would lead one to think the engines are very

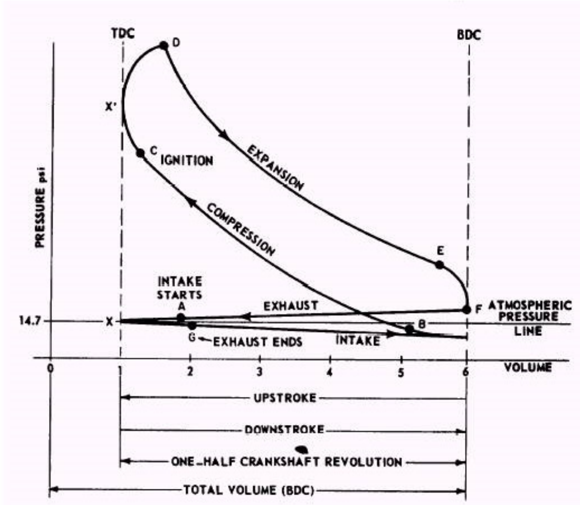

Figure 26 - Four Stroke Otto Cycle (tpub)

similar, their power, fuel efficiency, and adherence to the assumed model are vastly different. The main cause of all three differences is a result of scavenging. Scavenging is the ability of an engine to remove all the previously combusted material from the combustion chamber and replace it with new fuel air mix. In the diagram of a two stroke engine below, one can see that the piston controls the opening of the intake and exhaust ports, which are really nothing more than holes in the piston sleeve, precisely cut to allow flow at the proper times of the cycle. Since the two stroke engine ignites each revolution, the entire exhaust of old products, and intake of new mixture must occur in the fraction of a second the piston is near bottom dead center. If the ports on a two stroke engine were cut to allow flow over an angle of 90 degrees, at 10,000 RPM the total time for gas flow would be 1.5 milliseconds. This leads to imperfect exchange of gasses, with some exhaust products remaining in the cylinder and some unburned fuel passing through straight to the exhaust. Another downside to two stroke engines is their fuel must be diluted with lubricants since the crankcase is being utilized to compress the incoming mixture charge. While oil can be applied through a separate opening, there is no way to prevent a two stroke engine's lubricant from being swept away with the combustion products.

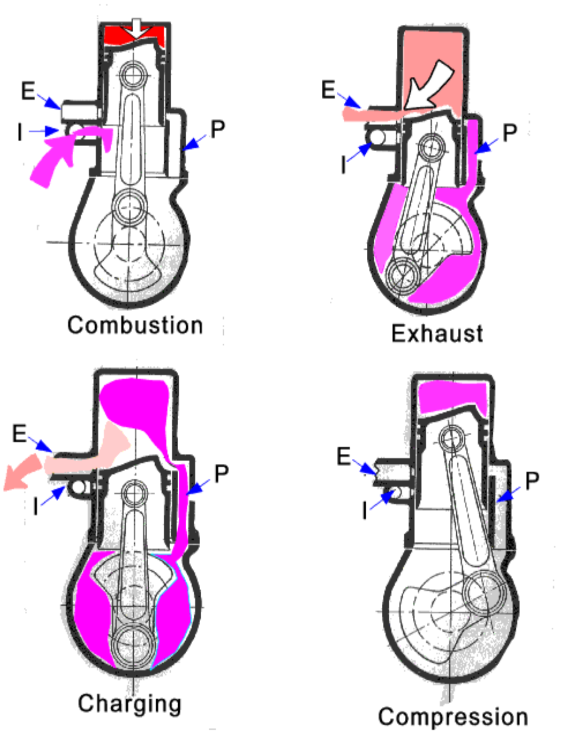

Figure 27 - Two Stroke Engine Schematic (roymech.co.uk)

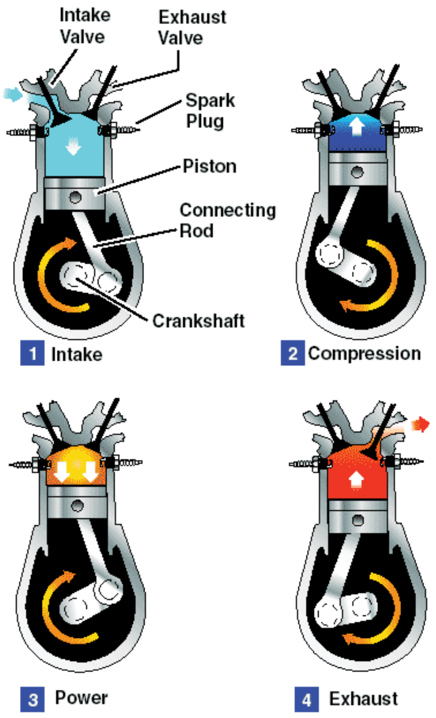

Figure 28 - Four Stroke Engine Schematic

With a four stroke engine, one complete revolution is dedicated to scavenging, with the intake and exhaust valves opening at separate times to help prevent unburned fuel from passing straight through the engine. Although some pressurization occurs due to exhaust valve restriction, one could assume that a volume proportional to the compression ratio of the engine is successfully scavenged in each revolution of a four stroke engine. This scavenging improvement over two stroke engines results in an immediate efficiency gain, and also allows for the implementation of a sealed lubrication system. Since four stroke engines do not use the interior of the crankcase to pressurize the incoming fuel charge, the varying internal pressure in the case can be used in combination with two one way valves to pump oil through the engine. This eliminates the requirement that the incoming fuel be mixed with oil that reduces the overall systems energy density.

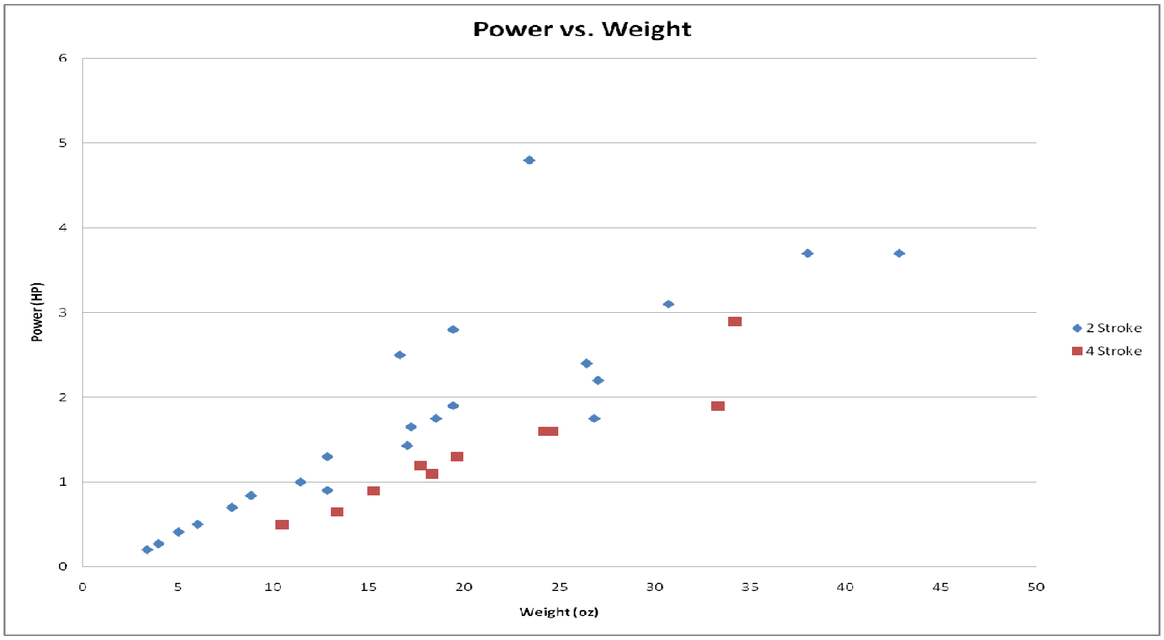

Figure 29 - Relative Power of Two and Four Stroke Miniature engines.

The relative manufacturers rated power levels for two and four stroke engines can be seen above. Although two stroke engines often are able to spin faster due to their reduced part count, and even though they combust every revolution as compared to four stroke's combusting every other revolution, the power of two stroke engines is only 1.5 times that of four stroke engines when trend lines are applied to the above plot and compared.

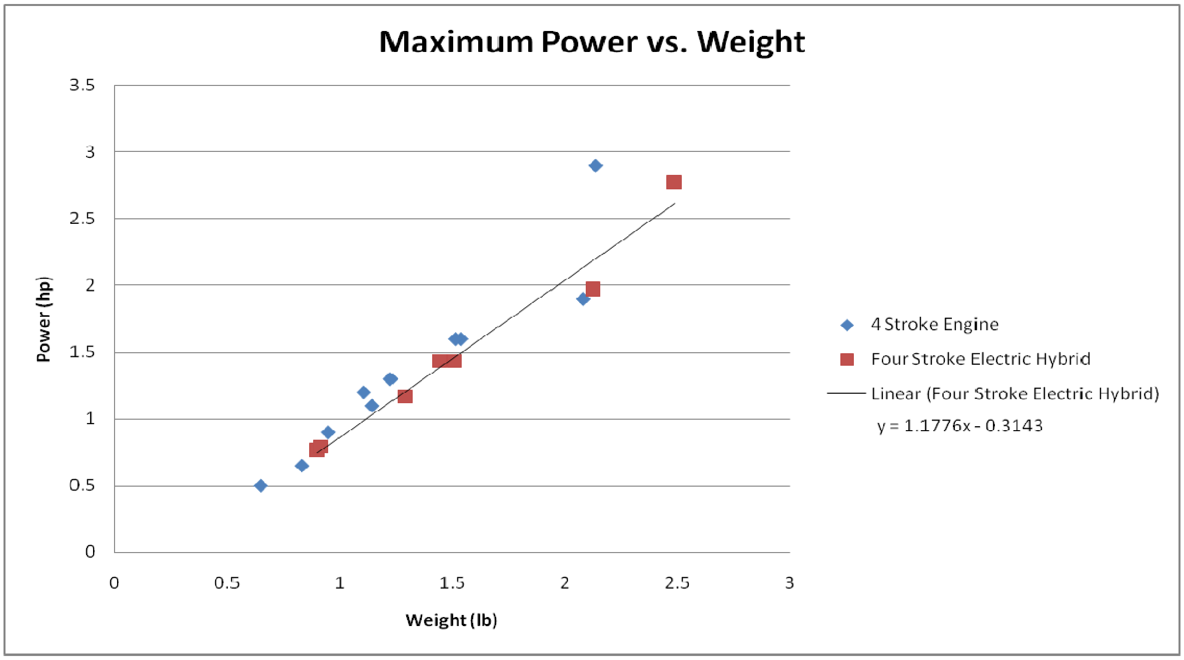

Figure 30 - Power to Weight Ratio of Pure and Hybrid 4 Stroke Engines.

One danger associated with using combustion engines is if the cycle every breaks down and the engine stops, they cannot be simply self started. In the case of aircraft one could command a dive to attempt to spin the engine by generating power from the propeller, but present autopilots do not possess that level of sophistication and without proper communication between engine management software and the autopilot, the engine may not even restart. To increase reliability, and allow for short periods of flight with the engine turned off, one could include a high efficiency electric motor in the engine design to act as a starter and generator. Interestingly enough, the power to weight ratio of modern batteries and motors is high enough that the overall power to weight ratio of four stroke engines is unaffected by the addition of the hybrid equipment. The system loses its continuous max power ability, but gains the ability to fly quietly and restart itself in the case of a malfunction.

HCCI Diesel Engine

TRL 4

Homogeneous Charge Compression Ignition engines rely on the natural temperature rise of the fuel air mix as it is compressed to create a uniform auto ignition event. This spontaneous combustion originates from several parts of the compressed volume simultaneously causing the flame front inside the combustion chamber to consume all available fuel more rapidly. This in turn results in a more concentrated impulse to the piston, higher peak temperatures, and overall greater fuel economy and efficiency.

HCCI engines are similar to diesel engines but vary greatly in the way the charge is ignited. In a diesel engine, fuel is injected into air that is already above its auto ignition point. This results in a travelling wave front as fuel meets unburned air. In an HCCI engine the fuel is already homogeneously mixed with air as in a spark ignition engine, but the cycle relies on compression alone to ignite the fuel. Since there is no single point of origin for the explosion, the impulse is very short. HCCI engines are tolerant of lean fuel to air ratio's, and are resistant to quenching as a result of multiple ignition points. This makes them ideal candidates for small engines. Aerodyne Research Inc. has studied, and is continuing to work on a small oscillating piston, linear generator. This engine operates on HCCI ignition techniques, and is targeted as a replacement for batteries. The ignition timing on HCCI engines like Aerodyne's can be difficult to control since it is not a triggered event.

Figure 31 - Aerodyne HCCI engine

The internal pressure, temperature of the incoming fuel, and density of the operating air, all affect the ignition angle.

Stirling Engine

TRL 7

Stirling engines are a very high efficiency, low specific power, external combustion engine. The stirling engine's cycle closely approximates that of an ideal Carnot cycle engine which results in its cycle efficiency being close the theoretical limit for heat engines. The idealized stirling engine cycle passes through the following phases as shown in the figure below. Segment 1-2 indicates the isothermal expansion of the operating fluid as it is stored in the predominantly hot region of the engine. Segment 2-3 is represented as constant volume (isovolumetric) heat removal, it is at this point that the operating gas passes through the engine's regenerator. Point 3-4 is where the fluid rejects heat to the cold portion of the engine, and as a result undergoes isothermal compression. Finally 4-1 indicates the gas' path back through the regenerator where it absorbs heat and expands isovolumetrically.

Stirling engines are of particular interest to aircraft, especially those that operate at high altitude. Most thermodynamic engine research attempts to raise efficiency by increasing the maximum temperature of the cycle after all but accepting a cold reservoir temperature near ambient. Stirling engines at high altitude utilize the colder thermal reservoir to increase cycle efficiency, while not losing any power since their operating fluid is entirely self contained. The only reduction in power with altitude would occur as the burner could no longer deliver adequate heat to the hot side of the engine as a result of available oxygen dwindling.

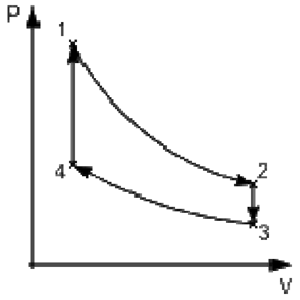

Although the idealized stirling cycle duplicates the Carnot cycle identically, a practical stirling engine's operation varies greatly from this assumed model. Problems with imperfect heat exchangers, mechanical and fluid friction, imperfect operating gas effects, etc. result in Stirling engines operating at peak efficiencies between 28 and 36 percent. The plot below shows the power and efficiency curve for a Sunpower EE-35 stirling engine. Note that the peak efficiency of the engine is just over 30%. At the given hot and cold reservoir temperatures of 650 and 80 degrees Celsius, an ideal Carnot cycle could achieve an efficiency of 62%. This demonstrates how poorly the idealized stirling cycle predicts the engine's true operation. Stirling engines are capable of running on any heat source. Engines have been demonstrated while running on JP-8, wood chips, organic compounds, and concentrated solar energy.

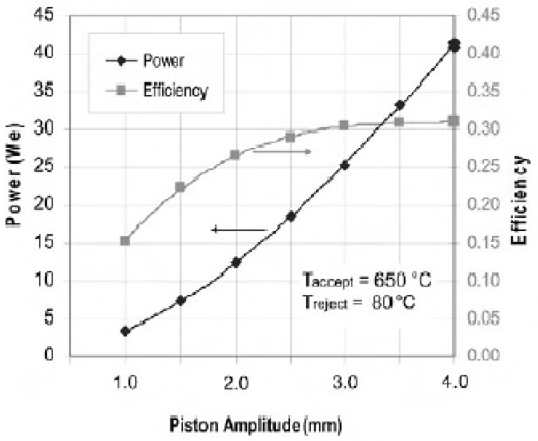

Figure 32 - Power and Efficiency vs. Piston Amplitude (Sunpower)

Stirling engines have many common configurations that are referred to as Alpha, Beta, and Gamma. The cycle remains the same in each type, but the driving mechanism is much different. Alpha type stirling engines use a hot and cold cylinder connected by a tube for the operating fluid to pass through. This configuration exhibits large dead space as a result of the connecting tube. Dead space is undesirable because any fluid that remains in the connecting tube is not being utilized to make power, and is a useless absorber of heat energy. The alpha type engine is difficult to implement at high temperatures as the seals of the hot piston must then survive the constant high temperatures without leaking. One advantage of having such a long connecting path between the hot and cold regions is that the two thermal reservoirs remain better isolated to increase the practical cycle efficiency.

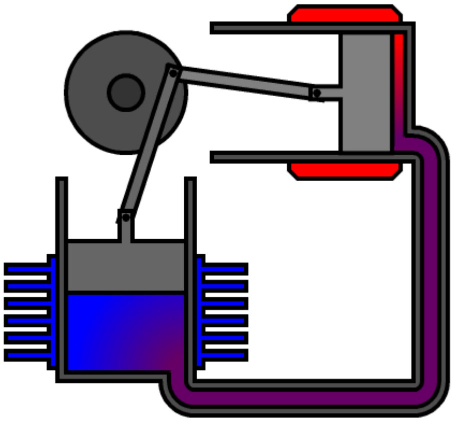

Figure 33 - Alpha Stirling Engine

Beta type stirling engines use coaxial pistons with one acting to change the overall volume of the operating fluid, and the other displacing that fluid between the hot and cold regions of the engine. since the hot and cold regions are connected by the cylinder wall, this type of engine looses more heat due to the thermal reservoirs being "short circuited". The top piston in the diagram below must be tight fitting to prevent the operating fluid from leaking. While the bottom displacement piston is intentionally gapped to force fluid between the hot and cold regions.

Gamma type stirling engines are the same as beta type, except the power piston (top piston in the engine below) is placed in a separate cylinder that is connected pneumatically to the main engine body.

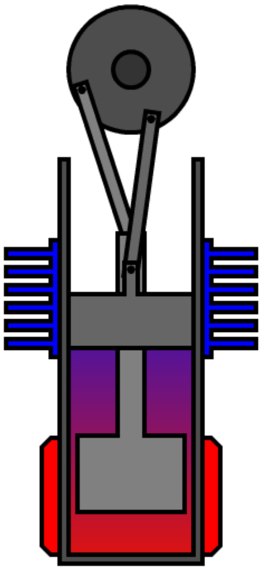

Figure 34 - Beta Type Stirling Engine

Free piston stirling engines are mainly used in environments where reliability, and long term performance are more important than power output, and weight. As the name implies, this type of stirling engine lets the power piston move freely through the use of fluid bearings, or planar springs. Most free piston sterling engine research has been conducted by the company Sunpower Inc. under a NASA small business innovation grant. Many other companies have either spun off from Sunpower, or licensed their technology to apply it to combined heat and power systems, or refrigeration. The free piston stirling engine is quite efficient, and runs very quietly. One drawback to FPSE's is that the power piston only oscillates a few millimeters, making power extraction rather difficult. The larger, and thus heavier, portion of most FPSE's is the linear alternator that is used to extract power from the oscillating piston. While the alternator itself is electrically efficient, the linear generator design coupled with small oscillations, results in the generator being heavier than a typical rotary brushless type design. The number of windings must be increased in a linear type generator versus a typical rotary generator to compensate for the reduced magnet movement.

Sunpower's current stirling engines represent the most advanced stirling engines to date. They were designed for operating in space from radioactive heat, which makes them nearly impervious to outside conditions, tolerant of considerable shock loads, and widely adaptable. Sunpower currently offers 42 W to 1 KW stirling generators, all with efficiencies greater than 32%, but power densities ranging from 11 to 43 W/lb. For comparison, the power density of the top lithium polymer batteries is on the order of 1,500 W/lb.

Figure 35 - Free Piston Stirling Engine Cutaway

Operating fluids.

Since the stirling engine is a closed cycle with external heating, the designer can select any working fluid he or she desires. It is desirable that the gas have a low heat capacity so that a small change in temperature produces a large change in pressure. Hydrogen is an excellent theoretical choice for stirling power because of its high thermal conductivity it will produce the most powerful engine per unit volume. However, hydrogen at high temperatures will diffuse directly through the metal that is meant to enclose it. Also, if air ever leaks into the operating space, there is a risk of explosion. Most top tier stirling engines use Helium because it gives nearly the same efficiency and power density as hydrogen, but with the advantages of an inert gas, and one that is much easier to contain. Air is another common working fluid, but aside from being less powerful, and less efficient, when combined with some lubricating oils the oxygen in air can ignite and turn the pressure vessel of a sealed stirling engine into a bomb.

Microturbines

TRL 4

turbines are the main source of power for most all modern full size aircraft, so it is no wonder that research is being conducted to miniaturize turbines to generate tens of watts instead of megawatts. With hobby industry turbines lacking the materials, and pressure ratio's necessary to exceed approximately 6% efficiency, many groups are looking raise both those parameters to deliver lightweight and efficient energy conversion. Micro turbines have many issues to resolve before they become practical power alternatives. First, as size decreases the speed required to achieve any appreciable power increases rapidly. Micro turbines routinely spin at hundreds of thousands of rotations per minute, with some approaching one million RPM. The high rotational speed requires the use of fluid micro bearings, and is limited by the tensile strength of the turbine blades as they try to rip themselves from the spinning shaft. Also once the turbine is working, the problem of developing a generator on the same scale, and capable of the same high speeds, is a problem that has yet to be solved.

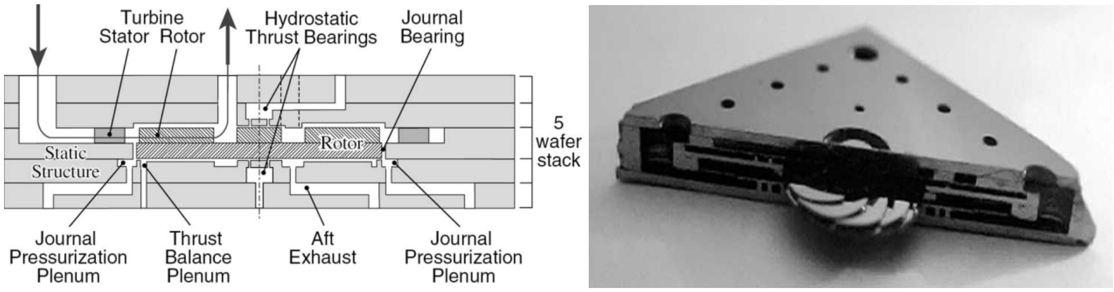

Figure 36 - MIT micro turbine schematic

The most publicized micro turbine project is the MIT "engine on a chip". This research group is attempting to utilize layered silicon manufacturing techniques to create a type of planar turbine that could be coupled to a similarly sized radial generator with future research. Dr. Alan Epstein comments that in his work on the micro turbines the most difficult problems have been "Understanding the interaction between manufacturing precision and rotor-bearing performance, and managing the tradeoffs between design requirements". He later goes on to say that on the smallest turbines "it is viscous forces in the air which cause the engine performance to rapidly drop off at sizes smaller than about a millimeter". The first applications for the MIT's army sponsored micro turbines will be in military laptops providing 10-50 watts of power.

Figure 37 - Microturbine shaft (Peirs)

Another slightly larger micro turbine research team in Belgium has tested a micro turbine to 16% total fuel to electric efficiency at an output power of 44 watts. The total rotor diameter of this micro turbine is only 10mm, and it has been tested up to 160,000 RPM with higher speeds out of reach due to bearing problems.

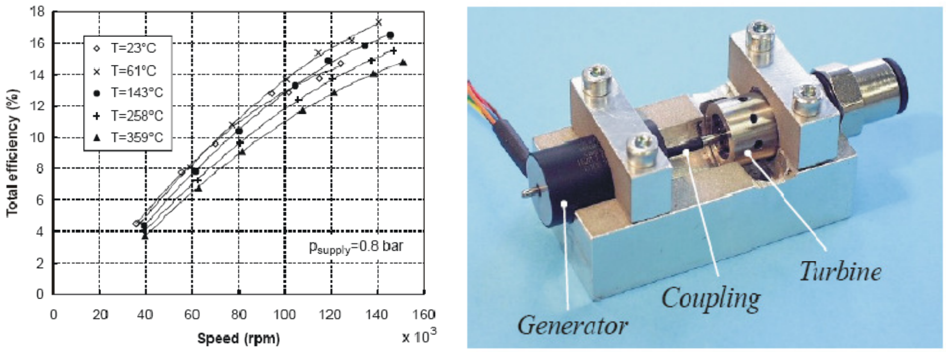

Figure 38 - Belgian micro turbine efficiency vs. RPM

Conversion System Comparison

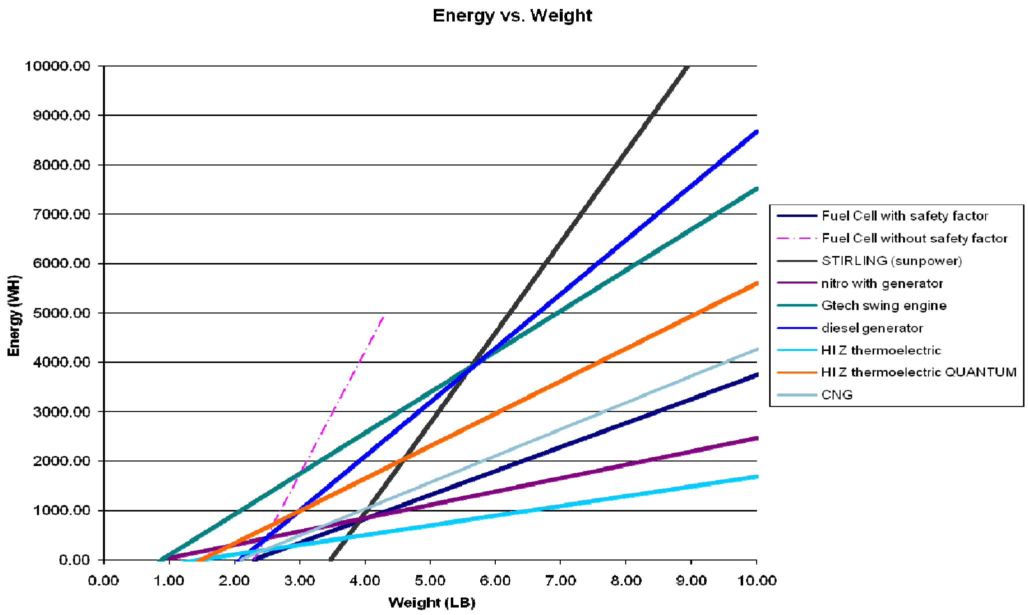

Figure 39 - Conversion Based Energy Systems - Energy vs. Weight

When all conversion systems are placed on the same plot, their seemingly vast differences in operating fuels, conversion methods, and cycle types disappear into a simple linear relationship that is dependent on only three things. The system's buy in weight affects its x axis intercept, the fuel type and the efficiency of conversion both go into determining the slope of the line when plotted against weight. A system made with Hi-Z's thermoelectric conversion devices would be very light since the only components would be a burner and heat transfer chamber. But, the relative inefficiency of conversion gives that system one of the lowest energy densities on the table. An energy system made with Sunpower's Stirling engine would be very energy dense as a result of the cycle's high efficiency, and ability to operate off of nearly any heat source. The surprising result of the above plot is that fuel cells do not outperform their hydrocarbon competition. The weight associated with storing hydrogen at any considerable weight fraction erases the energy density advantage of the fuel, and the efficiency advantage of fuel cells. The energy density losses of several types of hydrogen storage and a general fossil fuel storage device are shown below.

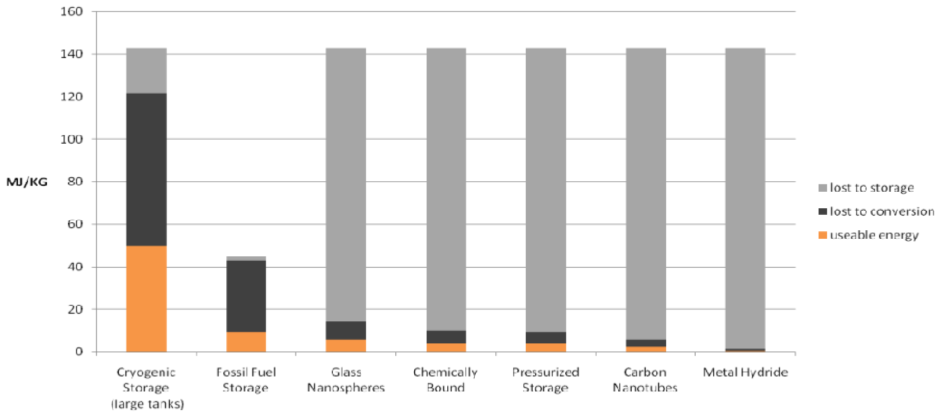

Figure 40 - Energy Density Losses of Various Systems

As discussed previously, cryogenic hydrogen storage is by far the most dense energy storage method, but cannot be successfully implemented on small aircraft less than 20 lb. due to the weight of hardware required to keep the hydrogen cool. Every other hydrogen based option has such a low mass fraction of useable hydrogen that traditional fossil fuel storage becomes the preferred option. Even after generator losses the two top performing options are Stirling, and Diesel engines. The Stirling engine was conceived in 1816, the diesel engine patented in 1898, and their modern evolutions continue to outperform newer more “advanced” technologies.

Energy System Comparison

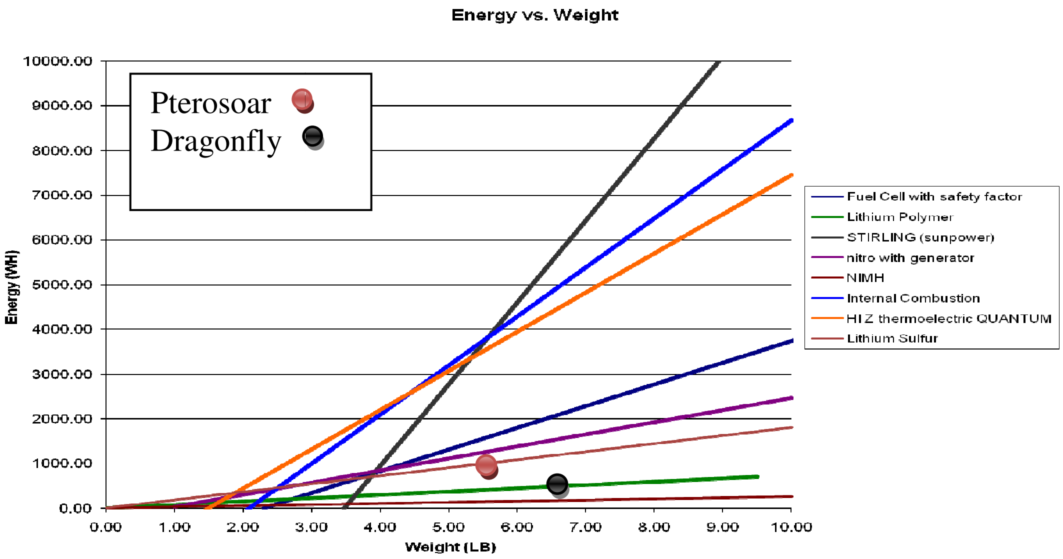

Figure 41 - Energy of Selected Systems

The figure above shows the most feasible system plotted against one another. This plot shows that lithium polymer batteries, which are the present SUAV standard, have a very low energy density when compared to other SUAV power options. For applications below 1.75 lbs, they are still however the best because of their lack of buy in weight. The maximum stored energy for any given system as a function of weight can be approximated between zero and ten pounds by the parabolic function:

One other useful way of comparing energy systems is to look at their relative power densities, and energy densities. As can be seen in the chart below the most energy dense systems often lack power, and the most powerful systems lack energy. It is because of these design restrictions that hybrid power systems have gained popularity in the past years. A system combining a stirling engine as a cruise power generator, and high power lithium batteries as the maneuvering power source could theoretically approach the maximum energy density and power density of both energy systems. Such hybrid systems must be used strategically so that the high power source never becomes depleted. The Aerovironment Puma fuel cell demonstration vehicle was forced to land prematurely as its high power lithium battery became depleted before the fuel cell used all available fuel.

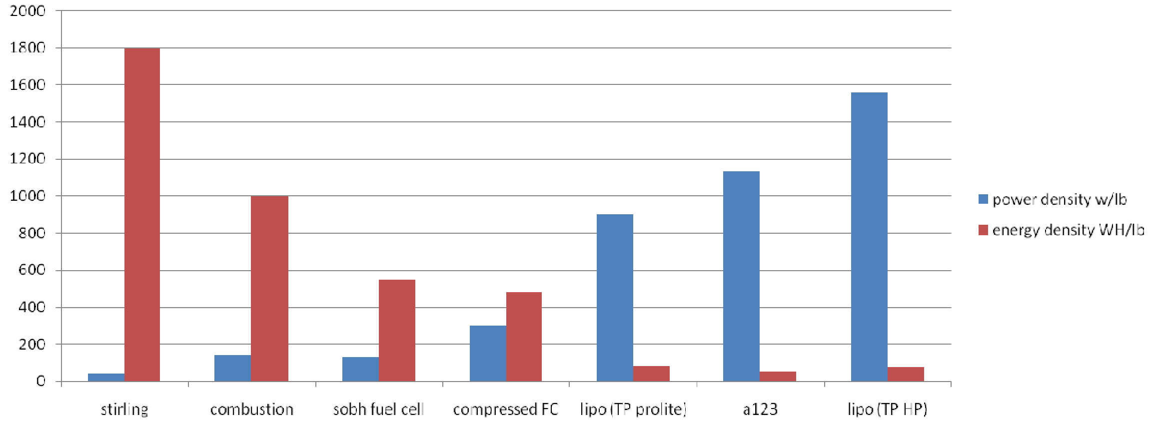

Figure 42 - Power Density vs. Energy Density of Several Common Sources

	power density w/lb	energy density WH/lb
stirling	40	1800
combustion	140	1000
sobh fuel cell	130	545
compressed FC	300	486
lipo (TP prolite)	900	79
a123	1135	50
lipo (TP HP)	1560	74

CHAPTER IV

SMALL ENGINE DYNAMOMETER

After conducting the broad scope energy system survey, it was decided that combustion engines would be the most appropriate high energy density system for UAV applications. This choice was based on combustion engines' high energy density (tested up to 1560 WH/lb by Aerosonde), their high specific power levels (250-1400 W/lb), and rotating shaft output. The rotating shaft was considered a plus because of its suitability to direct drive a propeller or impeller, and its compatibility with rotary generators, which have a higher specific power output than linear arrangements. An additional benefit to using a combustion engine is the plethora of research conducted on their larger brethren, which can be adopted to explain some of the dynamics of small scale engines. While the mechanics, and thermodynamic cycle are identical, the small scale brings much larger surface area to volume ratios. This change increases heat losses through the engine which results in reduced peak efficiency. Fluid flows through the engine are also heavily effected due to lower Reynolds numbers throughout the system. The largest reason for creating a small scale engine dynamometer was to enable engine performance to be quantified, and comparison of the effects of engine modifications.

The dynamometer was designed to test the energy density of various engines, which in turn requires the measurement of torque, RPM, and fuel flow. Torque is measured by a point load cell coupled to a known length moment arm on the engine side of the dynamometer. The engine mounting side was used to measure torque to ensure that torque contamination was minimized. Load torque measurements are often contaminated by the inefficiency of a coupler, bearing, pulley system, motor, etc... whereas mounting side load measurement is only contaminated by bearing friction and fuel line torque. Bearing friction can be minimized through the proper bearing choice combined with precision machining, while fuel line toque although very small to begin with, can be calibrated out as an approximately linear spring contamination. RPM is measured with an optical transducer that outputs a high logic level each time is "sees" the reflective tape on the engine shaft pass by. Fuel flow is averaged over time by continually acquiring samples from a sensitive digital balance, and then applying a linear curve fit to the resulting mass and time data. The low uncertainty of all three input measurements is essential to the final energy density value being sufficiently accurate.

The target engine class included any engine that could provide at least 200 watts of output power. This output power level was chosen as it is an average SUAV cruise power requirement. The RPM at which the power is delivered was not constrained as the output of the engine could be gear reduced before mating to the proper propeller for the specified application. The compatible RPM range has an indirect restriction based on the uncertainty of torque measurement which will be discussed further in the uncertainty subsection of this paper.

Small engine efficiency measurement provided a multitude of difficulties during the development of the project. The initial prototypes of the dynamometer and restraint parts did not account for the high energy vibrations that would pass through them and were quickly torn apart. Vibration continued to be the cause of nearly every problem with gathering data from engines. RPM measurement was the simplest to acquire accurately by using a microcontroller to average the duration of every 20 rising logic signals on the optical sensor channel. The microcontroller used had been tested to an accuracy of 4 microseconds, which results in very precise and accurate measurement of RPM. Torque measurement became very complicated in the presence of the vibration of a running engine. Many coupling types were tried along with several mounting systems, until the largest of the engine class meant to be tested on the dynamometer was steady and controllable on the dynamometer. Vibrations from the engine still excite the torque arm from 5000 to 6000 RPM making measurements in that RPM range unreliable. If that data range is essential, the removal of torque shaft ballast will allow the user to retune its natural frequency. Finally fuel flow was complicated by vibrations from the engine passing through the torque shaft, into the bearings, out of the support structure, through the carrying cart, and into the high sensitivity balance. To attenuate the high frequency vibrations from the engine, the entire balance and fuel reservoir was mounted on a low K spring table.

Operating Theory

The dynamometer uses standard formula's to calculate fuel flow, horsepower, and resulting energy density. But the algorithms concerning the uncertainty of these measurements, especially the origins of those used to reduce the uncertainty of averaged data, may not be so immediately apparent. The general formula's for horsepower, and a few useful relations are stated below: (note that all torques in formulas are assumed to be input in ft-lb's)

$$Horsepower = Torque \cdot \frac{RPM}{60} \cdot \frac{2\pi}{550}$$

The simplification of all constant multipliers results in the useful relation:

$$Horsepower = \frac{Torque \cdot RPM}{5252}$$

This means that at 5252 RPM the horsepower and torque value of any engine will be identical.

$$RPM = \frac{60}{t_d}$$

RPM is computed in the microcontrollers firmware as the average of 20 revolutions to reduce uncertainty, but the simplified period to RPM formulation is shown above.

Fuel Flow Rate

Fuel flow values for small engines can range anywhere from 0.3 grams per second of rc aircraft glow fuel, to .008 grams per second of Coleman fuel under maximum lean operation. While measuring such small fluid flow rates is possible with thermal fluid flow measurement devices like the omega FLR-1618A (1866$), such devices were prohibitively expensive for this unfunded dynamometer. In place of such expensive flow options, a scout pro 400 0.1 gram precision balance was used along with its optional USB data output to record fuel mass remaining over time. This data was then linearly fit to get average fuel flow rates over time. This method allows for extremely accurate and precise measurements at the expense of longer data acquisition times. A typical plot of fuel weight vs. time is shown below with its corresponding curve fit. Slope calculations are conducted in real time as data is gathered into lab view approximately each 1/4 second.

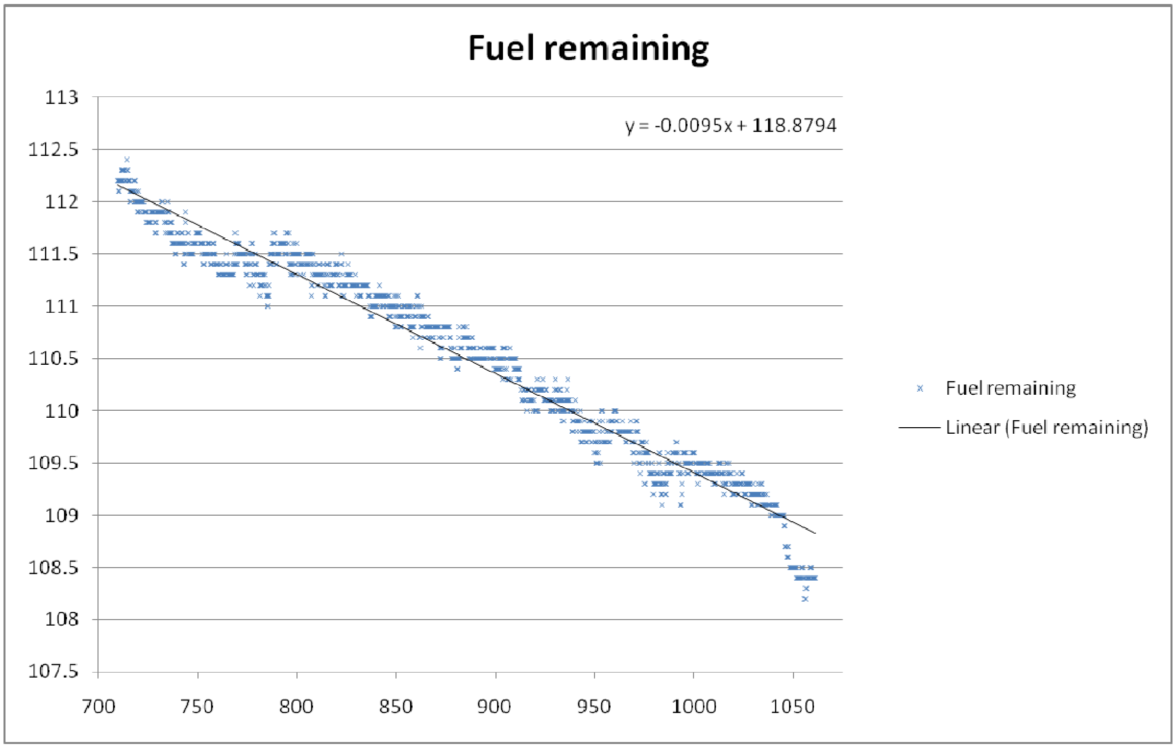

Figure 43 - Fuel Flow vs. Time

The Histogram below shows how the instantaneous mass is scattered around the linear fuel flow curve fit for four different test runs. As shown, the curve fit is seldom more than .2 grams off from the instantaneous fuel weight.

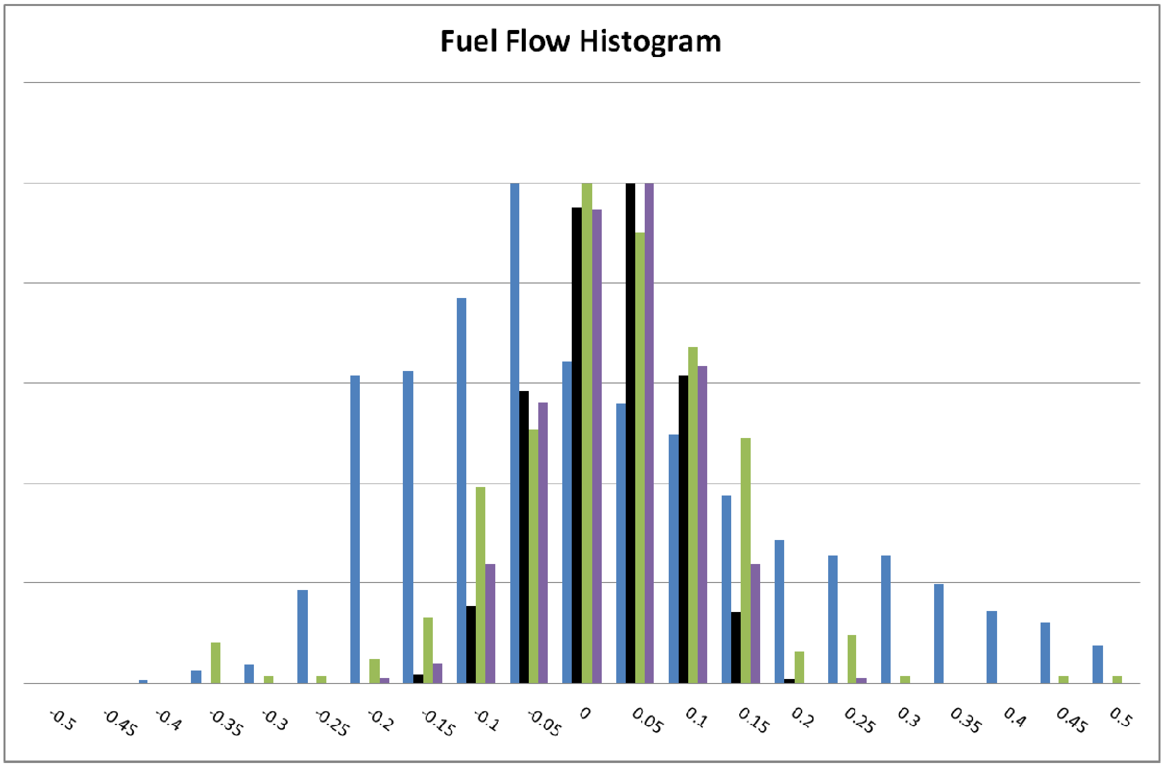

Figure 44 - Variance of fuel flow from linear average

Energy Density is calculated as the product of all preceding measurements, and as such has the highest uncertainty of all output values. To keep in the same output energy density units as the rest of this paper, (WH/lb) the calculation is conducted as follows:

(When FF is input in units of g/s)

where is in units of for most liquid hydrocarbon fuels.

Brake Mean Effective Pressure

Brake mean effective pressure (BMEP) is used as a way of characterizing the power output of each combustion cycle. While not a true nondimensionalization, it does allow for power comparisons between two and four stroke engines of variable displacement. BMEP is related to indicated MEP (IMEP), frictional MEP (FMEP), and pumping MEP (PMEP) by the following equation.

$$BMEP = IMEP - PMEP - FMEP$$

$$MEP = \frac{hp \cdot 33000 \cdot 12}{n \cdot V_d}$$

The above equation is useful in determining the power output of any given engine as FMEP is easily measured by driving the engine with an electric motor and measuring resistive torque (with the spark plug removed). IMEP and PMEP are most easily measured by taking an indicator diagram of the engine which results in the true PV map. The map's power and pumping regions can be integrated to give IMEP and PMEP respectively. If one is not able to measure the PV diagram of the engine to determine pumping losses, it is also acceptable to use the following equation to lump PMEP and FMEP into a single mechanical efficiency parameter.

$$\eta_{mech} = \frac{BMEP}{IMEP} = 1 - \frac{FMEP}{IMEP}$$

Resistive Load

An essential part of designing the dynamometer for small engine measurements, is designing the load to scale properly with such low outputs, and make the control of said load precise enough to maintain RPM, without becoming overly sensitive. The starter/generator motor used was an Astroflight cobalt 60 direct drive motor, This motor was chosen over a brushless option as efficiency was of no real concern, and its DC output simplifies load control. The load was passed through a high current PWM controller that would allow the duty cycle of the resistive load to be changed based upon the input signal to the Astroflight 204 D speed controller. Finally, four 0.5 Ohm 300 watt wire-wound resistors were used to dissipate the current generated to heat. Understanding the relation between torque and RPM for the complete engine, PWM controller, and resistor system is important for providing adequate control of an engine during testing. The equations governing power generation, dissipation, and resulting torque follow:

Astro Cobalt 60 Motor Parameters

RPM/Volt (Kv)	347
Resistance	0.103
Kt	3.89
Io	3

$$Generated\ Voltage = \frac{RPM}{K_v}$$

$$Current = \frac{V}{R_{resistors} + R_{motor}} + I_o$$

$$K_t = \frac{1352.4}{K_v}$$

$$Torque = I \cdot K_t = \frac{RPM \cdot K_t}{K_v(R_{resistors} + R_{motor})} + I_o K_t = \frac{RPM \cdot 1352.4}{K_v^2(R_{resistors} + R_{motor})} + I_o K_t$$

$$Horsepower = \frac{\left(\frac{RPM \cdot 1352.4}{K_v^2(R_{resistors} + R_{motor})} + I_o K_t\right) RPM}{1008384}$$

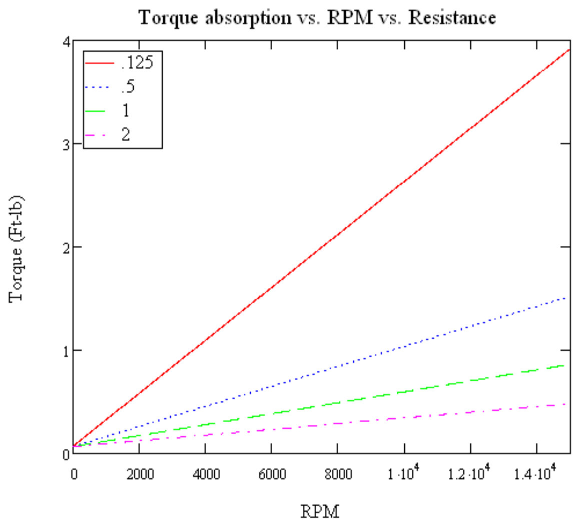

Figure 45 - Torque vs. RPM vs. Resistance

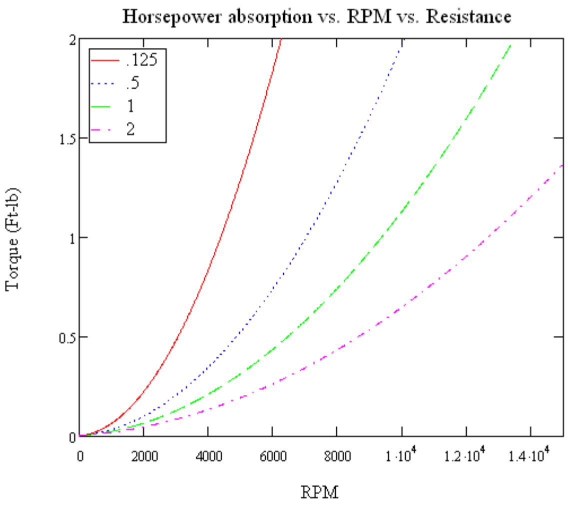

Figure 46 - Horsepower vs. RPM vs. Resistance

The above plots show the maximum torque and horsepower that the dynamometer in its current configuration can absorb for a given resistance. Lower bank resistance values increase the amount of current flowing for a given voltage, which in turn is proportional to RPM. Therefore it can be said that for a given RPM, lower resistance values will increase the torque on the motor. Since decreasing the duty cycle of the resistive load is equivalent to lowering its resistive value, one can simple use duty cycle to control the resistance to the engine shaft. It is vitally important to ensure that the resistance value selected will result in the motor absorbing more power than the engine produces at its maximum rated speed. If not, the engine will over speed and could be damaged. Since motor resistance rises exponentially, and engine power rises approximately linearly, the two would eventually come to steady state, but it could occur in a destructive sense. If the resistive value is set too high, the load becomes extremely sensitive to duty cycle making manual control of the engine difficult, and the portion of heat dissipated through the motor compared to that dissipated through the resistor bank increases. The plot below shows the relative percentage of heat dissipated in both the motor, and resistor bank. The crossover point occurs when $R_{bank} = R_{motor}$ in which case equal amounts of heat are dissipated in each. The total value of heat can be simply approximated as the output of the engine. Some energy is lost to the pulley system, and some in the wires and speed controller, but a safe estimate would be to split the power output of the engine at any given operating point proportionally in accordance with the chart below.

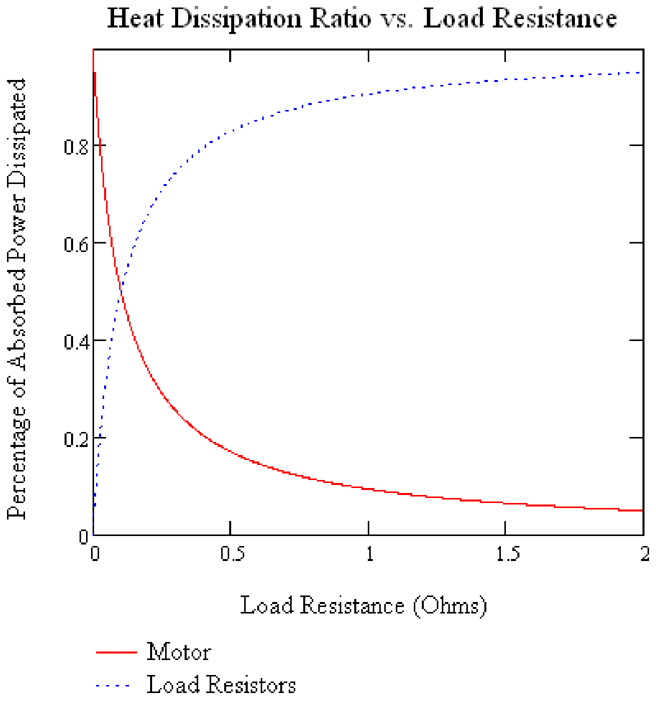

Figure 47 - Relative Heat Dissipation

The resistive load control operated as expected when first tested, but after a few hours of testing a diode on the speed controller used to modulate duty cycle of the resistor bank overheated and was destroyed. Assuming the controller was defective, a second was installed and met a similar fate after a short time of testing. The problem was traced to the natural inductance of the coils in the motor. When the MOSFETs in the speed controller switch the load on and off at 3Khz, this produces large current derivatives, which in accordance with the basic equation for inductors:

$$V = L\frac{\delta i(t)}{\delta t}$$

produces negative voltage spikes on the order of 500 volts, in an attempt to smooth current flow in the system. A P-spice simulation of the problem is shown below.

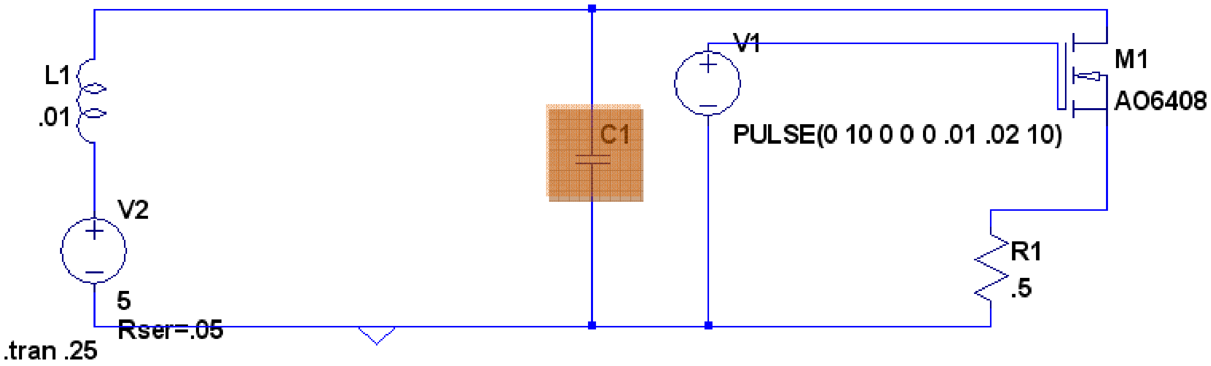

Figure 48 - Simplified MOSFET based speed controller representation

A schematic view of a basic MOSFET based speed controller shows the placement of the capacitor of interest. When C1 is much less than L1, the following voltage profile is seen on the main power lines through the controller.

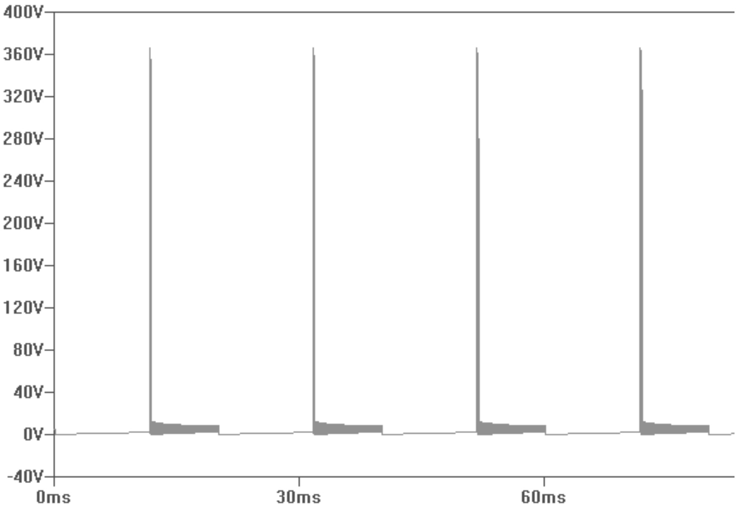

Figure 49 - Damaging High Voltage Spikes Resulting From Excessive Circuit Impedance

The large voltage spikes shown above were overloading the diode meant to protect the onboard circuitry from exactly this problem. Although the pulses are extremely short, it still resulted in excessive heat buildup in the main diode. The problem was resolved by replacing the moderate voltage, low capacitance stock capacitor with a high voltage, high capacitance part that successfully absorbs the voltage spikes as shown below.

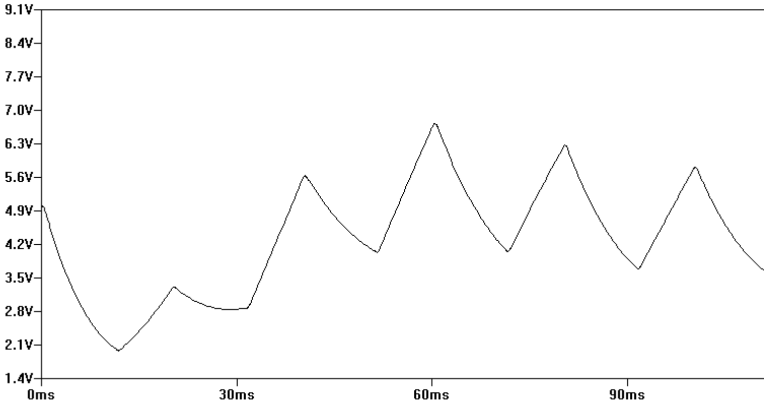

Figure 50 - Voltage Spikes After Adding Parallel Capacitance

Following the replacement of the inadequate stock capacitor, the replacement speed controller has worked flawlessly.

Uncertainty Calculations

Understanding how accurate one's measurements are is just as important as obtaining the measurements themselves. Great care was taken during the design of this dynamometer to ensure that uncertainty remained at a minimum while not overspending on increased sensitivity parts in areas where they were not needed. Understanding how uncertainty propagates from a single measured value, to values that are formed by many measured values, and based on many calibrations which each have their own uncertainty, is key to designing hardware wisely, and obtaining minimal uncertainty in all calculated parameters.

All measurements taken from the dynamometer are completely independent and the equations governing horsepower, torque, and energy density are simple functions of the form $\frac{x}{y}$ or xy which means the uncertainty formula is simply:

$$\sigma = \sqrt{\sigma_x^2 + \sigma_y^2}$$

Which is simply the RMS value of each individual measurement. This result is from a first order Taylor expansion of the function of interest around all input variables. The expanded version can be seen below: (Pengra and Wesleyan)

$$\sigma_f^2 = \sigma_x^2 \left(\frac{\delta f}{\delta x}\right)^2 + \sigma_y^2 \left(\frac{\delta f}{\delta y}\right)^2 + \sigma_z^2 \left(\frac{\delta f}{\delta z}\right)^2 + \cdots$$

Load Uncertainty

As with any load cell the minimum uncertainty can be achieved when the load applied to the cell nears the maximum rated load of that particular device. This design would minimize uncertainty, but maximize the chance of damage to the load cell. Also, transducer parameters like nonlinearity, hysterisis, non-repeatability, and zero balance all combine to govern the accuracy of each load cell. For the purposes of this small engine dynamometer, engine HP's were expected to be between 0.25 and 2 HP, and rotational speeds between 3,000 and 15,000 RPM. This range of power and speed would produce shaft torques ranging from 0.1 to 0.9 ft lb. The mount for the load cell allows it to move in or out depending on the maximum expected torque of the engine. For the case of an OS 40 four stroke engine with a maximum power output of 0.65 HP at 12,000 RPM. The load cell would optimally be placed 1.35 inches from the center of rotation to minimize uncertainty for the 2.5 lb load cell selected. The selection of this cell compared to other available types was based on its low maximum rated output, and minimal uncertainty. The cell is rated with the following parameters:

MDB 2.5 (Transducer Techniques)

Rated Output	2mV/V nominal
Nonlinearity	0.05% of RO (.5 g)
Hysteresis	0.05% of RO (.5 g)
Non-repeatability	0.05% of RO (.5 g)
Zero balance	1% of RO (11.35g)
Temperature Compensation	60 to 160 F
Excitation Voltage	Up to 10V
Safe Overload	150% of RO
Terminal resistance	350 ohms

Figure 51 - Transducer Techniques MDB 2.5 Load Cell

Since the load cell's ability to return to zero is only important when checking calibration after a data run, the actual measurement uncertainty on this load cell is on the order of $\pm 3\ g$ (0.25% to be conservative). Even if the zero balance rating of the cell is used, this still results in an uncertainty band of $\pm 11.3\ g$ (1%).

Because of the inability of the Transducer Techniques load cell to handle overload conditions, the load cell became damaged in testing even with all the protection measures taken and was replaced by a FUTEK FSH00001. This load cell is of comparable sensitivity, is 150 dollars cheaper, and most importantly has built in overload protection to 250 lbs. The load cell uses a statically indeterminate load condition to provide such a large overload protection. This load cell will be used in tension, and connected to the moment arm with 20 lb test fishing line. This will prevent eccentric loading since only tension can pass through the line, as well as provide a secondary overload barrier as the fishing line should break well before the load cell is overloaded. The specific numbers regarding the Futek load cell are given below:

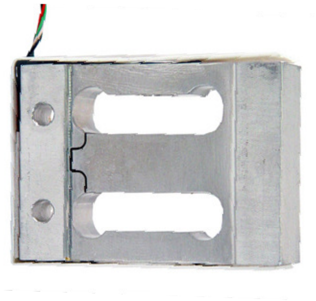

FUTEK FSH00001

Rated Output	2mV/V nominal
Nonlinearity	0.02% of RO (.5 g)
Hysteresis	0.02% of RO (.5 g)
Non-repeatability	0.02% of RO (.5 g)
Zero balance	3% of RO (11.35g)
Temperature Compensation	60 to 160 F
Excitation Voltage	Up to 18V
Safe Overload	**11364% of RO**
Terminal resistance	1120 ohms

Figure 52 - Futek FSH00001 Load Cell

Torque Uncertainty

Torque is the first parameter used that is not directly measured. The 1% uncertain load cell force measurement is combined with the uncertainty of the calibration torque, to obtain the overall uncertainty of the test torque measurements. The calibration torque application point was marked with a ground indention into the steel all thread rod, and then measured by wrapping a thin wire around the 2" diameter torque shaft and crossing and slicing its ends at the indentation in the all thread rod. The thin wire was used to bypass the uncertainty of trying to determine the center point of a shaft that is rigidly mounted on both ends of the region of interest. The overall length of the wire was measured with analog verneir calipers to an accuracy of ±0.0001 inches. The thickness of the magnet wire was assumed negligible with respect to the 1" radius it was turned around and therefore ignored. The resulting geometry is presented below.

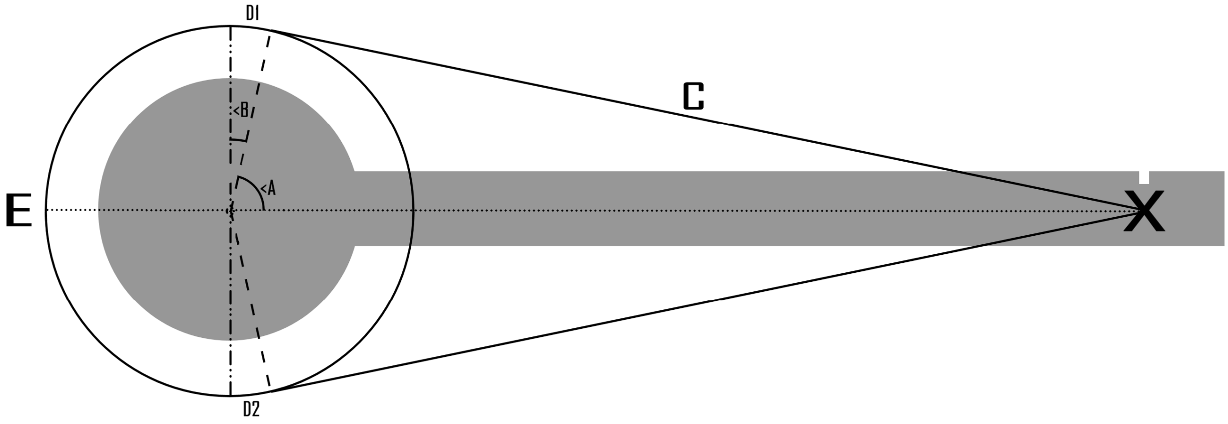

Figure 53 - Torque Arm Distance Measurement Diagram

The only measurements necessary to determine the distance from the center of the shaft to location X above are the total length of wire, and the diameter of the shaft. Every other dimension is dependent on those two. The wire is assumed to depart from the main torque shaft tangentially, and to cross precisely at the center of the notched portion of the all thread rod. The length of wire around the shaft can be determined by the relation:

$$L_{shaft} = \frac{180 + 2B}{360} \cdot \pi \cdot D_{shaft}$$

The length of wire along segment C from the detachment point from the shaft, and the crossing at the ground notch is defined below:

$$L_C = \cos\left(\operatorname{atan}\left(\frac{r_{shaft}}{C}\right)\right) \cdot X$$

Making the entire length of wire equal to the following expression:

$$L_{wire} = \left[L_{shaft} + 2L_C\right] = \frac{180 + 2B}{360} \cdot \pi D_{shaft} + \cos\left(\operatorname{atan}\left(\frac{r_{shaft}}{C}\right)\right) \cdot 2X$$

The above equation was numerically solved for distance X, from the center of the torque shaft, to the notch in the all thread rod. Once that distance was known, it allowed for a triple point calibration before each run of the dynamometer. The load readings are recorded as a 200, 100, and zero gram mass is hung from the notch. These recorded loads are compared with what the theoretical torque would be for such an applied mass at a known distance, and a calibration curve formed. The linear curve fit of the calibration curve gives the necessary offset and scaling factors to produce valid torque outputs. The current calibration method results in consistent ± 0.005 ft-lb accuracy, with results oftentimes exceeding that mark. However, these calibrations occur statically and cannot account for systematic error encountered due to the dynamics of the engine test stand.

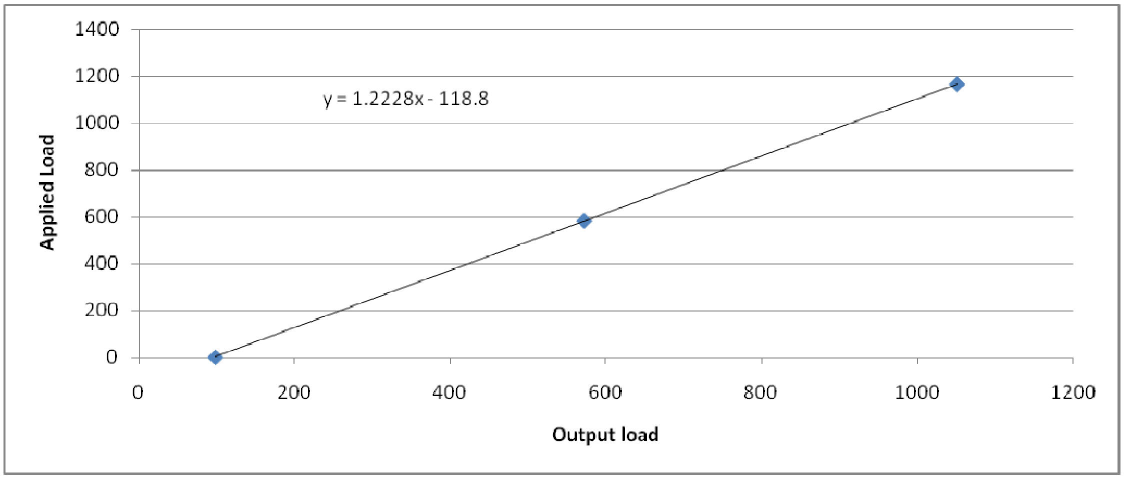

Figure 54 - Load cell calibration curve

The highly sensitive load cell is prone to damage if directly attached to the engine torque arm, especially when running the engine with additional flywheel balancing. If the engine were to seize, the energy stored in the flywheel would be dissipated through the load cell and surely exceed its maximum safe rating many times over thus destroying the load cell. To protect one of the costliest parts of the dynamometer, a spring was used in combination with a displacement stop to magnify the allowable strain of the load cell and prevent the cell from ever being overloaded. A force vs. displacement representation would appear as shown below, with the spring region having a very low modulus, and the rotational stiffness increasing nearly infinitely as the torque arm impacts the high end stop of the dynamometer.

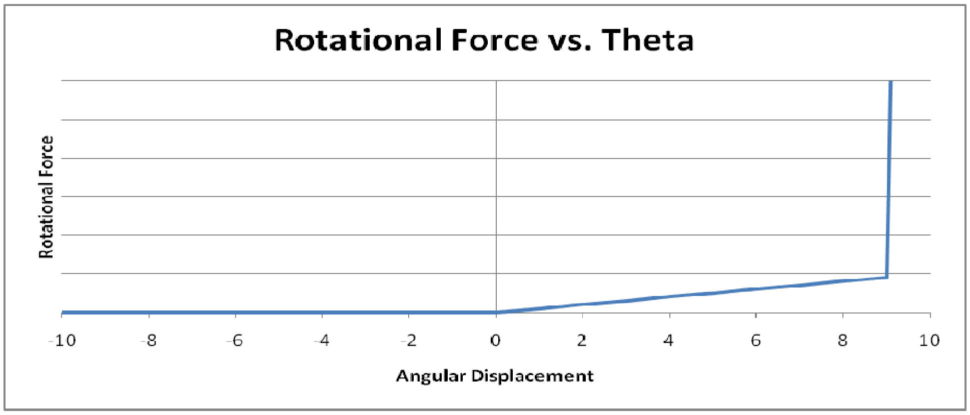

Figure 55 - Force vs. Displacement curve

While this setup ensures the safety of the load cell, it also adds complication to the dynamics of the system. Since the engine mounting shaft is now free to rotate through a small angle, it is possible that vibration could cause the bearings to have a preferred direction and impart a small anomalous torque. Secondly, care must be taken that the spring is stiff enough that it does not bottom out under maximum engine torque, and yet loose enough that the travel stops are possible to create. One could use the natural displacement of the load cell in the exact manner proposed previously, but the stops between zero load, and maximum load would be .004 inches apart based on the rated strain of the load cell used.

The stiffness of the spring used is also limited by the filtering characteristics it is meant to apply to the system. The spring setup is in effect a low pass filter with hard limits on its maximum and minimum outputs. if the spring is too stiff it will start to pass higher frequency vibrations through to the load cell and uncertainty will increase.

One must also be careful to constrain the connection between torque arm and load cell properly. If the spring's contact point travels during testing, then the moment arm length changes by a corresponding amount. Presently, the connection is held in place by a small diameter pit drilled into the moment arm, this allows repeatable measurements, ensures consistency during testing, and prevents negative overload on the load cell.

Considering all the above, the torque measurements uncertainty is the combination of the load cell's uncertainty, the constant moment arm length uncertainty, and the uncertainty in the calibration weights. The total uncertainty of the torque measurement is given by the following equation.

$$Torque\ Uncertainty = \sqrt{\left[\frac{\sigma_{loadcell\%}\cdot RO_{loadcell}}{Load}\right]^2+\left[\frac{\sigma_{calibration\ mass}}{m_{calibration\ mass}}\right]^2+\left[\frac{\sigma_{moment\ arm}}{L_{moment\ arm}}\right]^2}$$

Which for the present setup of the dynamometer gives:

$$Torque\ Uncertainty = \sqrt{\left[\frac{0.01\cdot 2.5}{Load}\right]^2+\left[\frac{0.1(g)}{201.3(g)}\right]^2+\left[\frac{.005(in)}{14.12(in)}\right]^2}$$

$$Torque\ Uncertainty = \sqrt{\left[\frac{0.025}{Load}\right]^2+3.7217E^{-7}}$$

RPM uncertainty

RPM measurements are simplified by the use of a microcontroller to count revolutions, and time the period between a set number of peaks. Currently the controller is configured to save the start time in microseconds at the first high input from the optical sensor, count the passing of the next nineteen high pulses, and then record the time in microseconds from board initialization of the 20th high pulse. This time delay is accurate to four microseconds, and the averaging over twenty samples gives an effective resolution of 200 nanoseconds. The percent uncertainty, and actual RPM uncertainty are calculated in the following manner:

The doubling of the timestamp resolution is a result of the two timestamp measurements that are necessary to determine RPM.

When applied to a 16 Mhz Arduino microcontroller with 4 microsecond accuracy, and a National Instruments USB data acquisition hub, the plot of RPM uncertainty vs. RPM is as follows:

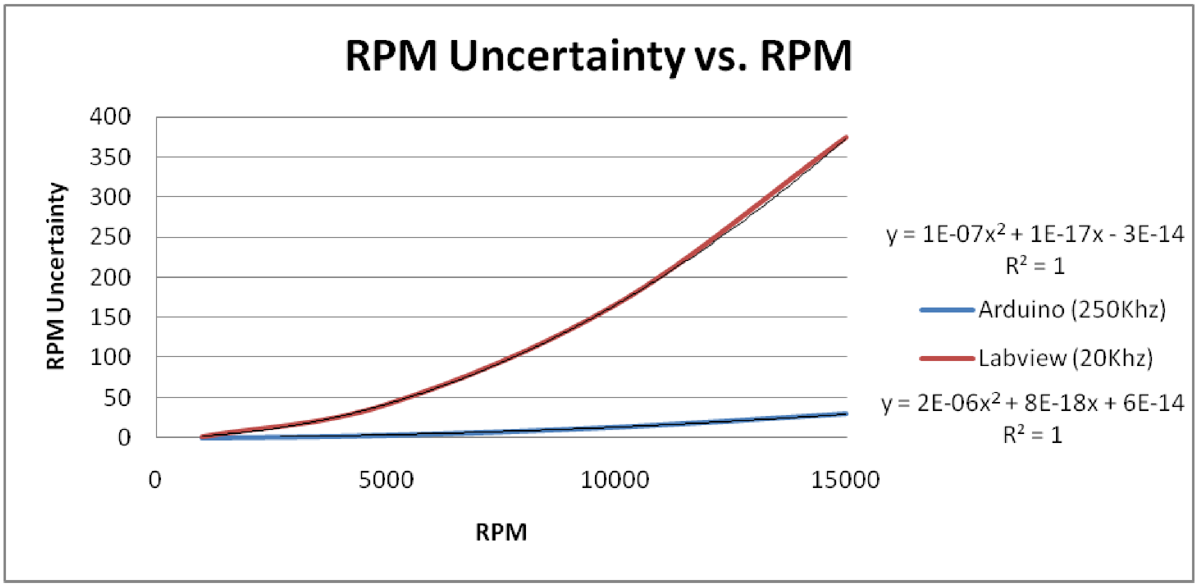

Figure 56 - RPM Uncertainty vs. RPM

If the RPM timestamps are taken every X number of revolutions instead of every revolution, then the uncertainty associated with this measurement is divided by X. Since it is not certain if Labview's imbedded frequency function returns the result of a single peak, or an average of many, it is not possible to depend on reduced uncertainty when using labview measurements.

The Arduino based RPM sensor can experience two trivial errors. The first being a misreading of RPM during the first 10 revolutions of engine re-start as a result of the long period of inactivity. The Arduino interprets the engine's idle state as simply a very long period revolution and averages it in as such. This measurement error is of no practical consequence. Also, the microsecond counter in the Arduino overflows approximately every 70 minutes, upon which that series of averaged RPM's will be incorrect as well.

In the later testing stages of the Dynamometer, the Arduino based RPM sensor developed trouble with false peaks tripping the peak detector, and incrementing the revolution count artificially. This was most likely due to back EMF through the power source of the Arduino, or interaction between the RPM optical sensor wire and other wires in the area. At that late stage of testing, the RPM sensing method was changed back to labview's continuous sensing method to ensure that each peak was counted. The increased single measurement uncertainty caused no worry since a typical data point's acquisition duration is governed by fuel flow uncertainty. This allows a vast excess of RPM data to be collected that can be used to statistically reduce uncertainty.

Horsepower

Horsepower is an indirect measurement consisting of RPM and torque, and thus its uncertainty varies with engine speed similarly to RPM. The formula used to determine Horsepower from these inputs is shown below:

$$Horsepower = \frac{Torque \cdot RPM}{5252}$$

Which results in the following uncertainty formulation:

$$Horsepower\ Uncertainty = \sqrt{\sigma_{Torque}^2 + \sigma_{RPM}^2}$$

That expanded equals:

$$Horsepower\ Uncertainty$$

$$= \sqrt{\left[\frac{\sigma_{loadcell\%} \cdot RO_{loadcell}}{Load}\right]^2 + \left[\frac{\sigma_{calibration\ mass}}{m_{calibration\ mass}}\right]^2 + \left[\frac{\sigma_{moment\ arm}}{L_{moment\ arm}}\right]^2 + \left[\frac{RPM^2}{Sample\ Rate\ \times 30}\right]^2}$$

Applied to present Dynamometer condition:

$$Horsepower\ Uncertainty = \sqrt{\left[\frac{0.025}{Load}\right]^2 + 3.7217E^{-7} + \left[\frac{RPM}{600000}\right]^2}$$

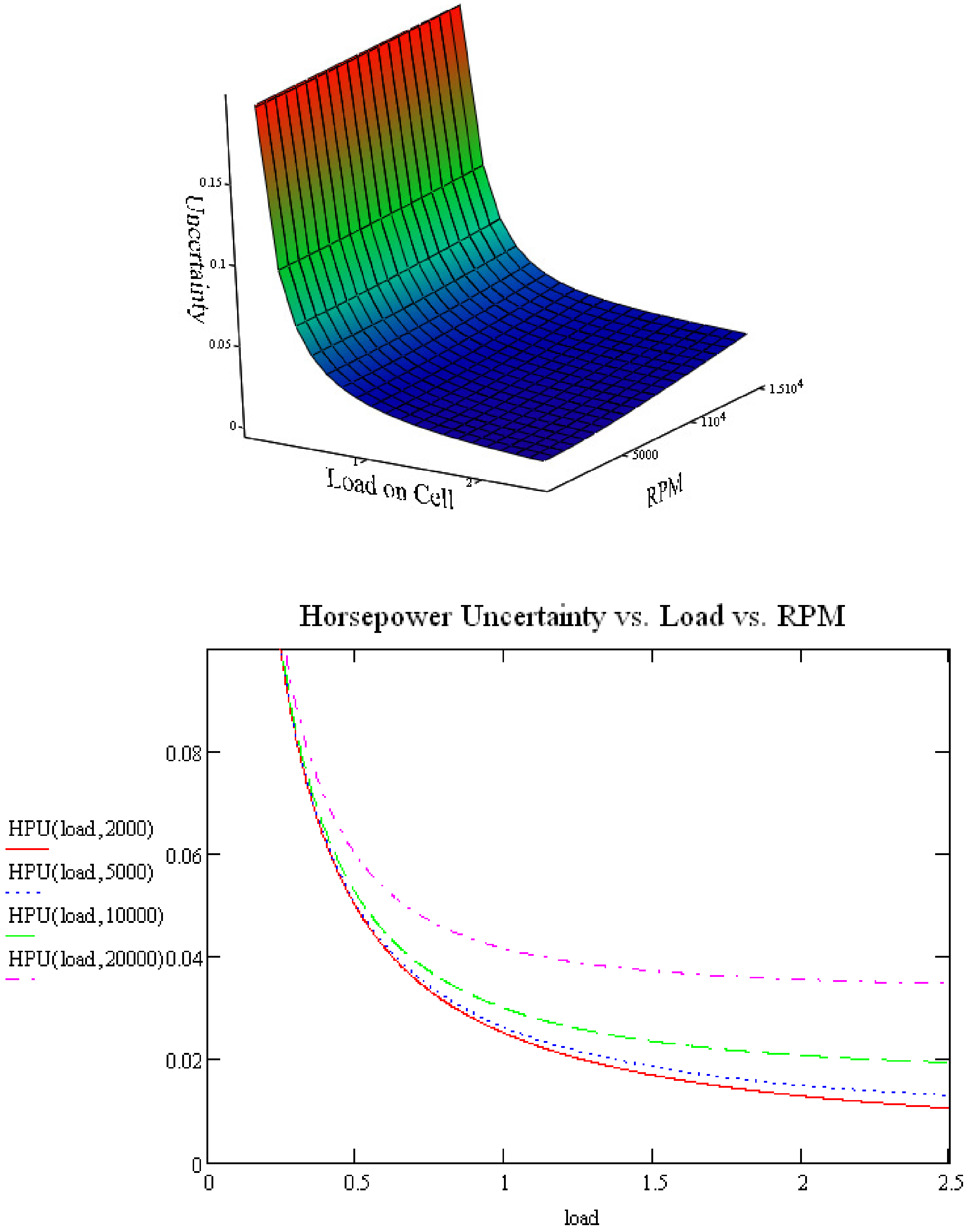

Figure 57 - Horsepower vs. Load vs. RPM Uncertainty

The two plots above are useful in selecting the proper load cell and data acquisition model for minimizing Horsepower uncertainty. Even in this case of relatively high engine RPM's, National Instrument's cheaper USB data acquisition module is able to provide reasonable uncertainty at the top end of the possible RPM band. The plots show that the load cell's uncertainty is much more important when testing for output horsepower. If one were to use a 5 lb load cell instead of the 2.5 lb. cell shown, the uncertainty would increase by a factor of two. The interaction between the load cell's millivolt level output signal and the analog to digital converter in the NIDAQ unit was intentionally left out of the uncertainty calculations as repeated calibrations have proven the digital to analog conversion to be a non factor. The data acquisition rate is fast enough, and resolution fine enough, that the uncertainty regarding the digitization of the load signal is negligible. For more background on why this uncertainty decreases with sample rate, please refer to the "Statistical reduction of Uncertainty" section.

Fuel flow rate

Fuel flow rate is a very important but difficult parameter to measure for small engines as a result of the extremely small fuel flow requirements of a properly tuned small engine. Fuel flow rates on the order of 0.008 grams per second to 0.3 grams per second can be seen during engine testing depending on the fuel used, and engine settings. As described previously in the operating theory section, fuel flow rate is determined by the least squares curve fit of fuel weight vs. time data. The scout pro 400 gram balance sends the scale reading approximately each 1/4 second with an uncertainty of 0.1 grams. since flow rate is the combination of two measured quantities in this situation, the uncertainty formula becomes:

$$Fuel\ Flow\ Uncertainty = \sqrt{\left[\frac{\sigma_{balance}}{\Delta W_{fuel}}\right]^2 + \left[\frac{\sigma_{time}}{T_{elapsed}}\right]^2}$$

For the present setup of the dynamometer, $\sigma_{balance} = 0.1\ g$ and $\sigma_{time} = 0.25\ s$. This results in the following relation.

$$Fuel\ Flow\ Uncertainty = \sqrt{\left[\frac{0.1\ (g)}{\Delta W_{fuel}}\right]^2 + \left[\frac{0.25\ (s)}{T_{elapsed}}\right]^2}$$

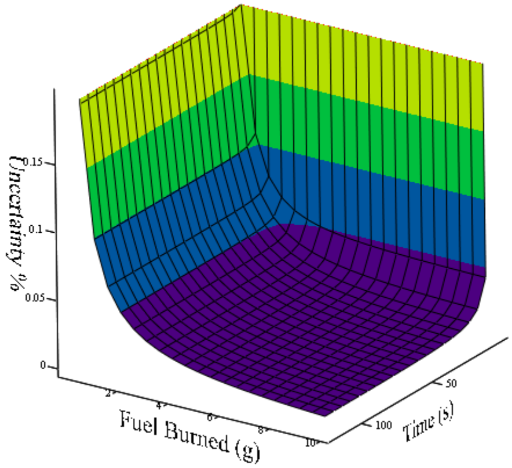

Fuel Flow Uncertainty vs. Time vs. Fuel Burned

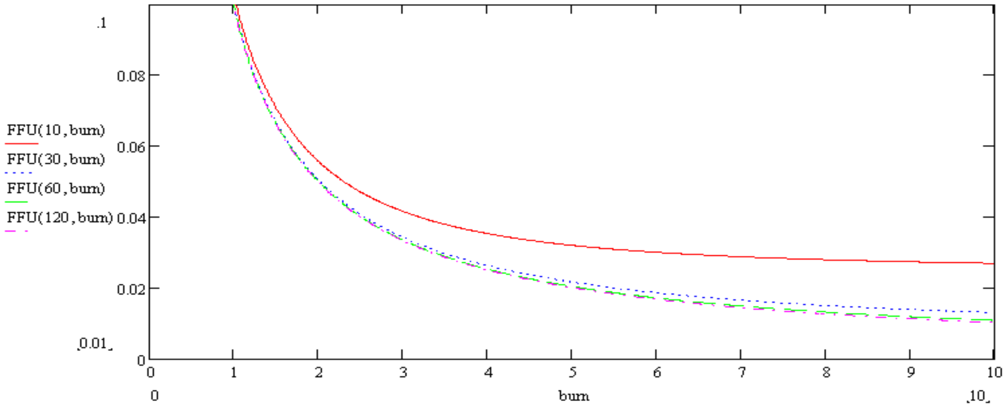

Figure 58 - Fuel Flow Uncertainty

The previous two plots are useful for gauging the relative importance of time and fuel mass measurements, but a plot more useful to a researched using the dynamometer is found below. This plot shows for various flow rates how long one has to wait for the fuel flow rate uncertainty to reach a desired level. Also in practice all of these estimates are found to be optimistic. The balance is unshielded in a windy outside environment, and some level of vibration still passes through the isolation mount, these factors compound to make the true fuel mass measurement uncertain to much greater than the rated 0.1 gram. Such errors are systematic and therefore unquantifiable.

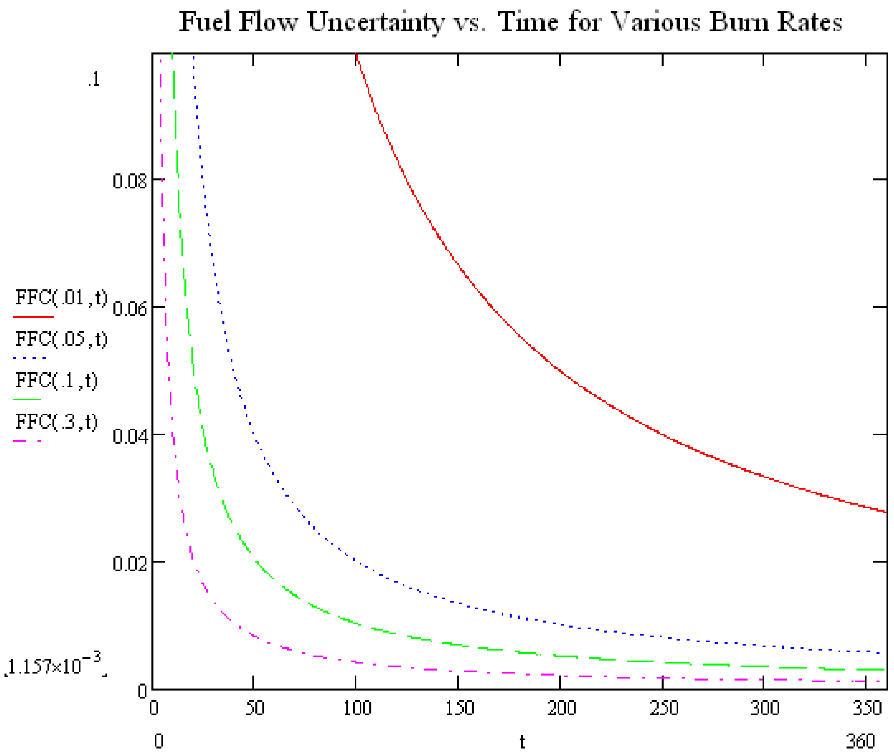

Figure 59 - Fuel Flow Uncertainty vs. Burn Rate vs. Time

As one can see, for large flow rates only a few seconds are required to converge a fuel flow rate measurement. This situation would arise with a glow engine running very rich on low percent nitro methane fuel. For the smallest flow rates the steady state time is measured in minutes, making the measurement of high efficiency engines a laborious task. These flow rates are found on engines running lean with full weight hydrocarbon fuels.

Energy Density Uncertainty

Being the combination of all previous measurements, energy density is easily the most uncertain, and for the purposes of this project, the most valuable output parameter. The previous data also allows the computation of brake specific horsepower (BSHP), which is again a measure of efficiency and energy density simply expressed in different units. The formula for computing energy density uncertainty is as follows:

$$Energy\ Density\ Uncertainty = \sqrt{\sigma_{HP}^2 + \sigma_{ff}^2}$$

A deceptively simple expression, that when expanded shows the care that must be taken to achieve acceptable uncertainty.

$$Energy\ Density\ Uncertainty$$
$$= \left\{ \left[\frac{\sigma_{loadcell\%} \cdot RO_{loadcell}}{Load}\right]^2 + \left[\frac{\sigma_{calibration\ mass}}{m_{calibration\ mass}}\right]^2 + \left[\frac{\sigma_{moment\ arm}}{L_{moment\ arm}}\right]^2 \right.$$
$$\left. + \left[\frac{RPM^2}{Sample\ Rate\ \times 30}\right]^2 + \left[\frac{\sigma_{balance}}{\Delta W_{fuel}}\right]^2 + \left[\frac{\sigma_{time}}{T_{elapsed}}\right]^2 \right\}^{\frac{1}{2}}$$

If one inserts the present settings of the dynamometer, and assumes the operator will gather data until fuel flow is converged to 5% uncertainty, the following plot emerges:

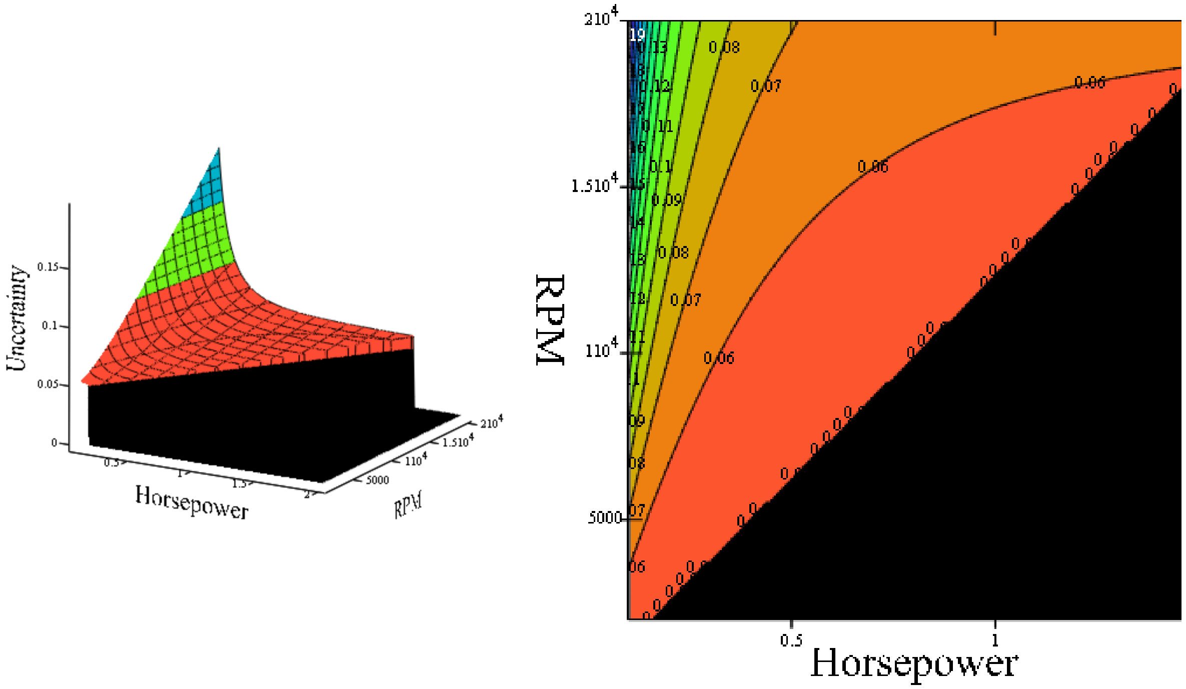

Figure 60 - Variation of Energy Density Uncertainty with RPM and Horsepower

The above plots show that when fuel flow converges to at least 5% uncertainty, one can achieve less than 10% energy density uncertainty for most any practical engine setting. The black regions of the plot represent conditions that would overload the load cell of the dynamometer. The dynamometer is poorly suited for low output high RPM engines due to the extremely low torque output of those engine types. Below The Contour Plots are repeated for 1% and 10% fuel flow uncertainty to guide any future user of the dynamometer. Just to note their relative scale, all three uncertainty plots use the same color contours.

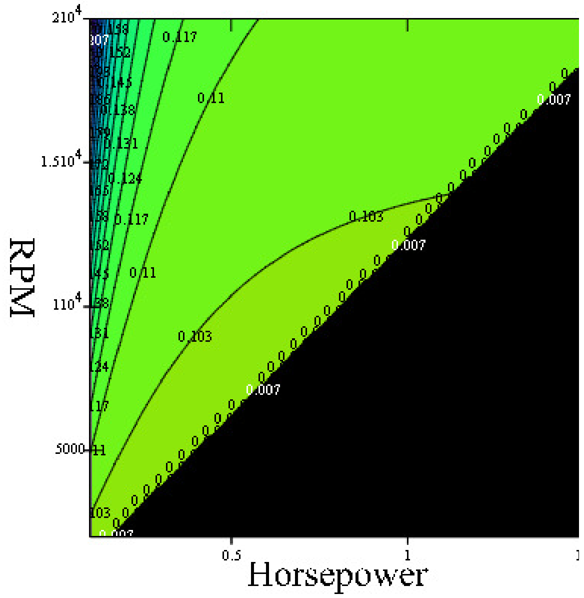

Figure 61 - Variation of Uncertainty with RPM and Horsepower - 1% Uncertainty

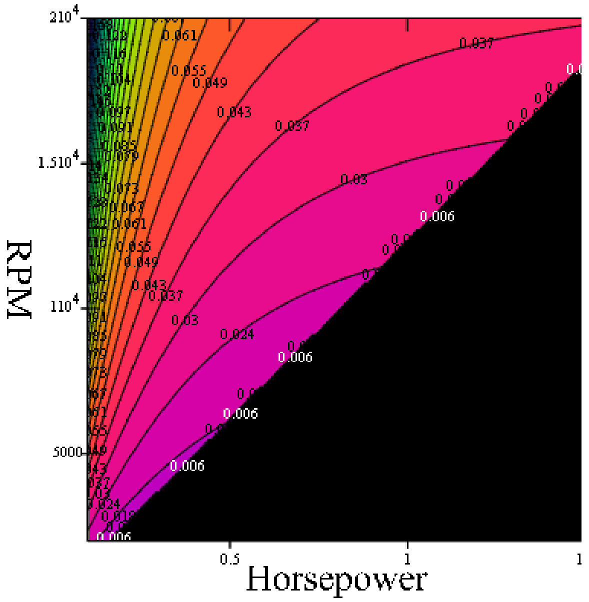

Figure 62 - Variation of Uncertainty with RPM and Horsepower - 10% Uncertainty

Statistical reduction of uncertainty

When one is only interested in the mean value of many data points as is the case with steady state dynamometer runs. One can statistically reduce the measurements random uncertainty by the square root of the number of samples taken. The averaging of the gathered points has no effect on systematic uncertainty, but can be used to compensate for analog or digital noise in the system. The following mathematical development shows how an increased number of samples reduces variance of the mean. (Pengra and Wesleyan)

$$\sigma_m = \sqrt{\frac{\sum_{i=1}^{N}(X_i - \bar{x})^2}{N(N-1)}} = \frac{s}{\sqrt{N}}$$

Where σ_m is the standard deviation of the mean value of measurements, N is the number of samples averaged, and s is the single sample standard deviation.

This technique is useful for stating lower random uncertainties for horsepower, torque, and rpm. In practice systematic error prevents the total error from reaching the low levels this theory may suggest. This technique is not useful in reducing the uncertainty of fuel flow measurements, since the curve fit over time is essentially a single measurement, and cannot be treated as N number of independent measurements.

Design Decisions

The seemingly simple task of measuring an engines output torque, RPM, and fuel consumption becomes very complicated when attempted on small engines. The torque's involved are very small while the operating speed is very high. The engines are far from being perfectly balanced which results in large vibration levels that vary with engine RPM. The fuel dispensing mechanisms on these small engines are functional at best, and do a poor job of maintaining a proper fuel to air mix. In addition, the optimal fuel flow is so small for full weight hydrocarbons that the fuel jet orifice size is nearly immeasurable.

Most large scale dynamometers measure torque on the load side of the machine, but the high speed and low relative output horsepower of small engines would make the losses associated with any coupling device a significant portion of the output of the engine. Such a torque loss would create an unquantifiable systematic error in the measurements of the engine. This dynamometer was designed with torque measurement on the mounting side of the engine to prevent such coupling losses. This complicated problems associated with vibration and torque measurement as the engine was no longer constrained in all six degrees.

It was also found that small engines are very dependent on the attached inertia to maintain a constant speed. There is not enough inertia in the engine crank shaft alone to maintain a sufficiently constant speed. For this reason, and for resisting off axis vibration, a flywheel was added to the output of the engine. Without the added inertia, the test engine was found to run very rough, and with increased vibration due to the unsteady cycle. The addition of inertia also allowed the engine to function at lower speeds due to the increased energy storage.

An electric motor brake was used mainly for the purposes of someday simulating a hybrid type system, where the electric motor load would be used as a generator to drive auxiliary systems. The use of an electric motor brake also allowed for easy engine starting at the flip of a switch where the motor was disconnected from the load bank, and connected to a 12 V power source. Tuning the resistance connected to the motor with the electromechanical properties of the motor itself to match the output power of the engine being tested is as essential part of making the dynamometer test controllable. Too much resistance, and the engine will overpower the motor. Too little, and the load becomes too sensitive which complicates RPM control. To control the load applied to the engine, a DC speed controller was used to change the duty cycle of the applied load.

National Instruments software package Lab view was used to acquire all data being generated from the dynamometer, This software along with NI's USB data acquisition module allowed a 48Khz total sample rate among all channels. The load cell and RPM sensor were directly connected to the analog to digital converter (DAC) and imported to the software at 20Khz on each channel. Fuel mass was brought into the computer through a serial port as the scale had the ability to communicate through RS232. Exhaust temperature, and any other temperature data could be connected to lab view, but is presently only being linearized, amplified, and output to a multi-meter in units of 1mv/deg F.

Coupling Devices

The coupling method between the engine and motor became one of the most important and troublesome design aspects of the dynamometer. Many off the shelf solutions were tried and failed to transfer torque at high rpm's without breaking down. Finally it was concluded that the root problem laid in the inherent dynamics of an axially mounted system and was only magnified by the small angular slop that inadequate machining tolerances had allowed in the dual bearing mount.

A common trait of all mounting techniques is that they are dependent on the stiffness of the mounting arm that is used. The mounting arm for most engines is a simple fork design, and as a result of being rotationally non-symmetric, exhibits angle dependent stiffness. This produces elliptical vibration paths as the couplers diverge. Two seperate materials were used to constrain the engine, CNC'd medium density fiberboard (MDF) and 6061 Aluminum. An approximate plot of stiffness as a function of theta can be seen below. This plot assumes the engine is mounted with a single pin on the left and right side so that the fork portion acts as a strain related double beam, and that all vibration forces are sufficiently away from the front bearing that they can be approximated as y and z shear loadings on the end of the shaft.

Figure 63 - Destroyed MDF Engine Mount

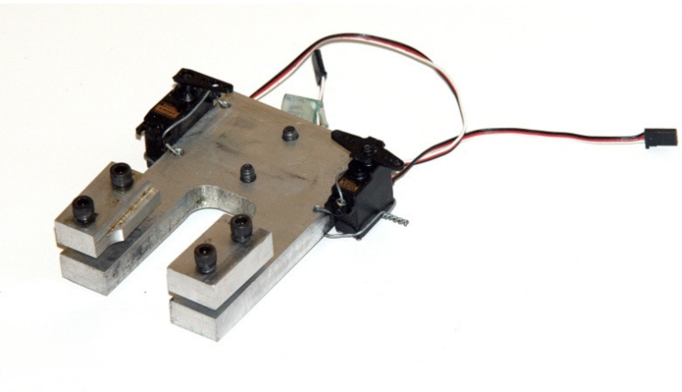

Figure 64 - Replacement Aluminum engine mount

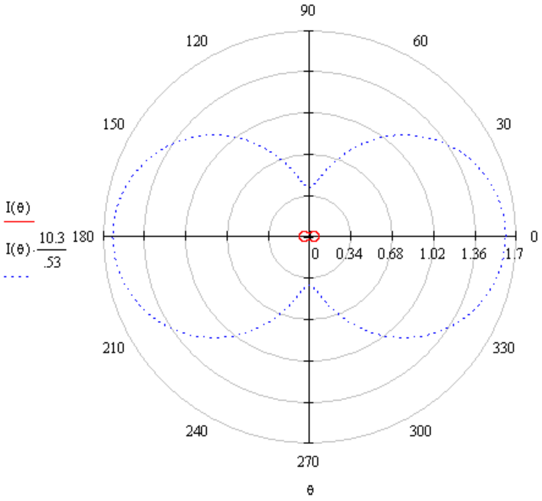

Figure 65 - Variation of Moment of Inertia with Theta

(Two Point Engine Mount)

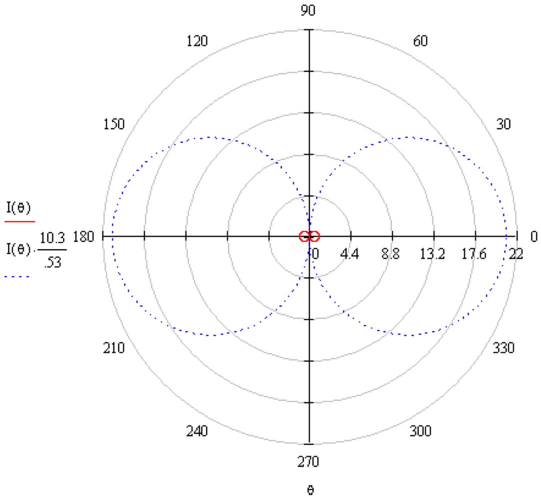

Figure 66 - Variation of Moment of Inertia with Theta

(Rigid Engine Mount)

One can see in the plot above how the relative stiffness of the engine fork varies with angular displacement and material type. The red path indicates the EI term associated with an MDF engine fork, while the blue path gives the EI term for aluminum.

The modulus ratio between the two materials is 19.4, making aluminum much better suited to reduceing vibration intensity. The stiffness of lateral deformation would be even more magnified if the engine was considered to be rigidly mounted to the fork as it is in application. In that case the lateral inertia would dramatically increase due to the AR^2 term as shown in the second plot.

Unconstrained spider coupler

The first coupler tried was an unconstrained square key coupling. The coupler used aluminum ends with built in self tightening bores, in combination with a polyaccetal insert. The coupler is classified as unconstrained because the keyway in each side of the insert was a pure rectangle that allowed the aluminum key to translate in the corresponding direction. At very low RPM's this coupling worked as designed, the insert allowed any misalignment between shafts to pass without issue, and the engine and motor functioned without problem. It is also important to note that at this stage of the dynamometer the flywheel and shield were not in place. once the engine passed a critical speed the engine side coupling came off center and from that point was forced outward. As there is no radial mechanical constraint built into this coupler, the engine began to vibrate at the frequency of rotation, and shortly destroyed both the polyaccetal insert and the MDF engine mounting board. The static stability equations for the unconstrained coupler are as follows:

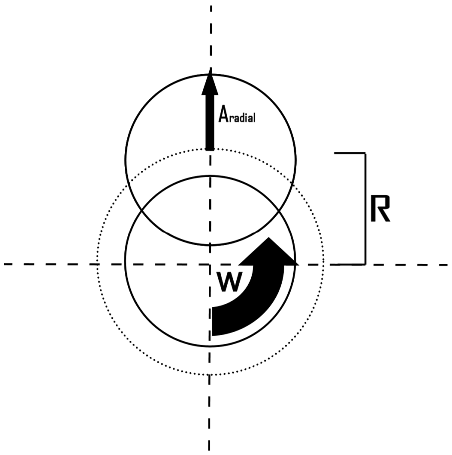

$$Acceleration = r\omega^2 - \frac{rk}{m}$$

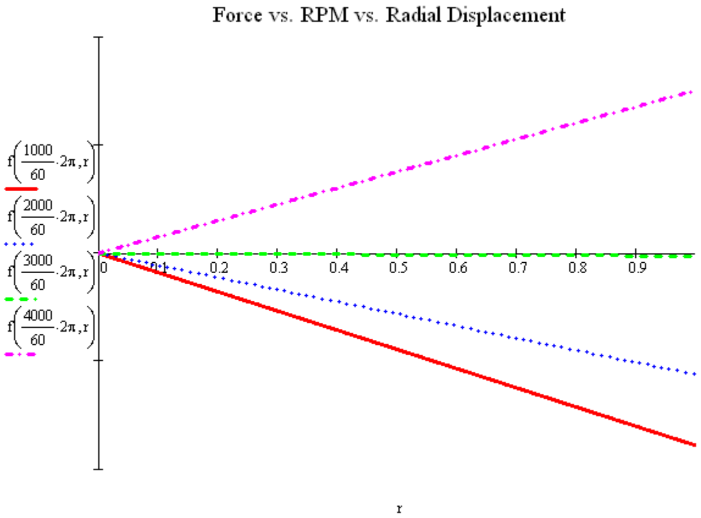

Figure 67 - Force vs. RPM vs. Radial Displacement of rotating unconstrained shaft.

The plots above share similar trends to aircraft static stability curves. Any negative sloping line indicates a stable converging system, with the slope of said line determining the magnitude with which the object is forced back to zero. The plots show that for increasing RPM and mass, one must have an increasingly stiff restraint to remain stable. The real dynamometer exhibited some slop in the main torque shaft support bearings. The engine output shaft is able to shift approximately one millimeter in each direction. That machining error can be approximated in the stability model as an offset spring. The shift of the spring's zero crossing point causes a vertical shift in the stability plot. This means that one can no longer eliminate shaft vibration completely by increasing stiffness, and that even stable systems' vibration will increase quickly with RPM.

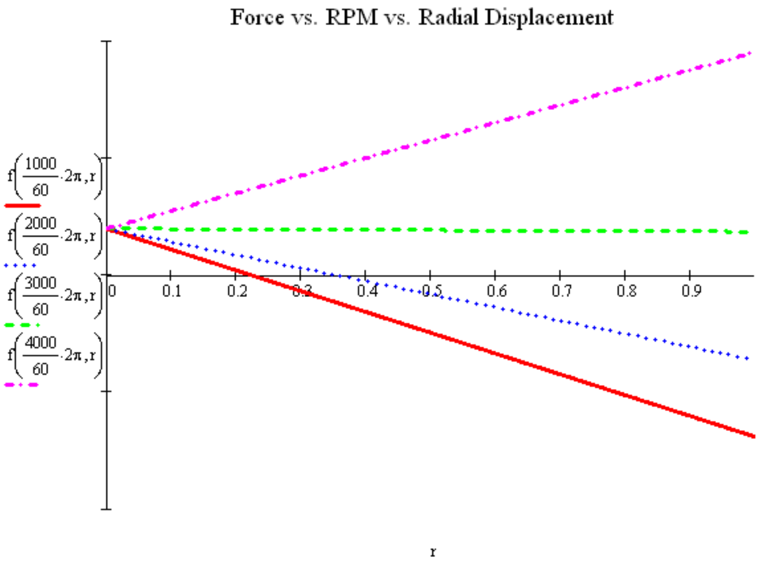

Figure 68 - Force vs. RPM vs. Radial Displacement for Offset Spring

The equation for computing the spring constant necessary to produce a neutrally stable system is shown below. Any stronger and the system will be stable at a given RPM, any less and the coupling will diverge.

$$K_{neutral} = m\omega^2$$

The unconstrained coupler did not allow the engine to function properly above its divergent speed, and often resulted in the destruction of the polyaccetal insert. Even after the joint was taped over with multiple wraps of electrical tape, the natural instability of the coupler still forced the system to diverge, although the tape did limit its magnitude.

Rigid mount

To constrain the engine shaft to always be co-axial with the motor shaft, a rigid coupler was purchased from MSC, and worked as intended. This coupler modified the dynamic system to behave as a doubly constrained shaft with the vibration of the engine being absorbed as a point load in the middle of the shaft. This method would have been final if the shaft of the engine did not come threaded from the manufacturer. The set screws were unable to tighten the collar enough to prevent it from slipping at different engine operating points. The collar had no issues with the smooth motor shaft, but would not stay attached to the threaded engine shaft. The set screws were tightened until one sheared off.

Rubber Grommet Mount

To add damping into the system, rubber washers were placed between the engine in hopes of modifying the frequency response curve to reduce the magnitude of vibration as the engine moved through the torque arms natural frequency. As neither the motor mount, or engine mounting system had no dissipation, the entire dynamometer was theorized to be acting as a series of high modulus springs responding to different frequencies based on the engine's RPM. Adding rubber damping would have the downside of absorbing a small amount of energy from the engine and adding systematic uncertainty to the measurement however small it may have been. The downside to using basic rubber washers, is that between glow fuel, naphtha, and gasoline, one of them will surely react and dissolve nearly any type of low modulus washer one could use. Additionally, the majority of broadband vibration was found to be a result of coupler misalignment, and natural engine vibration. While the mass damping arm does become excited in the vicinity of 80 Hz (5000 RPM), its region of excitation is so narrow that it poses no real consequences on dynamometer testing. Most rigid portions of the dynamometer (excepting the inertia arms), have natural frequencies much higher than that of any test point, while the floating torque arm portion of the dynamometer is coupled by such a low modulus spring that its natural frequency lies well below the operating range of the dynamometer. Extra inertia was added to the torque shaft to further lower its natural frequency, and attenuate the higher frequency portions of the engine's output.

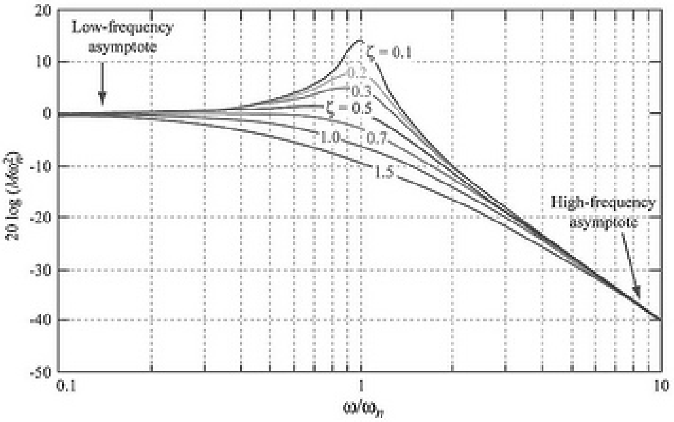

Figure 69 - Classical 2nd Order Frequency Magnitude Curve

Radially constrained spider coupler

Following the failure of the rigid mount to stay attached to the threaded shaft, a radially constrained spider coupler was attempted. This coupler behaves in a similar manner to an unconstrained spider coupler discussed previously, except that the teeth on this coupler's keys are designed to limit radial displacement. While the modified teeth did somewhat limit the radial movement of the engine, the governing equations had not been fundamentally changed. each polyaccetal insert allowed enough slop that the coupling system was inherently unstable. Two different durometer inserts were tried, and in each case the energy dissipated through vibration and friction melted, or otherwise caused the insert to fail. One could easily burn oneself on the coupler after even a short run of the dynamometer. In addition to the above problems, the coupler also utilized a set screw which required a 24 hour period for lock-tite to dry between engine swaps. This would greatly increase the time required to change engines on the dynamometer. If lock-tite was not used on the set screw in conjunction with a deep ground flat area, the screw would naturally back itself out and the coupler detach itself from the output shaft of the engine. Also, to remove the required lock-tite a high temperature MAPP gas blowtorch was required which is not very well suited for use around engines and dynamometers covered in oil residue.

Inertia Wheel

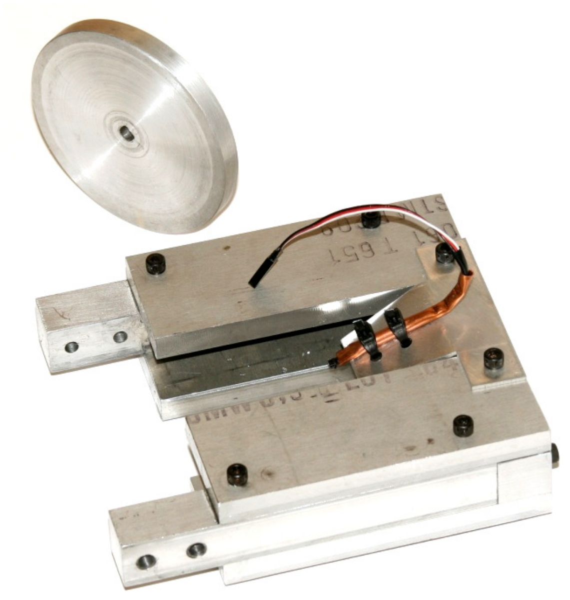

After even the radially constrained spider coupling, and the substitution of an aluminum mounting plate instead of wood failed to eliminate vibration an inertia wheel was added to attempt to change the dynamics of the system by adding some gyroscopic stability to the engine. While only the added mass of the inertia wheel would work for limiting the translational vibration of the engine, the rotational inertia of the wheel would contest any applied moments. Additionally the inertia wheel was added to replace the assumed propeller inertia, which was non-negligible at approximately . Although a 2.1 inch solid aluminum flywheel would provide an equivalent driven inertia, the flywheel was cut to 5.5 inches in diameter and 0.5 inches thick to maximize the available area between support rails. When the 5.5 inch diameter inertia wheel reaches 12,000 RPM it is storing an equivalent amount of energy to a 9 mm bullet (~350 ft-lb) and is certainly capable of similar damage. For this reason a solid aluminum containment shield was built around the flywheel to protect the dynamometer user from any danger.

In the worst case the flywheel would shear the engine shaft and then bounce harmlessly inside of the containment shield. The energy in that flywheel at full speed should always earn the respect of any user of this dynamometer.

One of the main benefits outside of gyroscopically balancing the engine was that the engine's cycle ran much smoother with the added energy storage. The difference was especially noticeable at low RPM, where the engine would not even function in the absence of the inertia wheel. The engine was much quieter as well, assumedly from the combustion process happening more consistently each revolution.

Locking spider coupler

When the inertia wheel was added to the output shaft of the engine, the normal locking spider coupler no longer fit onto the smooth portion of the engine output shaft, and the ground spot of the set screw was in the wrong location. Additionally, there was insufficient room on the output shaft to secure the flywheel and coupler separately, so both were machined into a single part. The engine output shaft uses standard 1/4-28 threads, so a 1.25 inch diameter custom threaded coupler was made to act as both the nut to tighten the flywheel, and the key to transfer torque to the motor. The threads were cut into the engine so that under load they would be tightened, but as the engine is started, the torque is reversed and quickly backs out the nut. To lock this coupler in place, two opposing holes were drilled in the part parallel to the axis of rotation, and threaded in the bottom to accept a 1/4 - 28 set screw. The coupling nut was then tightened onto the shaft, pressing firmly against the flywheel, and then the two set screws were tightened down even further to form a sufficient friction fit between the engine shaft threads, flywheel, and engine thrust bearing plate to hold all parts in place during starting and normal operation. This method of restraint was very reliable.

Alignment sleeve

After the addition of a flywheel, and custom machined restraint nut, the problem of RPM dependent vibration still persisted. Since the forces involved are heavily dependent on radius between shaft centers, a PVC collar was machined to restrict the relative displacement to manageable levels. Electrical tape had been tried, and often came loose, or expanded under the stress of the diverging coupler. The PVC collar functioned as expected by reducing, but not eliminating vibration. As the dynamometer was run with the PVC collar in place, the vibration passing through the PVC collar was strong enough to pulverize the plastic into a fine white powder which over time eroded the inner surface of the collar and made it less effective.

Pulley Coupling

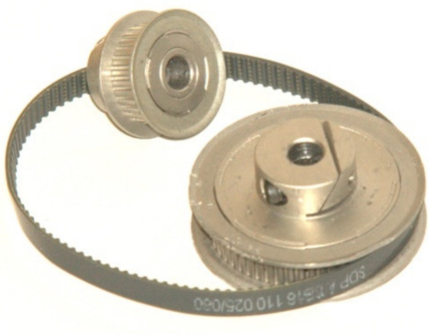

As the axial drive methods kept failing, no matter the method of restraint, the design of an off axis pulley drive was created. The motor mounting blocks were shortened, .080 MXL standard timing pulleys mounted to the motor and engine output shaft, and connected with a 109 tooth Kevlar reinforced belt. This off axis drive changed the dynamics of the system so that no matter the RPM, torque, or drive angle, the engines output shaft is always being forced in the same direction. While the pulley system does allow for some side to side movement, that is also the direction of the largest EI term in the bending equation. In addition the engine would be constrained to moving in a circular arc around the motor shaft. The motor mount was precision machined to eliminate the need for any tension controlling idler pulleys. The problem with using stock drive products' premade shaft locking pulleys is that it was not possible to simultaneously attach a flywheel and pulley. The smooth portion of the output shaft simply was not long enough. When an OS 40 four stroke engine with spark ignition was mounted to the dynamometer with only a pulley on its output shaft, the engine lacked the inertia to carry itself past the compression stroke smoothly, and could not sustain an even cycle no matter the ignition angle. Again, the addition of a flywheel would interfere with securing the pulley to the output shaft of the engine. The torque transfer thrust plate was re-machined to serve as both a flywheel, and front bearing. This allowed the pulley sufficient room to still attach itself to the output shaft of the engine. The flywheel and engine worked marvelously until the engine seized in a test and sheared the keyway out of the flywheel on the dotted line shown below. Changing the flywheel material to steel may have prevented this shearing from reoccurring, but would also pass the stress farther down the torque shaft, and possibly into the engine.

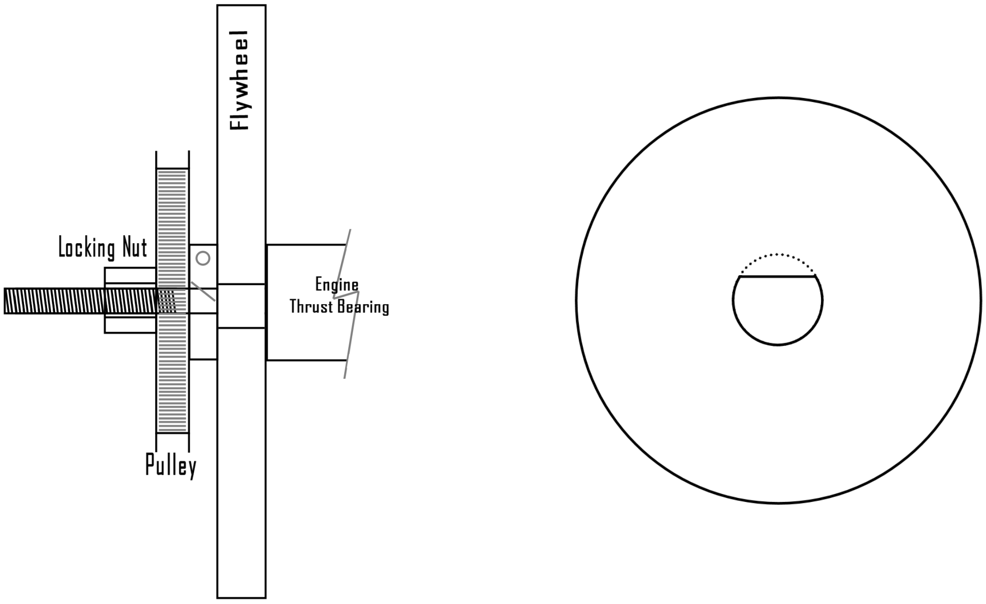

Figure 70 - Schematic of Flywheel and Pulley Mount

Locking Pulley

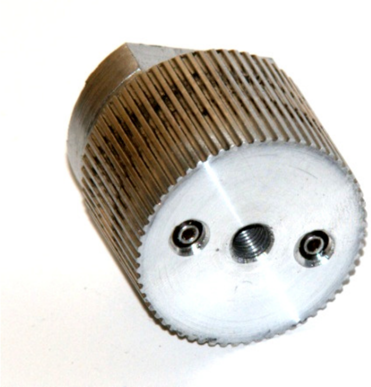

To simultaneously attach a flywheel, pulley, and engine thrust washer, a custom part was designed and machined to act as a lock nut, pulley, and flywheel restraint. The part was made in the same manner as the custom axial constrained spider mount with set screws tightening the threads against the engine output shaft to both ensure alignment, and prevent the lock nut from backing out as the engine was started. In this case some .080 MXL standard aluminum pulley stock was ordered from Stock Drive Products (www.sdp-si.com), so that the outer portion of the locking nut would become the drive pulley. This has become the final design as it combines the natural stability of an off axis pulley drive with the smoothing effects of an inertia wheel. The pulley is also small enough to use the same flywheel shield which reduced the time involved in making the modifications. This setup has endured over 5 hours of testing through all RPM ranges and power outputs without even replacing a belt.

Torque Shaft

The 2 inch diameter of the torque shaft was selected to provide sufficient stiffness without requiring special bearings to hold it in place. The Shaft's outer surface acts as the inner ball race of the needle bearings, and as such was machined to a tolerance of +0 -5 thousandths of an inch. Some slop does exist in the bearings, but was necessary to be able to slide the bearings onto the shaft during installation. The flat section machined on the front of the torque shaft is also machined to be perfectly in line with the center of the torque shaft. This allows the top surface of whatever is mated to the torque shaft to contain the axis of rotation thus minimizing systematic test error. The shaft is doubly supported to eliminate any chance of bearings binding due to torque. Between those two supports, two threaded rods were inserted into the shaft. One rod is used as a moment arm to apply force to the torque measurement load cell. The other larger all thread rod serves to increase the inertia of the rotating portion of the dynamometer. Steel washers can be added to, or taken from the inertia arm to change its resonant frequency. Presently, the torque arm resonates between approximately 4800 and 5500 RPM. The number and/or position of washers can be changed depending on desired results. The torque arm also serves as the device for applying calibration torques.

Needle Bearings

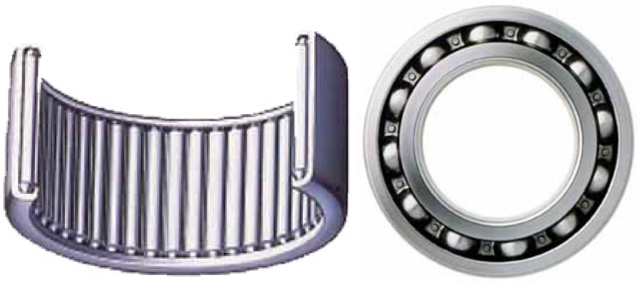

Needle bearings were selected to hold the torque shaft because of their low rolling resistance, and large contact area. This bearing type was not the best choice, as the lack of an inner race resulted in an imperfectly constrained torque shaft. Using a more traditional low friction spherical ball bearing would have eliminated most of the slop in the torque shaft, and is suggested as a future improvement to the dynamometer as it stands. The presence of bearing slop introduces the possibility of a frequency dependent excitation torque. If the bearings are excited at certain engine RPM's it could cause the torque shaft to bind, or generate a false torque. Spherical bearings would also sufficiently constrain the axial motion of the torque shaft. Presently the needle bearings let the shaft translate, and additional restraint is required. Eliminating the need for translational constraints will further decrease the chance of systematic error in measurements.

Axial Restraint

The original design of the dynamometer called for an axial engine to motor coupling that would inherently constrain the engine in the positive and negative directions. The failure of the prototype coupler led to the use of a non constrained spider coupler that allowed the engine to back away from the motor as it ran. To prevent the shaft from moving, a point was machined in the rear center of the shaft to reduce contact area, and an aluminum stop was screwed to the back bearing support. The back support was designed to be easily removable to enable quick engine swaps without the need to detach the motor.

Once axial coupling methods were abandoned in exchange for pulleys, the torque shaft was no longer constrained in either direction. A simple pipe clamp is presently being used to prevent the torque shaft from moving forward, and the flywheel crashing into its containment walls. Both restraints add systematic error to the torque measurement, and should be eliminated once the needle bearings are replaced with ball bearings. Thankfully during operation, the natural vibration of the engine all but ensures that the pipe clamp and point contact do not bind the rotating system by ensuring the contact is only intermittent.

Motor Brake Selection

While the theory of operation and difficulty in designing the electric generator based braking system have already been explained in the theory section, the selection of such a system over other braking methods has not been discussed. Any method of controllable energy dissipation can be used as a load control method for a dynamometer. Common methods include water brakes, eddy current brakes, friction loads, and electrical generators.

Water brakes use the engine to drive a water pump, the higher pressure head the pump is required to generate, the higher the torque load on the engine. This type of dissipation has the distinct benefit of extracting heat through the output shaft of the engine and transferring it to the water. The method is not very well suited for small scale engine dynamometers as finding a small pump compatible with the high rotational speeds, and vibration of small engines would be difficult. Additionally, having water plumbing in close proximity to sensitive electrical equipment would be unwise.

Eddy current brakes use electromagnetic induction to temporarily induce a charge in a piece of non-ferrous metal attached to the output shaft of the engine. This induced eddy current automatically opposes the applied field and can be easily controlled through pulse width modulation or other current control techniques. While either permanent or electromagnets can generate eddy currents, most commercial eddy current brakes use electromagnets so that the load can be controlled electronically instead of mechanically by moving a permanent magnet nearer to or farther from the rotating disk. The largest advantage of eddy current brakes is that they can be used to almost completely eliminate vibration transfer through the coupler, as that coupler consists of only electromagnetic fields. However, the brakes inability to absorb large torque's at low RPM's, variable torque with temperature, and the overall addition of heat energy to the system by inductively heating the aluminum flywheel, make this type of brake a suitable, but not preferable fit for small engines.

Figure 71 - Land and Sea Eddy Current Brake

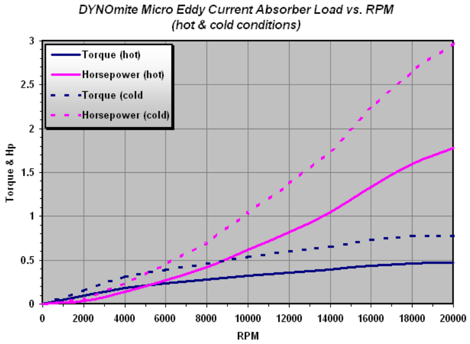

Figure 72 - Torque and Horsepower profile of Land and Sea Eddy Current Brake

The most basic style of dynamometer brake is a pure friction load. This style of load simply uses a variable tension belt around the rotating output shaft of the engine to dissipate the engine's power as heat. This style of load is difficult to control as the tension of the belt can change as the material heats up, or simply naturally wears down. Additionally the highly concentrated dissipation area will result in very high temperatures that would not only reduce heat flow out of the engine, but could also generate enough heat that the belt itself catches fire.

Finally, a generating type brake has the benefits of low speed torque, transfer of energy away from the engine, the ability to self start, and additionally generate useful power from the engine. Most of all for the application of powering a small aircraft, it allows hybrid power takeoff control systems to be tested without modification of the dynamometer. As a downside, the direct shaft coupling has proven problematic, rectification and conditioning of generated power is not a simple task, and the overall configuration of the motor and resistor bank requires more sophisticated configuration than an eddy, or water brake where one can simply turn up the power until the desired load is met. It is mainly for the reasons of low speed torque capability, self starting, and facilitation of hybrid power studies that this dynamometer uses an electric motor brake.

RPM control loop using Lab View

Simultaneously adjusting the applied load and throttle of a small engine to maintain a certain RPM while conducting a dynamometer tests can be a sensitive and complicated task if done by hand. The operator is also simultaneously listening for indications of cycle breakdown, making sure the fuel Burette does not run dry, and checking the dynamic calibration of the load cell. Lab view was used to sense the RPM and torque output of the motor, as well as control the throttle servo position. Because of the large processor overhead involved with lab view importing load cell data, optical RPM sensor data, fuel weight data, etc... the minimum stable cycle time for each calculation was 0.25 seconds. In each one of those periods the program operates on 2,500 data points from the attached analog sensors, and approximately one data point from the fuel scale. Attempts were made to modify the program, but the underlying issue appears to be with the time involved in accessing and processing the various blocks used in the dynamometer VI. In addition the RPM accuracy of lab view is limited by the method of sensing. The optical RPM sensor returns a high voltage each time the propeller breaks the light beam. This voltage is acquired at 10Khz and then reduced to an RPM every 0.25 seconds. Because of the limited data acquisition rate, the RPM resolution is approximately 150 revolutions per minute.

The inherent digital delay, poor RPM resolution, and natural cycle dynamics of the engine prevented a simple proportional controller from maintaining RPM. In fact all attempts to employ a proportional controller resulted in the engine immediately shutting off. The RPM hold function in lab view initially used throttle position as the output to the system. For low gains at which the system did not go unstable, the steady state offset from the target point was many thousand RPM, and that was if the engine remained running at all. Many times the throttle completely closed as soon as the proportional controller was turned on. To reduce this steady state offset, the gain was gradually increased until the engine became unstable. Because of the large 0.25 second delay associated with the lab view loop, the throttle servo could not respond to changes in engine RPM fast enough. For all cases the proportional controller failed to meet even the most basic performance requirement of at least keeping the engine running.

As a result of the complete failure of a simple proportional controller, a pure integrator was applied in hopes that its response time could be calibrated to yield a stable system that would also track the desired RPM on command. Since the engine stays running without being perturbed, it was desired to make the integral controller modify the natural state of the system as slowly as possible. This meant starting at very low gains and working up until the digital delay of lab view forced the system unstable. The first attempt at pure integral control killed the engine immediately. The extremely low gains applied did not integrate the error fast enough to keep the throttle servo from closing immediately as the engine was switched from manual mode to "self aware". A central value for the throttle to perturbate around was set and the integral controller was able to control the RPM of the engine, albeit with extremely large overshoot and settling times.

To combat these poor performance parameters, a proportional gain was added to the integral controller to modify the throttle servo when it was significantly off target. This PI controller exhibited improved overshoot characteristics and decreased settling times while regulating the engine to the desired RPM. Derivative control was eliminated from consideration as the noise inherent to the RPM signal would decrease the system's performance and would have forced it unstable with a high enough gain.

At the end of controller design and testing, the PI controller was able to maintain RPM as the load was varied on the engine. The final change came during tests that involved holding RPM constant while sweeping various load conditions. It was found that extremely small variations in load produced large variations in throttle position. It was difficult to manually vary the load in small enough increments to deliver more than three data points for any given RPM. To combat this sensitivity, the output of the RPM hold controller was switched to the load side, and the engines throttle was set to a constant position. This better emulated the actual scenario the experiment was trying to evaluate. Holding RPM constant, and varying throttle to see how the power output and engine efficiency changes as a result.

Overall the PI RPM hold controller significantly reduced dynamometer operator stress, and allowed more focus to be applied to the data being gathered, instead of the operation of the measurement device.

System Identification

The dynamometer was in a constant state of change as the Lab view controller was implemented, so any attempt at system ID at that time would have quickly become outdated. In addition the control speed and RPM sample rate through Lab view was much too slow to deliver even a moderately smooth sine wave input to the servo for testing the device properly.

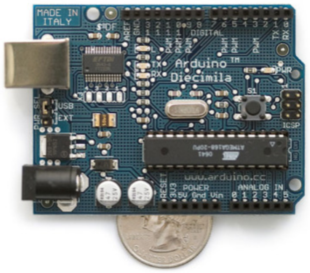

To expedite the update rate on the servo and RPM sensing, the controller and associated routines were programmed in to an Arduino Diecimila. The Arduino has a clock speed of only 16Mhz, which is over 100 times slower than the desktop computer that was running the control loop previously. The main speed advantage of the Arduino is a result of code efficiency. While the computer must carry out its own background operations, the Arduino can assign every clock cycle to a single task without being interrupted.

To keep the delay times in the control loop short, it was planned to have the RPM sensing task performed by one Arduino, and the controlling task on a second. The RPM Arduino was capable of determining the time required for 10 pulses accurate to 4 microseconds, which results in an RPM uncertainty of +- 10. The update Rate of the RPM state varied with engine speed because the algorithm output the state every 10 pulses instead of a fixed time increment. This way the uncertainty of the measurement could be insured, and the update rate would automatically accelerate as the engine reached higher RPM's.

To identify the system, a second Arduino was programmed to control a servo in a sinusoidal pattern while allowing for control of its magnitude and center frequency. This microcontroller was wired to a button that when pressed incremented the frequency of the sin wave from a minimum period of 30 seconds, to the maximum output update rate of the Arduino.

Also, a Lab view VI was made to accept data from the serial port (RPM Arduino output) and record it to file as fast as possible. Since this program was very simple and involved only writing data to a file, the update rate was exceptionally fast.

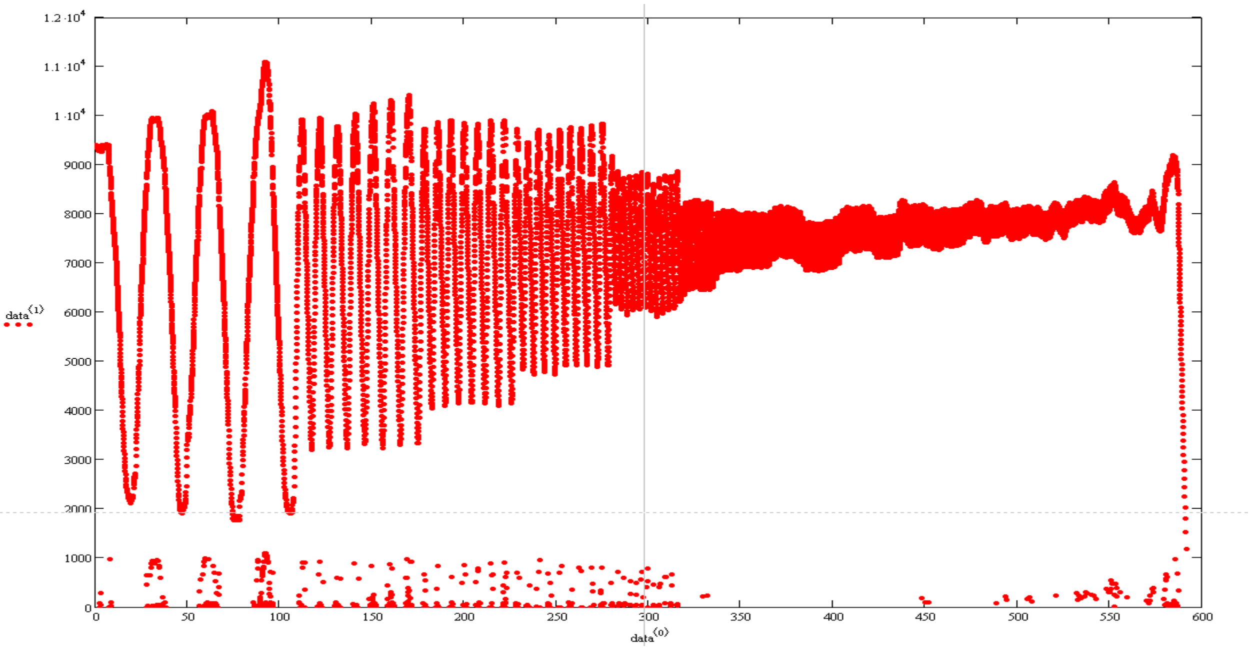

Figure 73 - System Identification Test Frequency Based Attenuation

With the sine wave properly calibrated, the engine was started and then controlled in a variable frequency sine wave pattern that was recorded by Lab view. The resulting data is shown below. It was not necessary to record the input frequency to the system as the input frequency passes through the system unchanged and is shown in the RPM data output. Each distinguishable frequency segment was filtered for average amplitude and frequency, then plotted in proper Bode form.

The resulting Bode magnitude plot shows the system is 1st order with a single pole at 0.11.

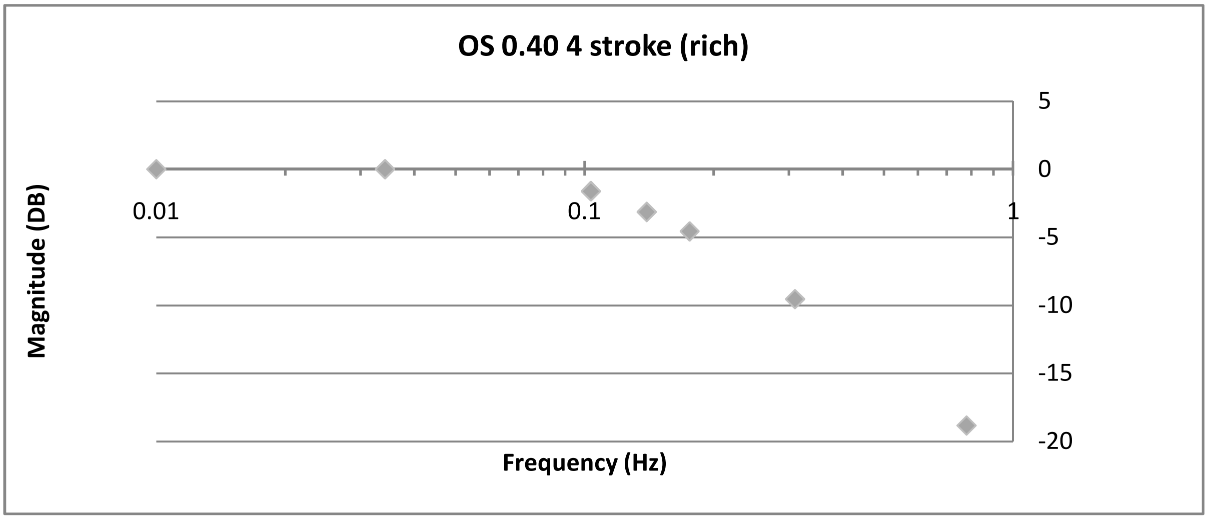

Figure 74 - OS 40 4 Stroke Bode Magnitude Plot

Controller Design

Since the system is only 1st order and has one naturally stable pole, in an ideal world one could simply apply a large proportional gain and get a very rapidly converging and highly damped response. However, the digital control delays in the system add a pure delay that quickly drives the system unstable at higher gain values. A simple PID controller was chosen because it is very commonly applied in machinery control applications, has the advantages of simple proportional control while using an integrator to remove steady state error, and a derivative term to add artificial damping. With one Arduino sensing RPM and the other solely dedicated to controller math and servo control, the update rate of the system would be at a minimum 12 times per second. This should have been high enough to determine an accurate derivative value that is sufficiently free of noise, and allow for a reasonable proportional gain before the system went unstable as a result of delay.

The assumption that made all this possible is that the RPM output of one Arduino could be quickly and easily transferred over a serial connection to the other Arduino. As with most assumptions, this one quickly broke down as the author learned there was not a readily available serial routine for accepting data larger than one byte between Arduinos. This meant that the 4 (or 5) digit RPM value must be split into its constituent bytes, then transmitted as a character, received by the 2nd Arduino, sorted into an array, then converted back into an integer data type. After that method was implemented, it was apparent that nearly all of the processing time was being used to parse the incoming serial data, allowing little extra processing time on the chip to calculate the outputs of a control system, much less update a servo every 20ms.

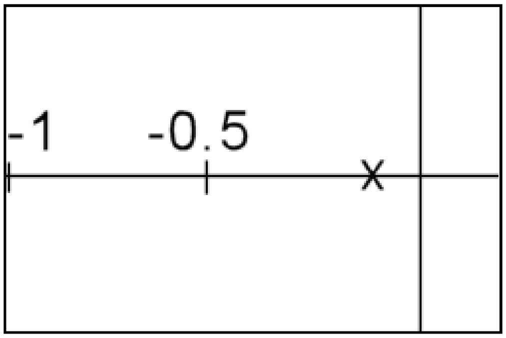

Figure 75 - Current Root Locus Representation

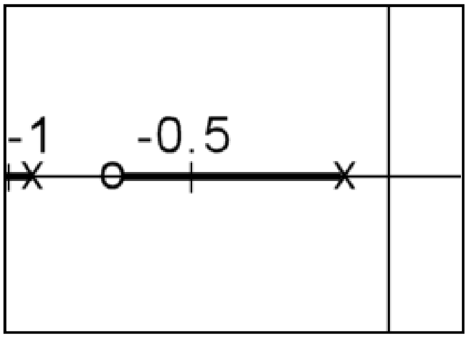

Figure 76 - Proposed Controller

It was decided to simplify the programming by including the controller on the RPM sensing Arduino. This would significantly slow down the rate at which RPM data was gathered, but without an operational serial connection there was no way to offload the controller processing time. The target RPM was determined by reading an analog input connected to a potentiometer, and the servo control outputs were set so that the engine throttle moved between 0% and 100% without stalling the servomotor.

The system update rate was fast enough that the proportional only controller worked, but with a 4,000 rpm steady state offset (commanded 11,500 RPM). The engine speed using that controller varied some 2,000 rpm around the set point, as the controller could not keep up with the necessary update rate. Lowering the proportional gain and adding integral gain was attempted, but resulted in even worse performance from the control system. The Arduino was simply not fast enough to catch every passing pulse from the RPM sensor, turn those into an actual RPM value, read the desired RPM from the analog input, calculate the error, integrate the error, determine the derivative of the error, apply all appropriate gains, change the output of the PID controller into a servo signal, and update the servo every 20 ms. The controller operations needed to be offloaded, but because of the previous failure in establishing serial variable transfer between two Arduino's, this was not possible. In addition, the rough control of the engine caused the engine to seize, which in turn sheared the keyway machined into the flywheel off and let the flywheel spin freely around the shaft of the engine. This significantly changed the dynamics of the system, and ended testing until the dynamometer could be fixed.

Proposed Controller Revisions

Since the system is stable to begin with, an Arduino based low rate controller with digitally established maximum slew rates will be created. This will not be executed in a time based simulation of classical analog methods. This will significantly reduce overhead on the microcontroller, reduce the importance of rapid RPM measurement, and most importantly will gently control the engine by guaranteeing the servo moves in smooth and slow increments as a result of the prescribed maximum slew rate. The Classical control analogue to this proposed algorithm would be an extremely damped integrator (PI). The damping is a result of maximum servo step change between iterations instead of a gain applied to a noisy derivative value. The integration is the result of the step change being constantly summed through time. This will deliver a stable system, but could not be called a traditional PID controller.

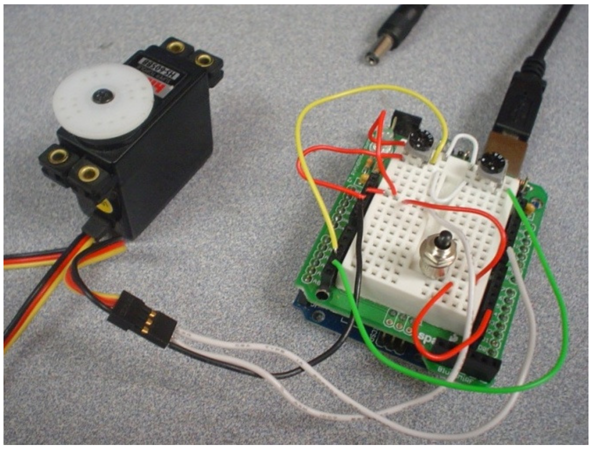

Figure 77 - Arduino Configured to Drive Servo

Creating digital control systems with output sensing rates fast enough to deliver accurate states requires more processing power than a simple microcontroller can provide in addition to its sensing and output responsibilities. The lab view controller successfully demonstrated low gain PI control, but completely failed at any proportional only control attempts. The Arduino based controller was just fast enough to demonstrate low gain proportional control, but failed to deliver smooth engine operation before the flywheel's keyway sheared and ended testing. The Arduino is theoretically capable of the same low rate PI control as lab view since its update rate is higher. But neither system is fast or robust enough to be worth its added operational overhead during testing. A simplified digital control as described in the previous section will be attempted, and should have a decent chance of success given that most of the simulation overhead, and possibility of widely varying servo outputs has been eliminated.

Engine Mount

The engine mount was designed to allow for quick engine changes, while simultaneously holding the engine rigidly, and on axis with the torque shaft. Two clamps on either side of the mount allow for OS engine's with similar crankcase sizes to the OS 40 FS, and OS 46 FX, to be mounted without modification. If the crankcase of the engine is larger or smaller, a new engine mount can be quickly made by simply following the bolt hole pattern found in the drawings appendix. A complete engine swap, including fresh calibration, and installation of an ignition system can be completed in less than 45 minutes. Initially the engine mount was made of MDF, but after vibrations literally shook that part to pieces, it was re-machined out of aluminum.

Load Cell Protection

While a low capacity load cell is necessary to accurately measure torque, it is not well suited for absorbing abnormalities in the engine's operation. Even a single engine seizure, or accidentally leaning against the torque arm could destroy the load cell. To prevent this, the deflection of the load cell was magnified with a lightweight spring who's natural frequency was well out of the operating range of the engine. The spring effectively reduced the average stiffness of the load cell/spring system. A hole was machined in the top panel of the dynamometer so that the spring could expand completely, and compress just enough to reach 2.2 lbs until the moment arm impacted the dynamometer frame which then absorbed the rest of the torque.

This method should have protected the load cell in all conditions, but during the maximum speed test of an OS 40 FS engine, the load cell was overloaded and irreversibly damaged. The spring had shown some variance in its stiffness during different calibration runs, and in this case must have transferred too much force into the cell. Instead of placing an identical load cell back in the same circumstance, a Futek load limited cell is now being used that has built in deflection limitation. This should ensure the safety of the load cell, as the stiffness of a cheap external spring is no longer an issue.

Fuel to Air Ratio controller

After preliminary testing showed a very strong relation between energy density and fuel to air ratio, the importance of monitoring fuel flow became apparent. Car type fuel to air ratio sensors were investigated as an option for measuring fuel to air ratio, but would have been rendered useless by the large oil discharge in the exhaust of small engines. Data could be gathered while running the engine on pure gasoline, but the engine would rapidly overheat, as small engines do not contain an oil reservoir.

Preliminary testing of the OS 40 engine with a propeller load showed the dynamometer to be very repeatable in horsepower and torque, but quite scattered in energy density. This was not due to the lack of accuracy in measuring energy density, all points were converged to approximately 10% uncertainty in fuel flow. The variance is a result of the engine's ability to run on a wide variety of fuel to air ratio's, and the resulting effect that has on energy density. The plots obtained during that testing cycle are shown below. Note the different HP vs. RPM curves of the two propellers used, and the wide variance of energy density.

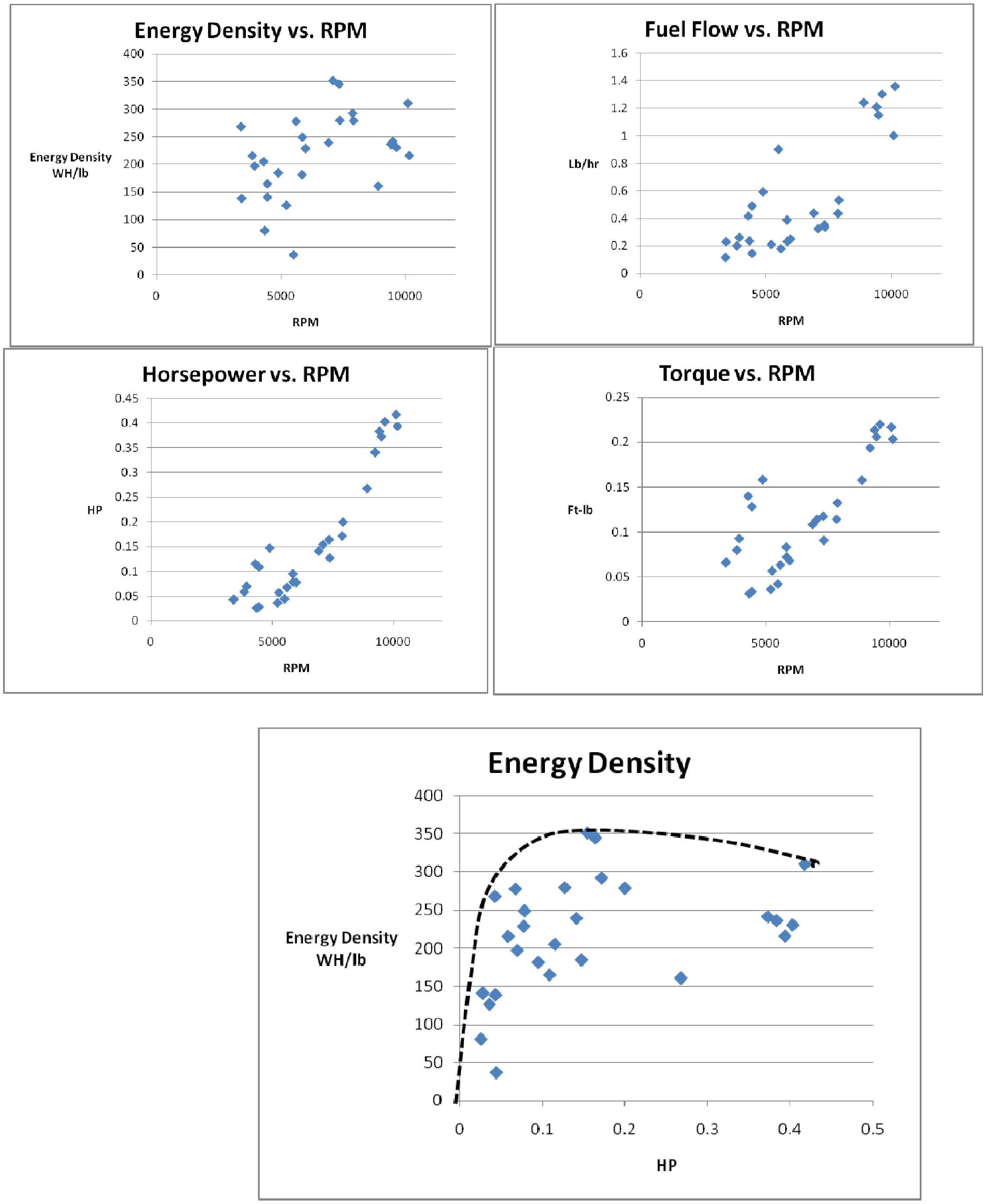

Figure 78 - OS 40 Propeller Load Testing

The mass based measurement system on the dynamometer is capable of providing very accurate fuel flow measurements, but has an update rate measured in minutes. To enable engine's to be run at the same point time and time again, two rotameters were added to cover the range of all possible flow rates for glow fuel, naphtha, and gasoline. While the rotameters do not have electrical output, they do enable the user to re-create a previously run test by establishing the same throttle, rpm, and fuel flow rate. The calibration tables for both rotameters flowing Naphtha and glow fuel can be found in the appendix of this document.

Additionally, it was attempted to track the optimal fuel to air ratio by tracking the peak exhaust temperature as mixture was changed at a given RPM, throttle setting, and varying load. The response of the thermocouple, as well as the natural drift of exhaust temperature made it apparent that a microcontroller would have difficulty successfully controlling fuel to air ratio with such incomplete and delayed information. It was instead decided to rely fully on repeatability of fuel flow to be re done. If an air flow meter of any kind is added to the dynamometer at a later date, the actual fuel to air ratio can be determined, but without a true air flow measurement, any approximation based on piston swept volume would be a pure guess, as one of the main differences between small and large engines is their scavenging efficiency. Additionally, the engines were unable to run lean enough on pure fuels to locate the peak exhaust temperature on an exhaust temperature vs. fuel flow plot. The typical profile for an OS 40 four stroke running Coleman fuel with an ignition system is shown below:

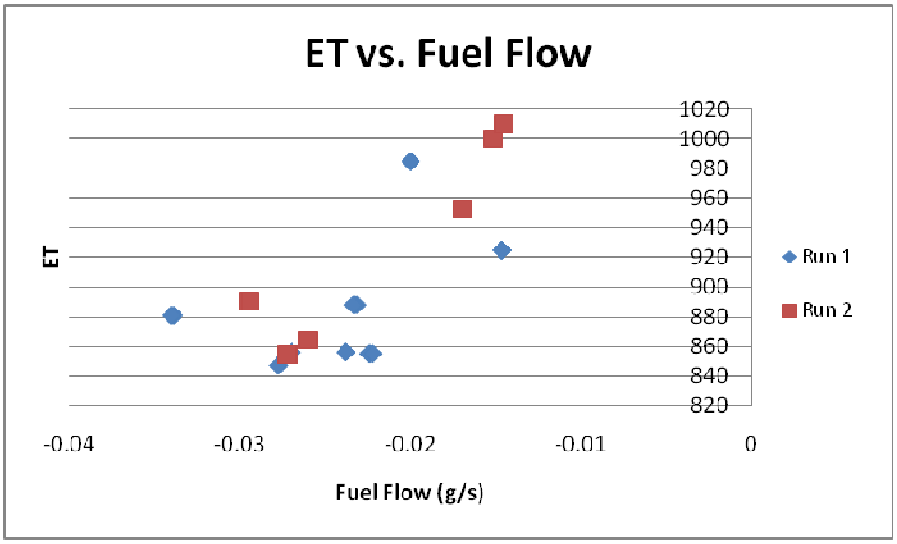

Figure 79 - Exhaust Temperature vs. Fuel Flow

Mechanical Attenuation

When the frequency dependent bearing vibration induced torque problem was discovered in later stages of testing, one of the proposed reasons for the change in output torque was the mechanical attenuation of engine torque into the support shaft of the dynamometer. It was theorized that the relatively large inertia of the torque shaft in combination with the dynamics of the spring connecting the moment arm to the load cell was attenuating the output of the engine, and adding large systematic error to the measurement. This type of attenuation would have been a problem if the dynamometer was seeking to measure the absolute torque profile of the engine versus rotation angle, but since the only output value sought after is average power, the averaging effect of the large inertia torque shaft actually helps the measurements signal to noise ratio. The added inertia from the arms serves to decrease the main shaft's natural frequency, which in turn further dampens all high frequency vibration and engine irregularities. This inertial damping lets the DC component pass unaltered through the mechanical filter, and therefore poses no risk of mechanical attenuation. The equations and qualitative Matlab simulation proving so are shown below:

$$I_{shaft}\omega^2 = T(t) + \theta K_{spring}$$

$$\text{assuming } K_{spring} \ll K_{load\ cell}$$

$$F_{load\ cell} = K_{spring} \cdot \theta$$

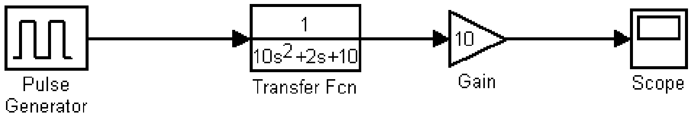

Figure 80 - Simulink Qualitative Model

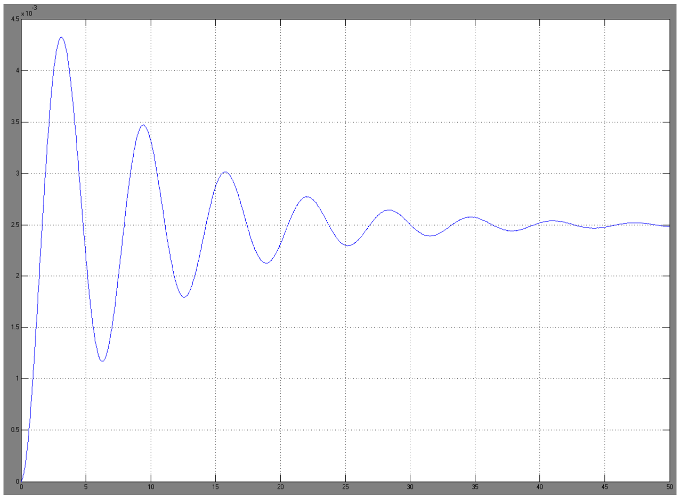

Figure 81 - Time based force input to load cell from pulsed input.

Labview VI Description

The labview VI is responsible for reading both analog, digital, and packet data inputs from the various sensors on the dynamometer. The program is configured to read load cell analog signals at 20Khz, RPM sensor signals at 20Khz, and import mass data from the scale every 0.25 seconds. When an Arduino was being used to sense RPM, labview would automatically import data each time the com port buffer reached 6 bytes. Once the data was imported, it was only a matter of applying calibration curves, computing parameters of interest, and averaging the data to produce small data files for viewing. Three separate data files are created in any one run. The largest file is a simple data dump of all data the computer collects while the labview program is running, and the collect data switch is enabled. The second file records data each time the steady switch is enabled. This file should contain only the data from valid test points. The third file contains averaged data. Whenever the "steady" button is engaged, the previous points are cleared from RAM, and all data from that point forward is averaged. Live uncertainty calculations are performed on that data in accordance with the equations presented earlier in this document. Once the uncertainty has converged to the user's liking, pressing the save data button will record a single line of data in the third and final output file. This file is meant to be a fast method of reading all desired data. Each output file contains 32 output parameters, half of which are data, and half of which give the uncertainty of said data point.

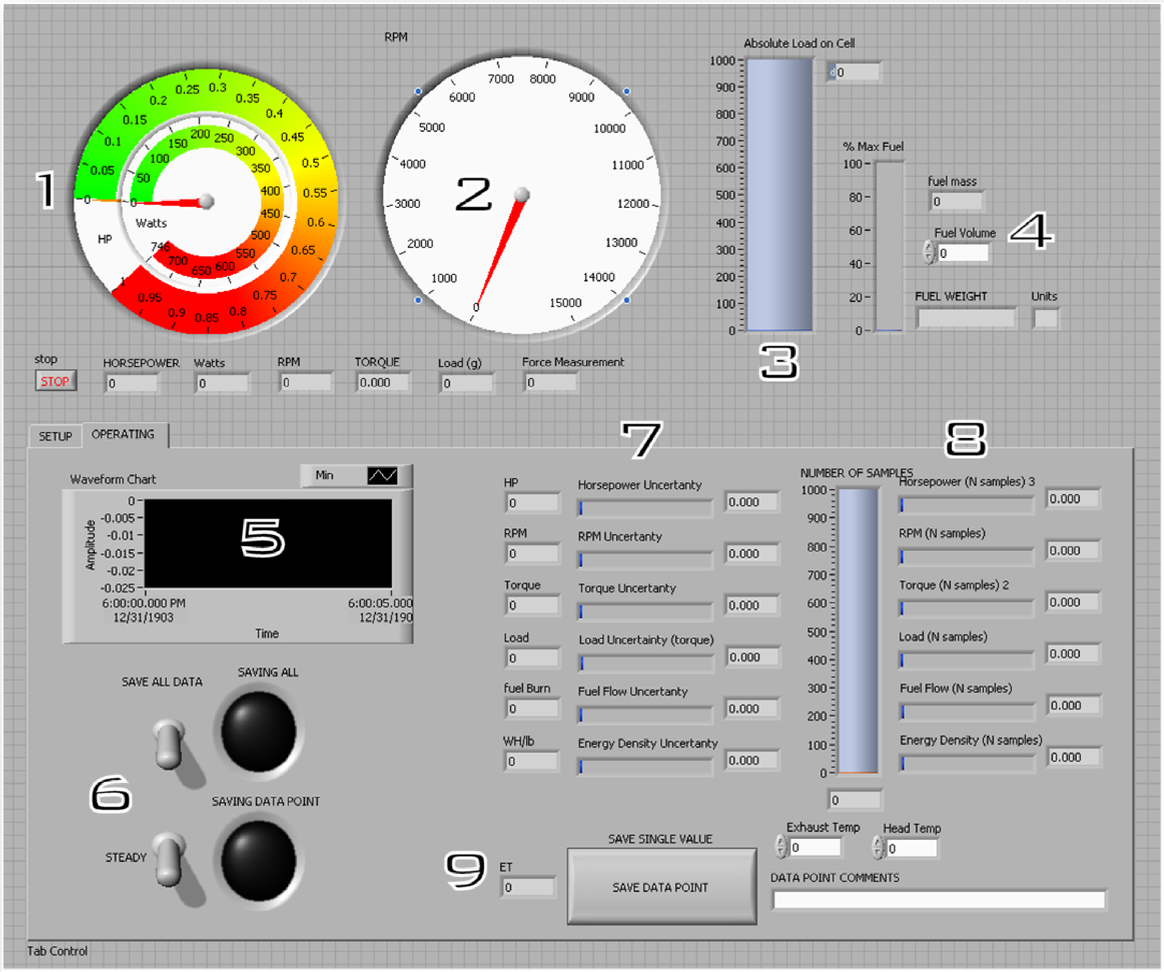

Figure 82 - Operations Tab of Lab View VI

- 1 - Output Horsepower and Watts
- 2 - RPM
- 3 - Absolute Load on Cell
- 4 - Fuel Weight Measurements
- 5 - Input Waveform from Load Cell
- 6 - Data Output Controls
- 7 - Live Single Sample Uncertainty Measurements
- 8 - Live Multiple Sample Uncertainty Measurements
- 9 - Single Data Point Output

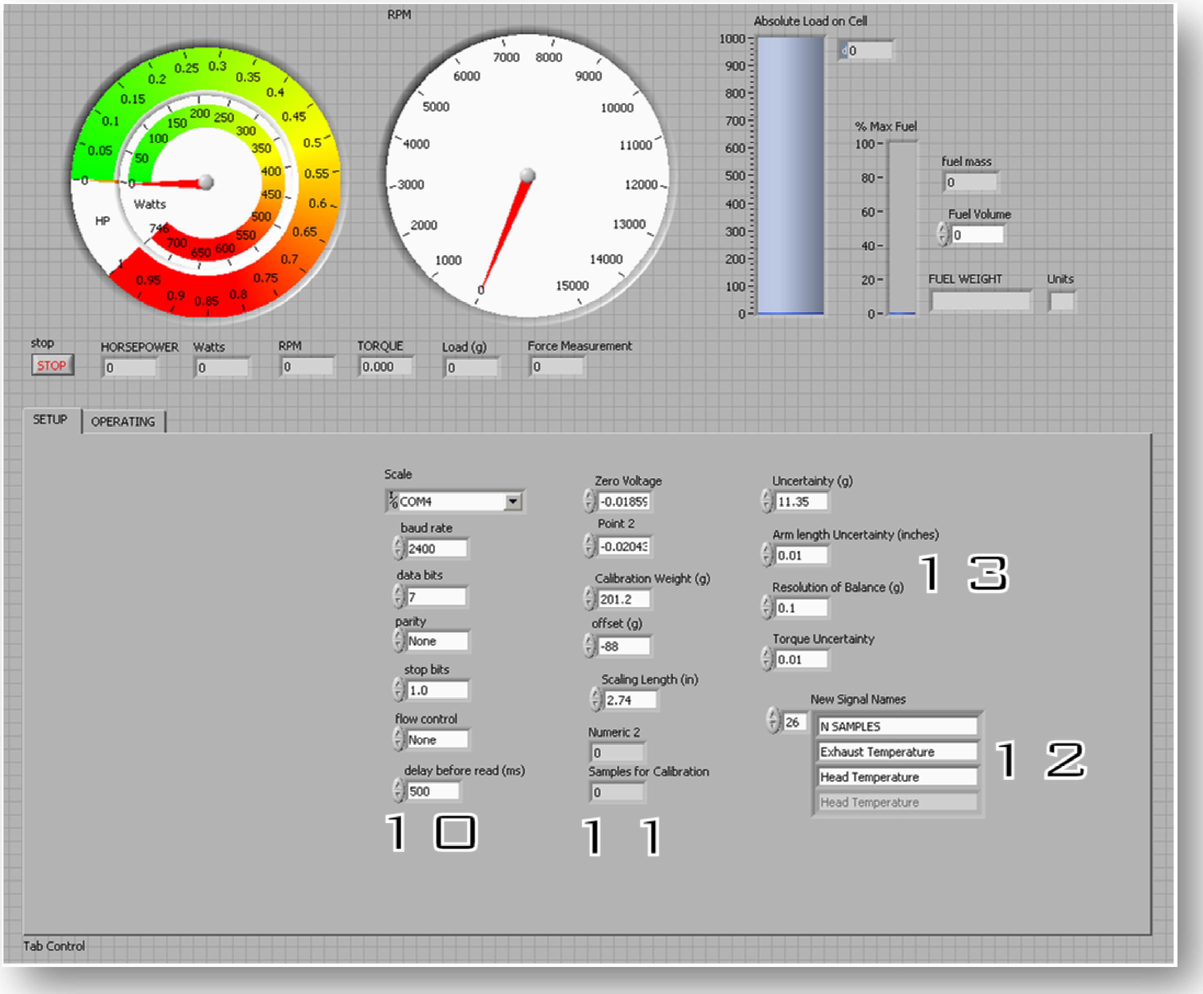

stop

HORSEPOWER 0

Watts 0

RPM 0

TORQUE 0.000

Load (g) 0

Force Measurement 0

Absolute Load on Cell 0

fuel mass 0

Fuel Volume 0

FUEL WEIGHT

Units

Scale COM4

baud rate 2400

data bits 7

parity None

stop bits 1.0

flow control None

delay before read (ms) 500

Zero Voltage -0.01859

Point 2 -0.02043

Calibration Weight (g) 201.2

offset (g) -88

Scaling Length (in) 2.74

Numeric 2 0

Samples for Calibration 0

Uncertainty (g) 11.35

Arm length Uncertainty (inches) 0.01

Resolution of Balance (g) 0.1

Torque Uncertainty 0.01

New Signal Names 26

N SAMPLES

Exhaust Temperature

Head Temperature

Head Temperature

Figure 83 - Configuration tab of Lab View VI

- 10 - Ohaus Scale COM Port Configuration
- 11 - Load Cell calibration Fields
- 12 - Data Output Labels
- 13 - Individual Sample Uncertainties

Experimental Procedure

Calibration of load cell

Although the actual torque calibration curve is based on a least squares fit of output voltages, and thus does not require the load cell to read true grams, it is important to know the load put on the cell to protect it against overload conditions. At the beginning of testing the load cell is detached from the main frame and placed on a level surface. Two calibration points are taken so that the true mV/V rating of the load cell can be calibrated. The labview VI has a segment dedicated to load cell voltage averaging, and selection of the number of averaging points. As discussed previously in the reduction of uncertainty through multiple samples of the same measurement, a larger number of averaged samples will produce a more accurate measure of the true voltage output of the load cell. The labview VI simply takes the zero load and calibration load, computes the slope between those points, and determines all further load conditions based on that data. One cause of systematic error in the load measurement would be that the calibration is conducted vertically, while measurement is conducted horizontally. This would slightly change the load condition of the cell, and introduce some systematic error into the system. This error does not affect the torque curve uncertainty, because the torque calibration, and load cell calibration are independent of one another. The load cell calibration is only for purposes of preventing overload.

Torque Calibration Curve

After the load cell has been calibrated, it is placed back into its fixture on the frame of the dynamometer. Two calibration masses are used along with a no load condition to create a three point calibration curve. One should use the technique described in the torque uncertainty section to determine the distance from shaft center to the ground spot in the torque arm. This distance is in turn used with the measured mass of the calibration weights to determine the true torque applied during calibration. In the present dynamometer setup a mass of 201.2 grams will produce .199 ft-lb of torque, while a mass of 100.6 grams will produce .1 ft-lb of torque given the present 5.398 inch moment arm. Once the expected torque is known, proceed with the following steps:

- Connect belt drive to pulley and relocate engine until mounting torque is minimized
- Zero the torque offset
- Set the scaling length to one in lab view
- Place each mass on the torque arm
- Perturb the torque shaft to eliminate any possibility of drag
- Measure and record the resulting torque
- Repeat for each calibration point
- Create curve fit of the data in Excel and extract the proper offset and slope

Following this procedure properly should produce something similar to the following plot:

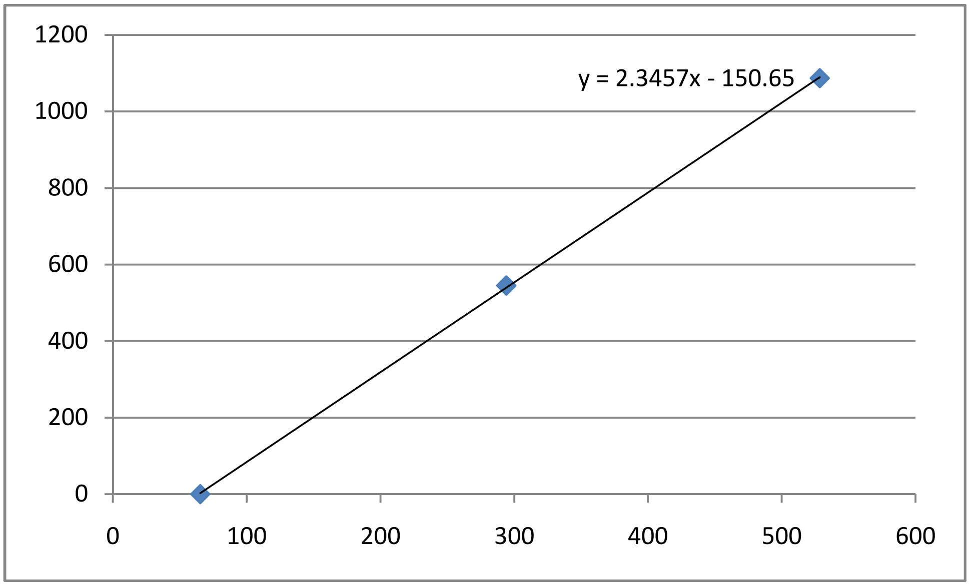

Figure 84 - Torque Calibration Curve

Where the slope of the curve fit becomes the scaling length, and the intercept becomes the zero offset. As a consequence of the load cell measuring compression only, one must ensure that the load cell experiences some load at zero torque, or the lowest torques will become immeasurable as the torque arm no longer contacts the load cell. Also, one must ensure that a calibration point does not result in the load cell bottoming out on the upper deflection stop. Especially for the case of the Futek load cell, one must monitor the output of the cell to ensure the calibration point remains in the useable range.

Large systematic error can result from a misaligned engine shaft. Any lateral displacement from the motor shaft will cause a relatively large torque to be exerted on the shaft. Although the displacement required to tension the belt is small, the high modulus of the belt's aramid core combined with the large forces that the four bolt motor mount can exert make the load system very stiff. Attach the engine, check for torque offset, then repeat and adjust until the offset torque is acceptable.

Engine Starting Procedure

Engine starting is made very simple through the use of an electric motor brake. Begin by ensuring the area around the engine and flywheel is clear of tools and other debris that could be thrown by the flywheel, or catch in the mechanism and damage the dynamometer or the engine. Next, fill the fuel system and ensure that all air has been purged out of the line. If fuel is pumped through the rotameter's too quickly, air will be sucked in at the joint between the glass rotameter tube, and the metal holder. Once the fuel system is primed, the fuel will flow naturally downhill from the burette to the fuel outlet. Use a paper clamp across a piece of folded fuel tubing to stop the flow. Close the needle valve to the engine and engage the starter motor. Slowly open the fuel valve until the engine is running smoothly, additional opening will most likely be needed to reach higher RPM's as the engine's carburetor does not adequately meter fuel across the engine operating range. Do not let the engine remain stopped without replacing the fuel line clamp or unburned fuel will drop out of the engine's carburetor. This is particularly bad for upward facing carburetor's where the fuel would flow into the engine, and could possibly cause hydro lock.

Repeatability

The only thing separating a dynamometer from a random number generator, is a thorough understanding of its uncertainty, and proof of the device's repeatability. To generate the following repeatability data, an OS 40 four stroke engine running on glow fuel with an ignition system set to 30 degrees BTDC was installed on the dynamometer. The data was taken at constant RPM, constant throttle, constant needle valve setting, but varying fuel flow rates and engine loads. The target RPM for all test points was 6500 RPM, and was maintained as best as possible by hand. Four test runs were conducted over two days, each time the dynamometer was recalibrated before use, so that any systematic error during calibration would show during testing. The throttle setting was accidentally changed after the first run of the first day of testing without being previously recorded, it is excluded from these plots, as the data would not contribute to proof of repeatability. The data gathered during those tests follows:

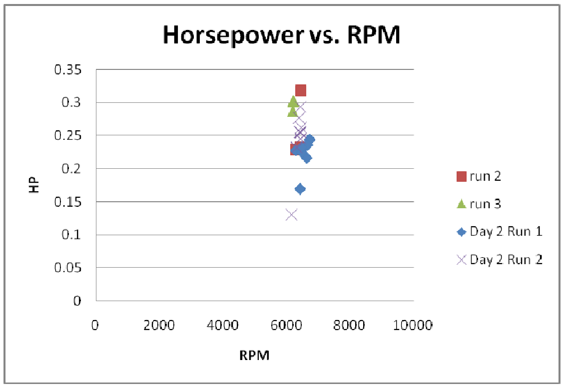

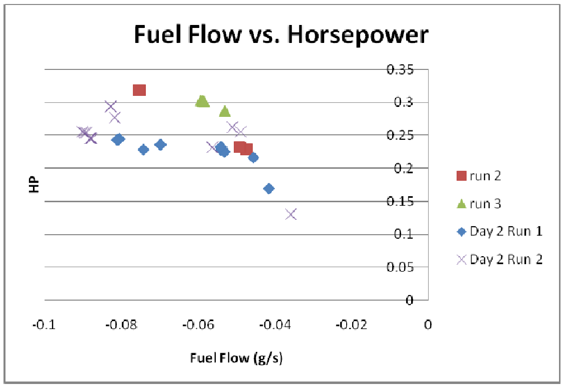

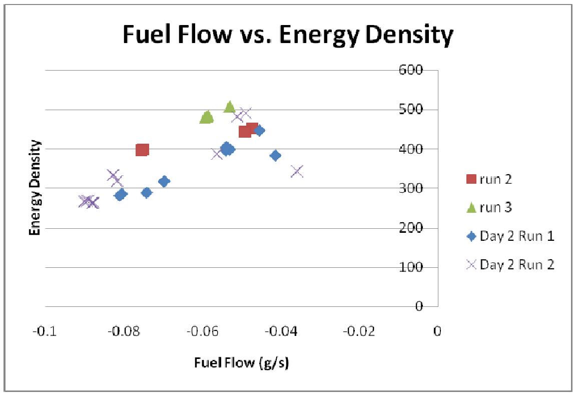

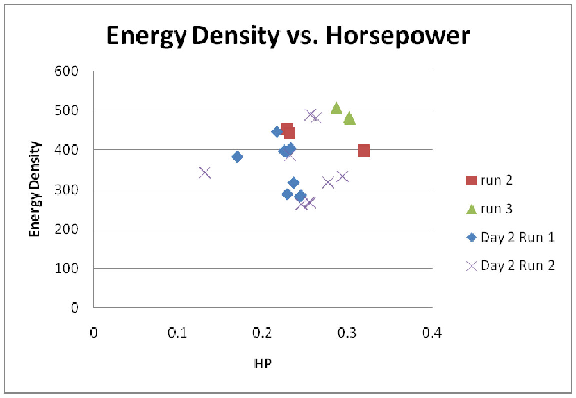

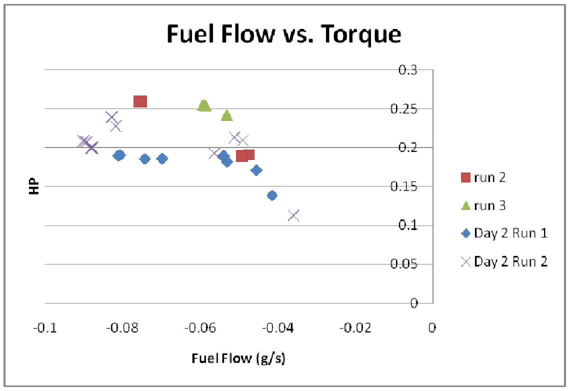

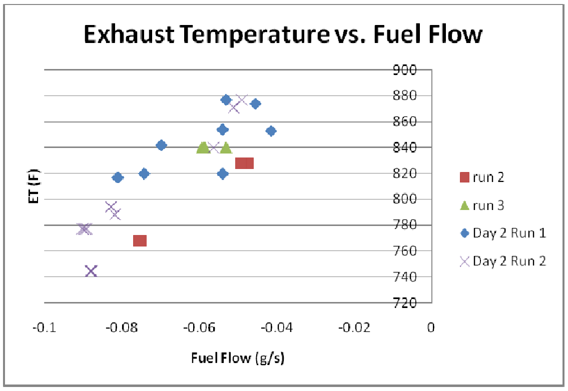

The horsepower vs. RPM plot serves little purpose other than showing the extent to which the average RPM varied among data points, and also the range of power output based simply on the fuel to air ratio. The fuel flow vs. horsepower plot is the first that can really be used to prove repeatability, the data scatter at lean running conditions up to the maximum energy density point is very small. However the data breaks apart once the maximum energy density point is passed. This is most likely due to the difficulty of controlling the RPM of a rich engine. When the engine is running lean, or on an optimal fuel to air mix it converges to a single RPM and remains there virtually unaided. Alternatively, when the engine's are ran with excess fuel they become difficult to control, often wanting to accelerate, or becoming bogged down from what one can only assume is incomplete combustion. The problem becomes more and more pronounced as more fuel is added. The two plots below show the RPM vs. time plots for a rich and lean data point. One can distinctly see the average speed of the engine changing in the rich fuel setting plot, but although the RPM data is similarly scattered in the lean plot, the average value is fairly constant. The Histogram below the two shows the relative scatter of RPM data points, and shows a surprising similarity between the RPM error of the rich and lean settings.

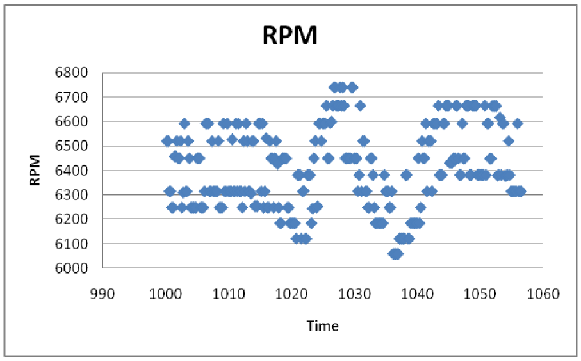

Figure 85 - RPM variation vs. Time for Rich Fuel Mixture

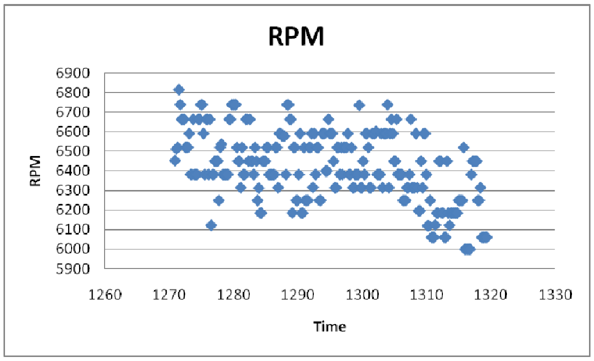

Figure 86 - RPM vs. Time for lean fuel mixture

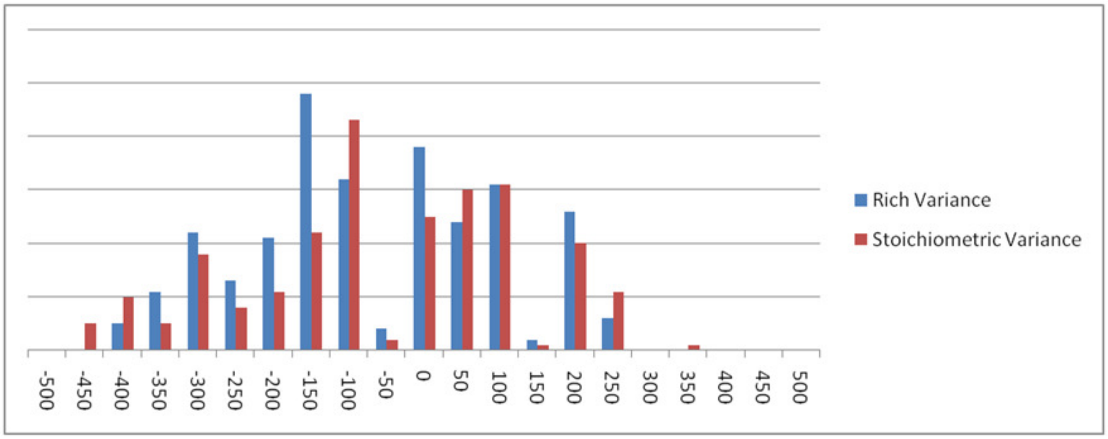

Figure 87 - RPM error compared to 6500 RPM set point

The same growth of data scatter can be seen in the fuel flow vs. energy density plot, and fuel flow vs. torque. Most every data run lies on the same path except for the first run of the second day. This data is only plagued by a lack of horsepower at rich settings, but still converges to the mean path at stoichiometric, and lean conditions. The similarities at the endpoints of the fuel flow vs. horsepower plot could indicate that the dynamometer was calibrated properly, and producing repeatable data, but the engine itself was not producing the same amount of power at that point. Additionally if one looks at the exhaust temperature vs. fuel flow rate plot, the three anomalous data points also have much higher than average temperatures which could indicate some type of cycle difference. Overall, whether the small difference is a result of poor manual RPM control, or a true variation in the engine's cycle, the dynamometer has been proven sufficiently repeatable over these four tests.

Dynamic Calibration

The powerful vibrations and excitation of the dynamometer brought the frequency dependent calibration of the dynamometer into question. A test was conducted where the 0.1 ft-lb mass was taken on and off the torque arm of the dynamometer to ensure the output torque was incrementing correctly. The resulting plot of torque is shown below with each point representing the averaging of approximately 2000 data points.

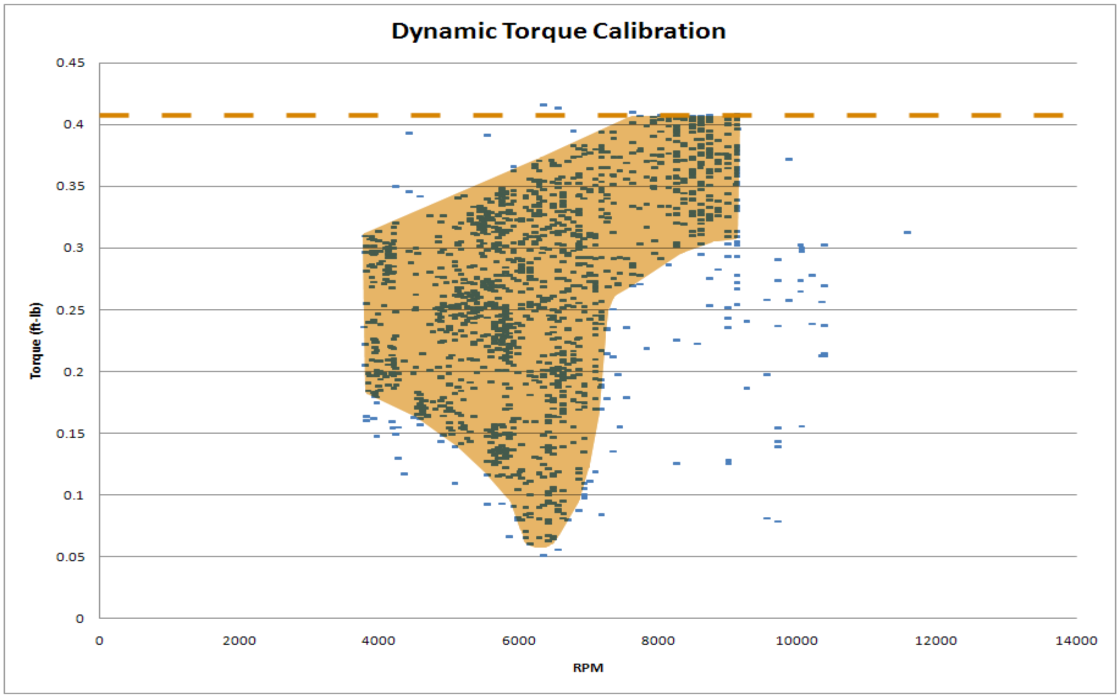

Figure 88 - Dynamic Calibration Plot

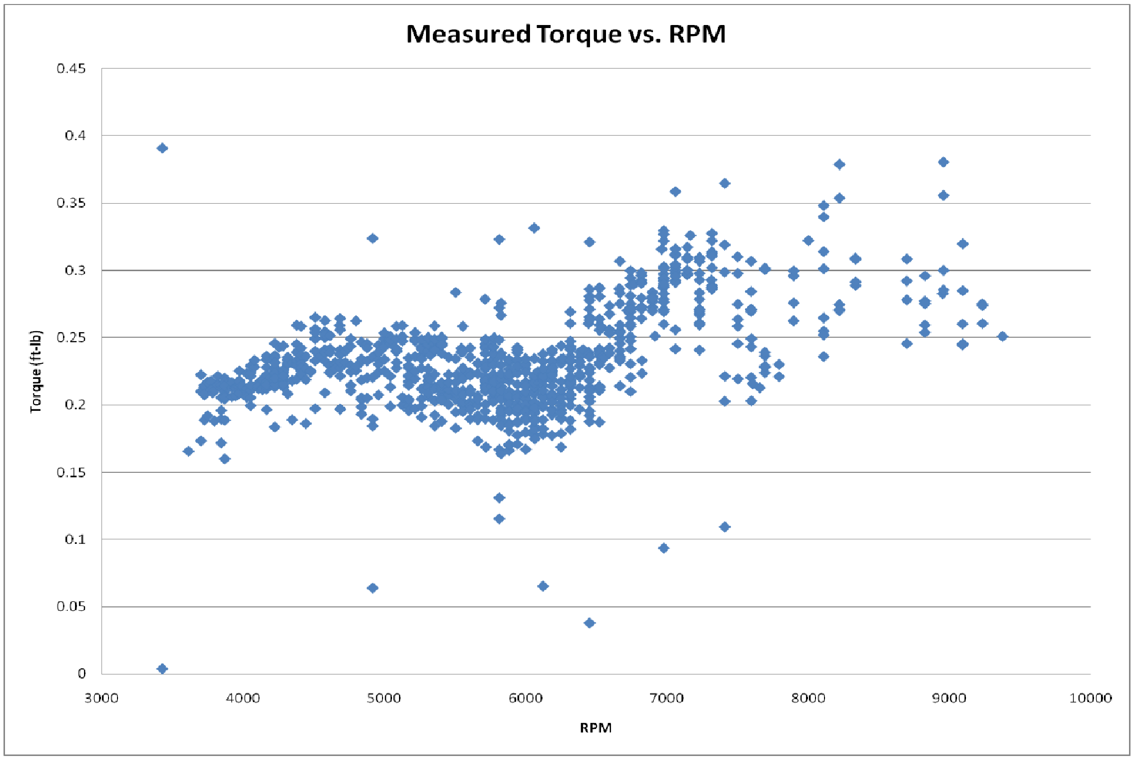

Figure 89 - Measured Torque vs. RPM

One can see several distinctive and worrisome features above. The orange line represents the maximum load condition of the Futek load cell and one can see that above 8000 RPM the engine's torque combined with the added calibration torque caused the load cell to rest against its deflection stop, making any further measurements above 8000 RPM useless at the current moment arm setting. The most worrisome feature is the wide scatter in data from 5000 to 7000 RPM caused by the excitation of the torque arm . In the second plot, an unnatural decrease in measured torque can be seen to coincide with the resonant RPM of the torque arm. All of the washers were removed from the torque arm in an attempt to shift the natural frequency of the arm outside the typical operating range of the dynamometer. The resulting plot from that test is shown below:

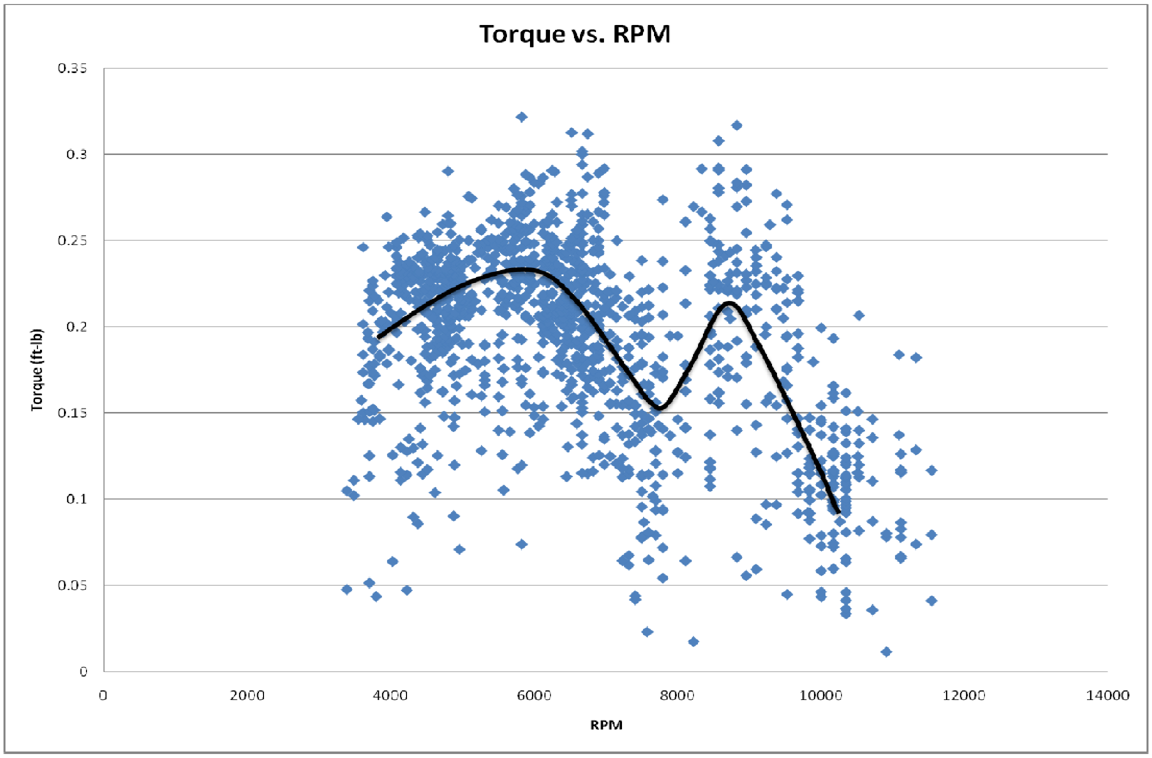

Figure 90 - Torque vs. RPM with Reduced Inertia

As one would expect, the data appears more scattered than in the previous test conducted with more torque arm inertia, but the shift in the resonant frequency of the dynamometer can be seen. Previously the measurements were affected from 5000 to 7000 RPM, and in the plot above the reduced inertia shifted the affected region to between 6000 to 9000 RPM. It was obvious that simply reducing inertia would not shift the resonant frequency high enough, and the stiffness of the torque "spring" is somewhat fixed because of load cell protection measures. Although the braided fishing line was very stiff in tension, its spring force in compression was negligible making the effective K very small. It was decided to leave the load cell protection in place, and solve the resonant frequency problems through other means.

The proximity of the maximum allowable torque on the load cell to the measured value of torque, combined with the repeatable trend of measured torque being lower than theoretical values in the resonant region, in addition to the sampling rate being well above the nyquist frequency of torque arm resonance meant that the dip in measured torque was a result of mechanical limitation of the load cell. The torque arm was raised to accommodate up to 0.9 ft-lb of torque being exerted, and the reduced inertia test was repeated with the following results:

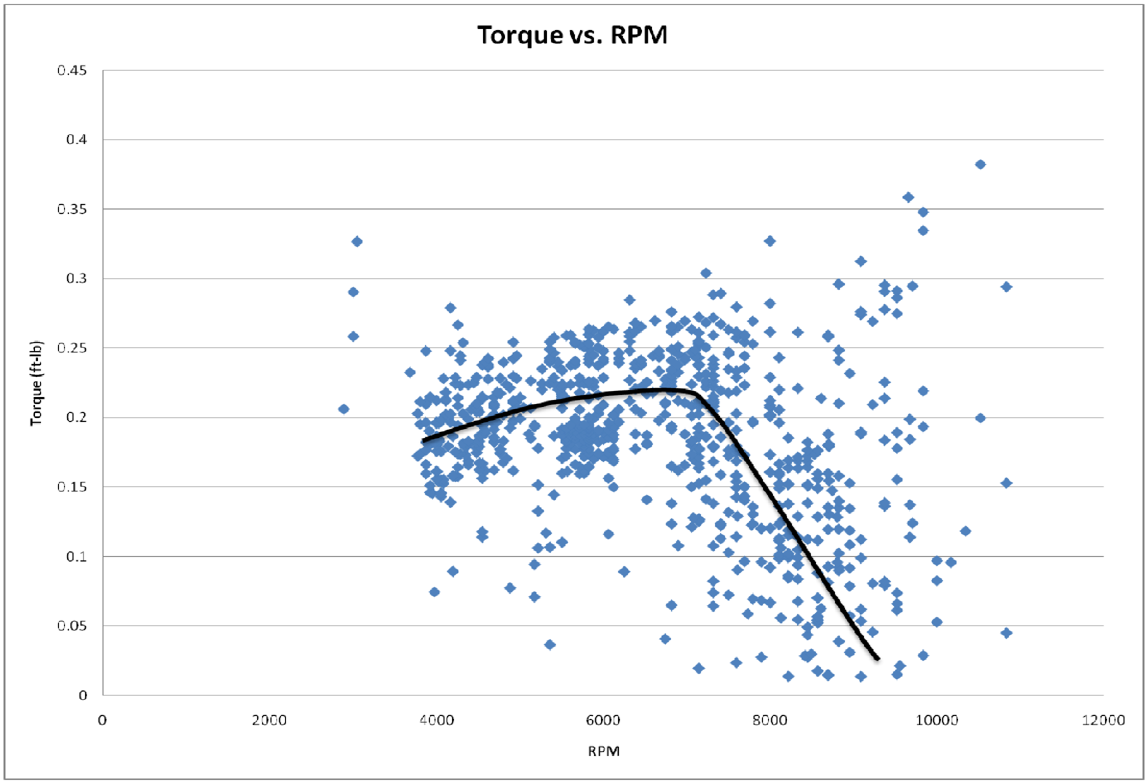

Figure 91 - Torque vs. RPM with higher maximum load.

The dip in measured torque was no longer present, meaning both the peak and trough of the torque waveform was being successfully captured. Even though the uncertainty of the load cell increased due to the mean value of torque measurement being a lower percentage of the maximum allowable torque, the average values over 2000 samples show no expansion in their random uncertainty. With the dynamic calibration problem solved, the washers were added back to the torque arm to increase vibration attenuation, and the test repeated with the following results:

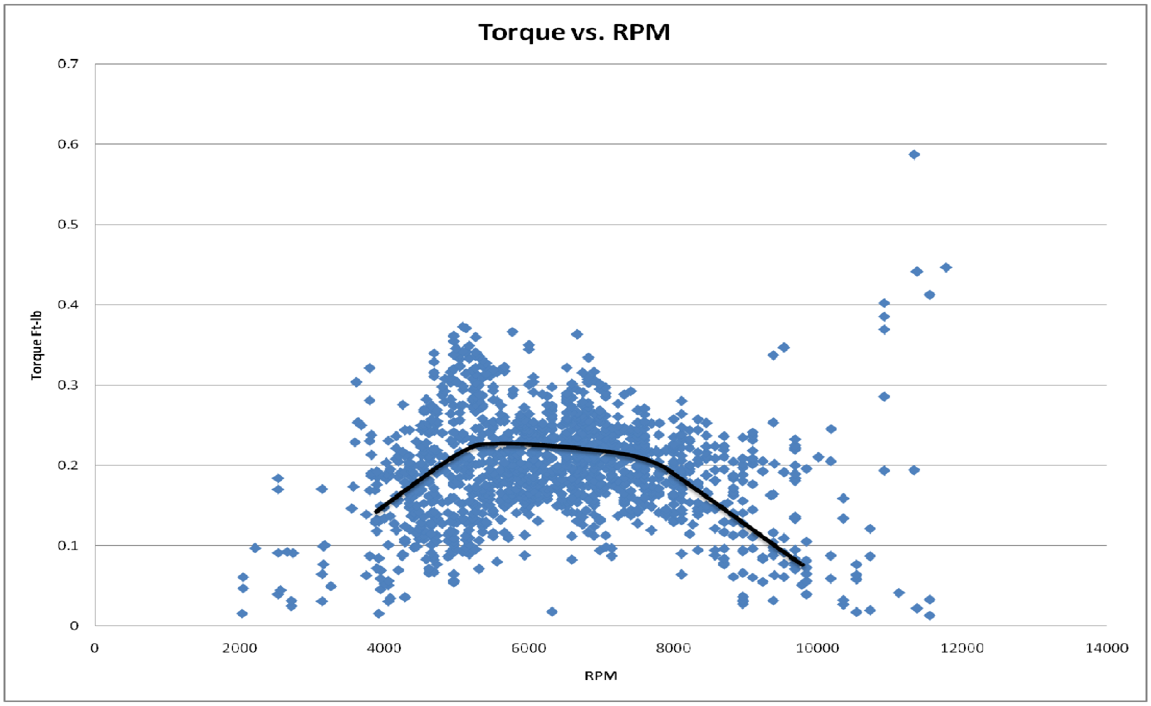

Figure 92 - Torque vs. RPM Resonant Dip Absent

Although the scatter of torque measurements remains high, the previous dip in indicated torque at the resonant frequency is now absent. The number of samples per data point was increased from 2000 to 10,000 to reduce scatter of individual measurements, and the dynamic verification of calibration was complete. All final output data points contain hundreds of individual torque points, so the scatter shown in all the above plots is statistically reduced before data is considered converged.

Engine Data

OS 0.40 CI Four Stroke Glow Plug Ignition 20% Nitro Methane Fuel

Manufacturer's Data:

- Bore: 21.2mm (.835")
- Stoke: 18.4mm (.724")
- Power Output: .65 BHP at 12,000 RPM
- Weight- w/o muffler: 12.5oz (354g)
- with muffler: 13.3oz (377g)
- Practical RPM Range: 2,200 - 12,000 RPM
- Crankshaft Thread Size: 1/4-28
- Height: 98mm (3.85")
- Construction: Aluminum and aluminum alloys

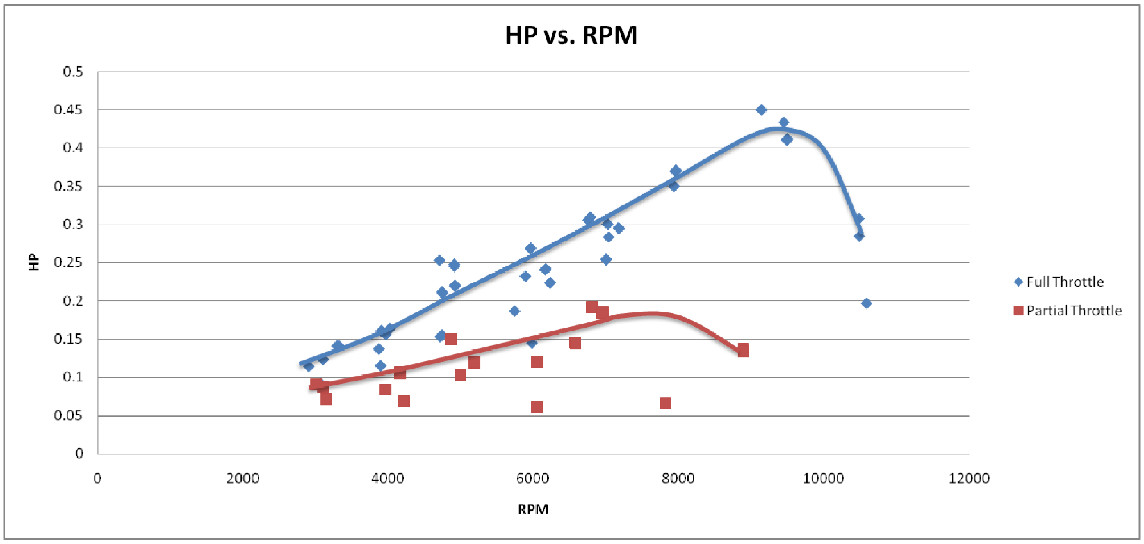

Figure 93 - Hp vs. RPM - OS 40 FS 20% Nitro Methane Glow Plug

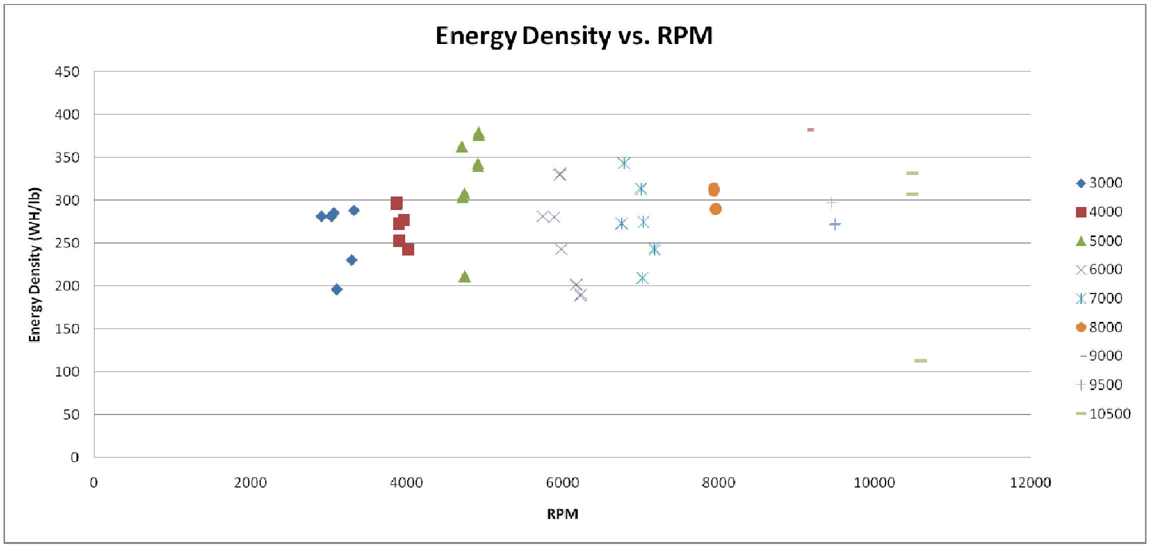

Figure 94 - Energy Density vs. RPM - OS 40 FS 20% Nitro Methane Glow Plug

In the above plots, the horsepower and energy densities at 5000 RPM should be accepted only with the understanding of increased systematic error due to vibration. Since all other data points indicate a linear relationship between horsepower and RPM up to 9000 RPM, the higher points at 5000 were excluded from the stated curve.

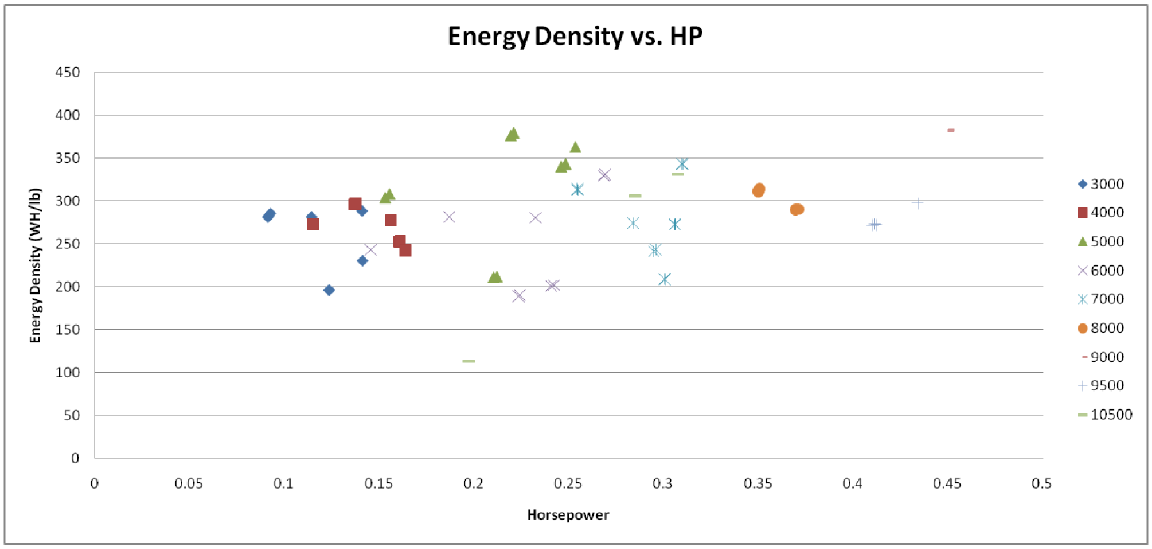

Figure 95 - Energy Density vs. HP - OS 40 FS 20% Nitro Methane Glow Plug

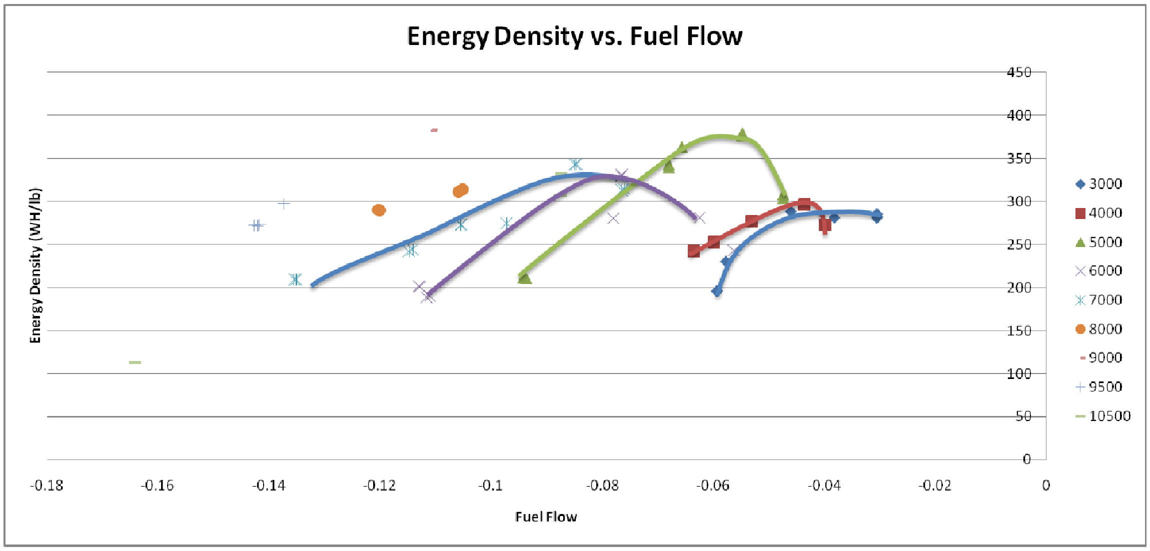

Figure 96 - Energy Density vs. Fuel Flow - OS 40 FS 20% Nitro Methane Glow Plug

A strong relationship between energy density and fuel flow exists. This plot is of great use when determining the proper fuel flow map for and engine designed for high efficiency operation.

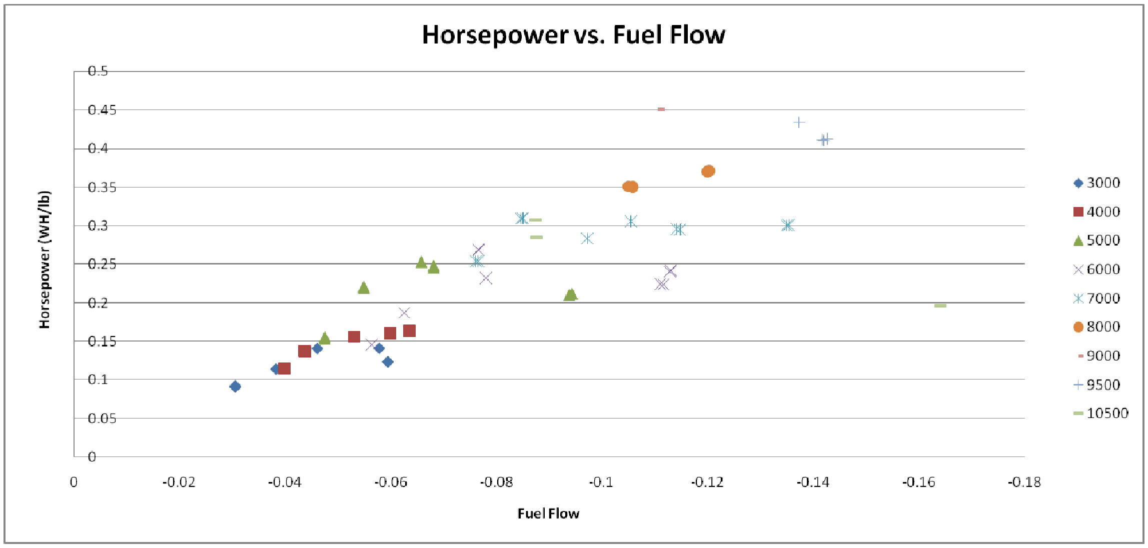

Figure 97 - Horsepower vs. Fuel Flow - OS 40 FS 20% Nitro Methane Glow Plug

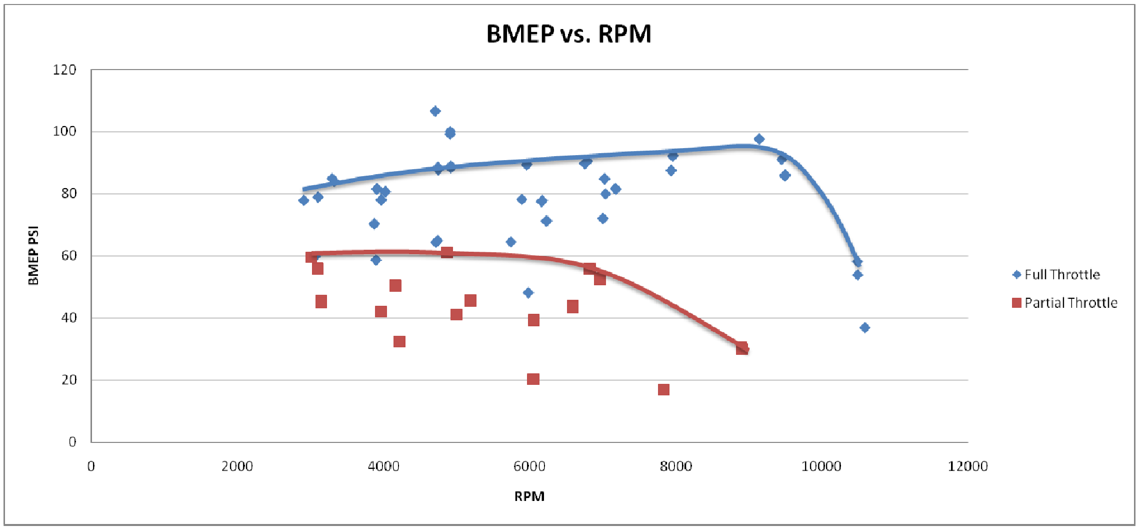

Figure 98 - BMEP vs. RPM - OS 40 FS 20% Nitro Methane Glow Plug

The top figure shows the strong relation between fuel flow and horsepower, this plot can be used to create a fuel map for ideal power under operating conditions. The bottom plot shows the variation of brake mean effective pressure (BMEP) with engine speed. One can see that at full throttle the cycle breaks down near 9000 RPM, while at partial throttle, the air restriction causes the BMEP to steadily decrease after 6000 RPM. Typical naturally aspirated large engines have BMEP's ranging from 125-150 making the OS 40 FS non-ideal, but respectable for a small engine.

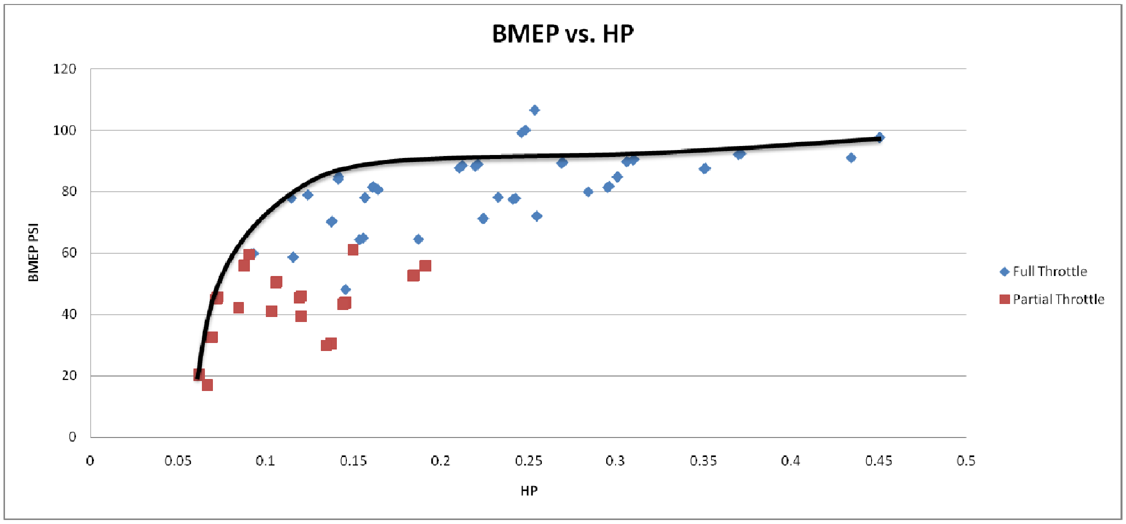

Figure 99 - BMEP vs. Horsepower - OS 40 FS 20% Nitro Methane Glow Plug

OS 0.46 Two Stroke Glow Plug Ignition 20% Nitro Methane Fuel

Manufacturers Data:

- Construction: Aluminum 1-piece crankcase, piston, cylinder head
- Bore: 23.0mm (0.906")
- Stroke: 18.4mm (.724")
- Horsepower: 1.2 BHP at 15,000 RPM
- Weight: 272g (9.6oz without muffler)
- Crankshaft Thread Size: 1/4-28
- Bushings (no ball bearings)
- Practical RPM Range: 2,000 - 16,000 RPM (This engine will not turn this many RPM on the ground) RPM curve is when the engine unloads.

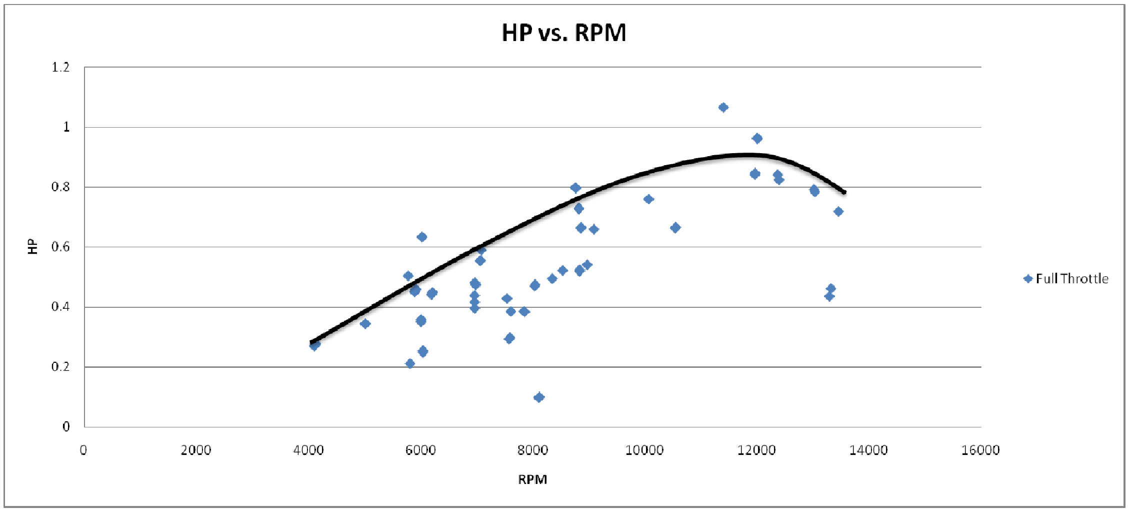

Figure 100 - Horsepower vs. RPM - OS 46 LA - Glow Ignition - 20% Nitro Methane Fuel

Peak horsepower values fall short of the manufacturers specification of 1.2 BHP at 15,000 RPM. The engine failed to reach that speed even at minimal dynamometer load. The manufacturer notes that the engine will only reach maximum speed in flight, but as the above horsepower plot shows, the peak horsepower begins to drop off around 12,000 RPM. If the engine did reach 15,000 RPM when all load is removed, it most certainly would not be producing 1.2 BHP.

Horsepower scatter in the plot above is due to variable bearing friction, changing engine temperature, cylinder head screws backing out, and of course variable fuel mixture. During engine start, if the fuel lines were not immediately primed with fuel to be pushed through the crankcase, the change in bearing friction was quickly apparent in the amount of current the motor had to source to crank the engine.

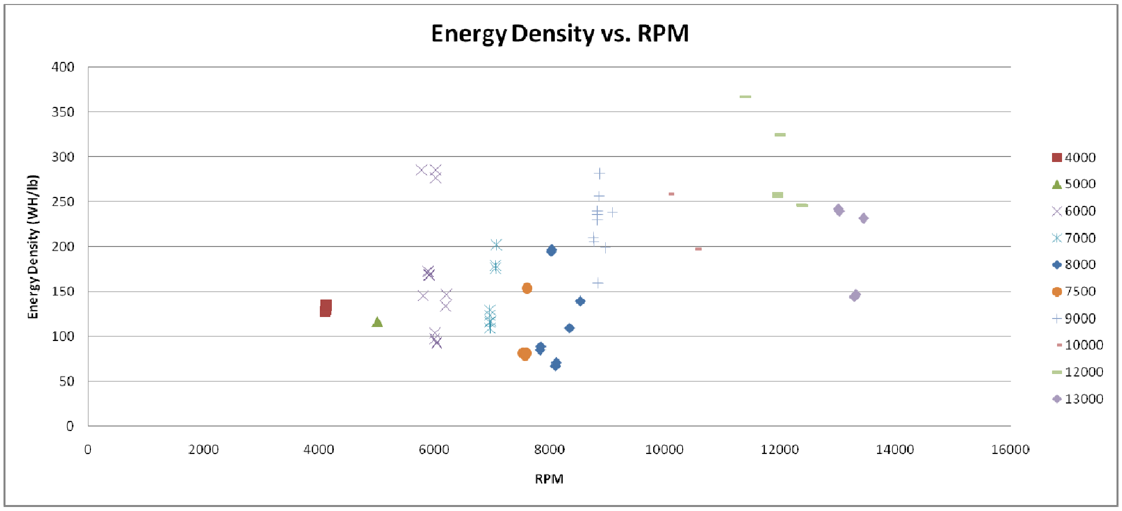

Figure 101 - Energy Density vs. RPM - OS 46 LA - Glow Ignition - 20% Nitro Methane Fuel

One can easily see a linear relation between the maximum energy density and RPM. Three points lie off that line at 6000 RPM, and were taken at two separate times during testing, so cannot be completely anomalous. Those points lie at half of 12,000 RPM where peak energy density occurs, and one could theorize that whatever cycle mechanism occurs at 6,000 RPM is reaching a harmonic at 12,000 RPM.

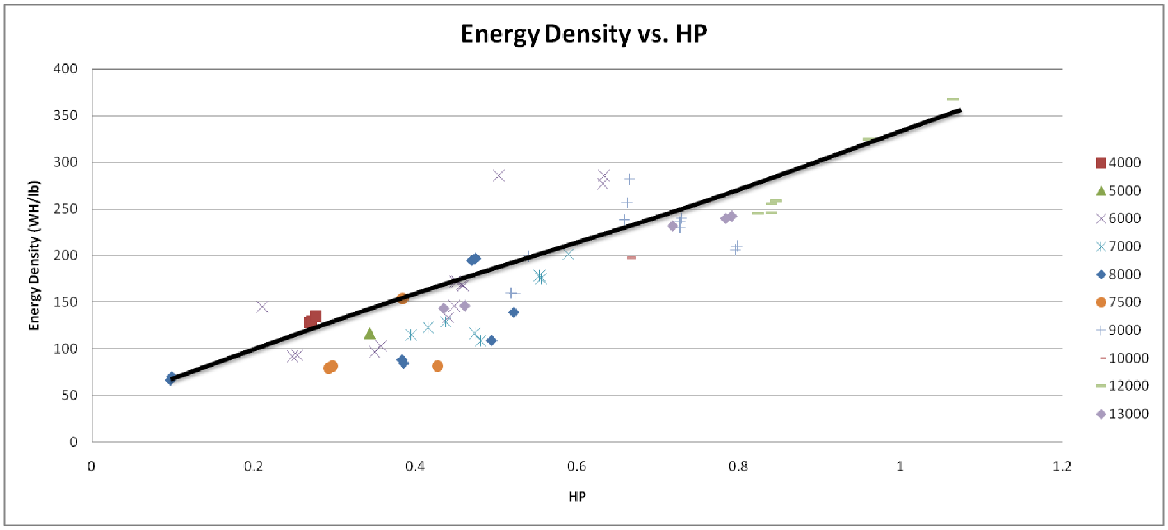

Figure 102 - Energy Density vs. Horsepower - OS 46 LA - Glow Ignition - 20% Nitro Methane Fuel

The linear relation between energy density and horsepower in the figure above is an interesting feature of the two stroke cycle. Except in the case of the outlying points at 6,000 RPM, an optimization of fuel to air ratio cannot restore peak energy density at all operating power levels.

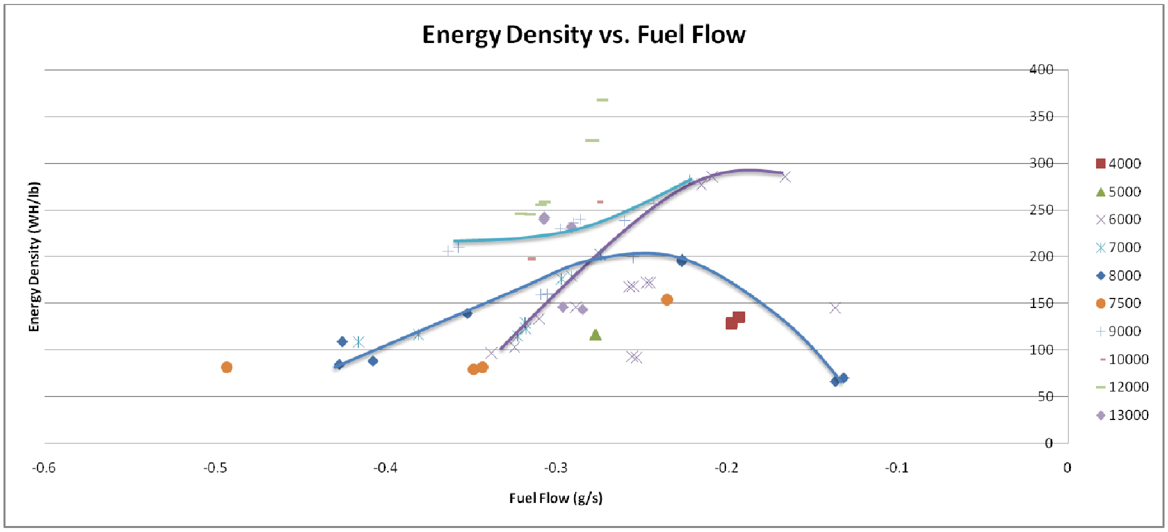

Figure 103 - Energy Density vs. Fuel Flow - OS 46 LA - Glow Ignition - 20% Nitro Methane Fuel

The energy density vs. fuel flow plot shows as expected that proper fuel to air ratios are necessary for producing maximum energy density. Both lean and rich settings will reduce the efficiency of the engine. One must also remember that for the OS 46 LA, energy density also depends on output horsepower.

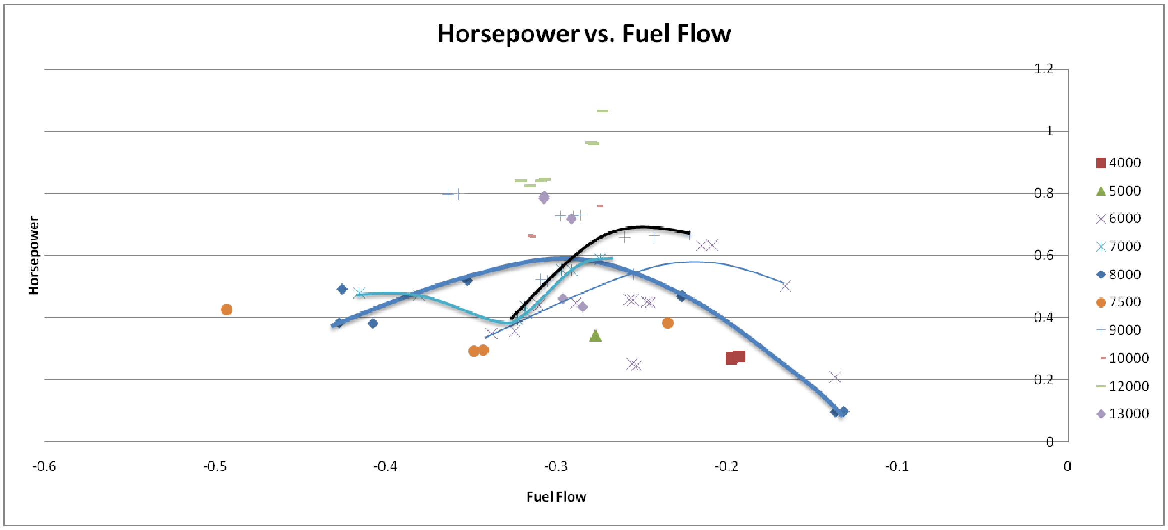

Figure 104 - Horsepower vs. Fuel Flow - OS 46 LA - Glow Ignition - 20% Nitro Methane Fuel

Similarly to energy density, horsepower also varies with fuel flow. The maximum power point occurs at a slightly higher fuel flow rate than that of the maximum efficiency point. Maximum power depends on complete combustion of the air-charge, while maximum efficiency demands complete combustion of fuel.

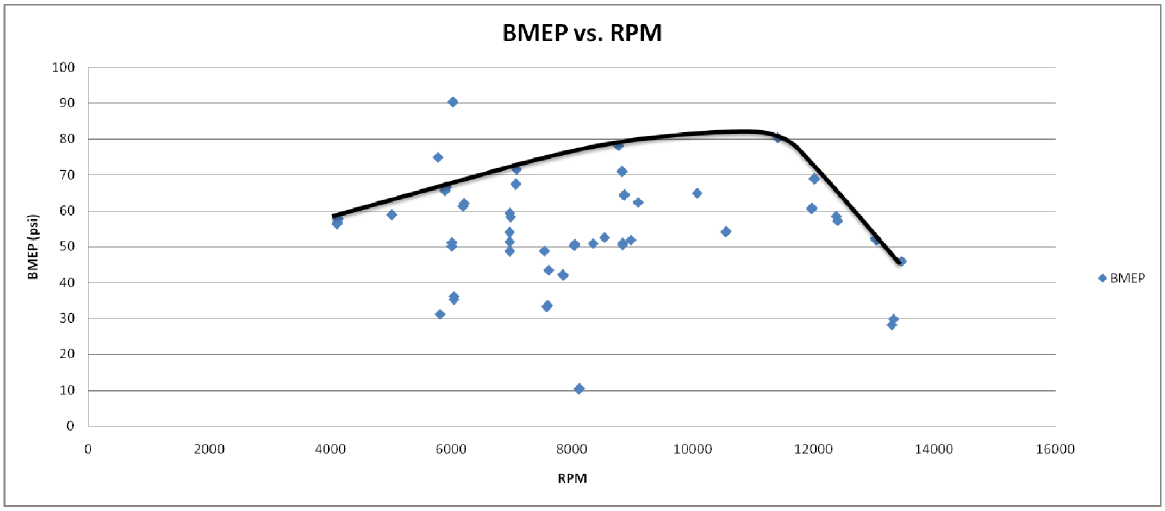

Figure 105 - Brake Mean Effective Pressure vs. RPM - OS 46 LA - Glow Ignition - 20% Nitro Methane Fuel

The variable BMEP with RPM is expected in a two stroke engine where scavenging and exhaust backpressure are both changing with engine speed. Again the cycle is shown to break down just before 12,000 RPM. The plot of BMEP vs. horsepower below shows excellent correlation between the power output and maximum per cycle power efficiency.

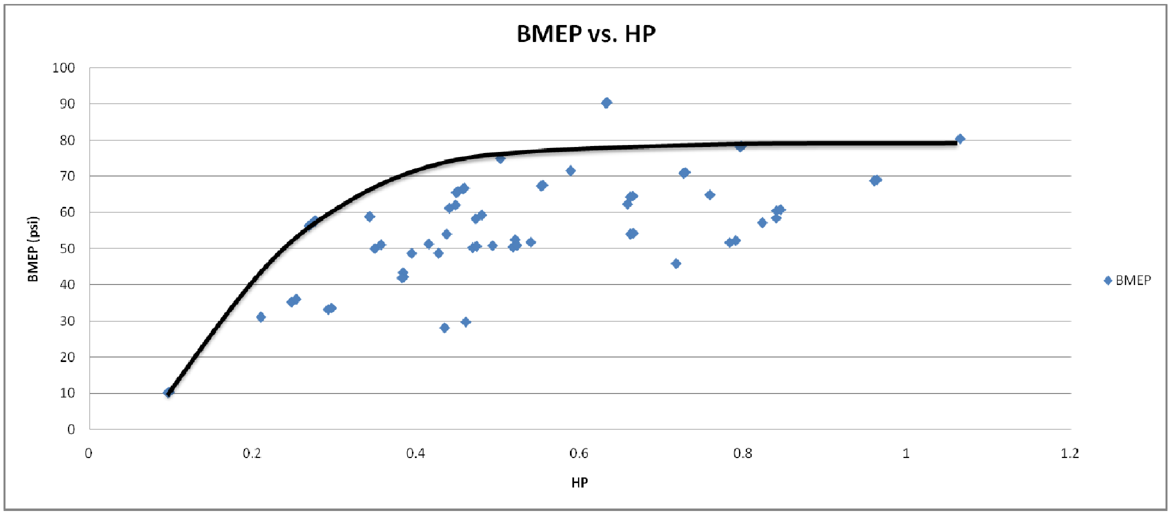

Figure 106 - Brake Mean Effective Pressure vs. Horsepower - OS 46 LA - Glow Ignition - 20% Nitro Methane Fuel

Two and Four Stroke Engine Comparisons

The test engines were selected to be from the same brand and of comparable displacement. OS did not offer a 0.40 cubic inch engine at the time of this study therefore all data below has been placed in units of horsepower per cubic inch.

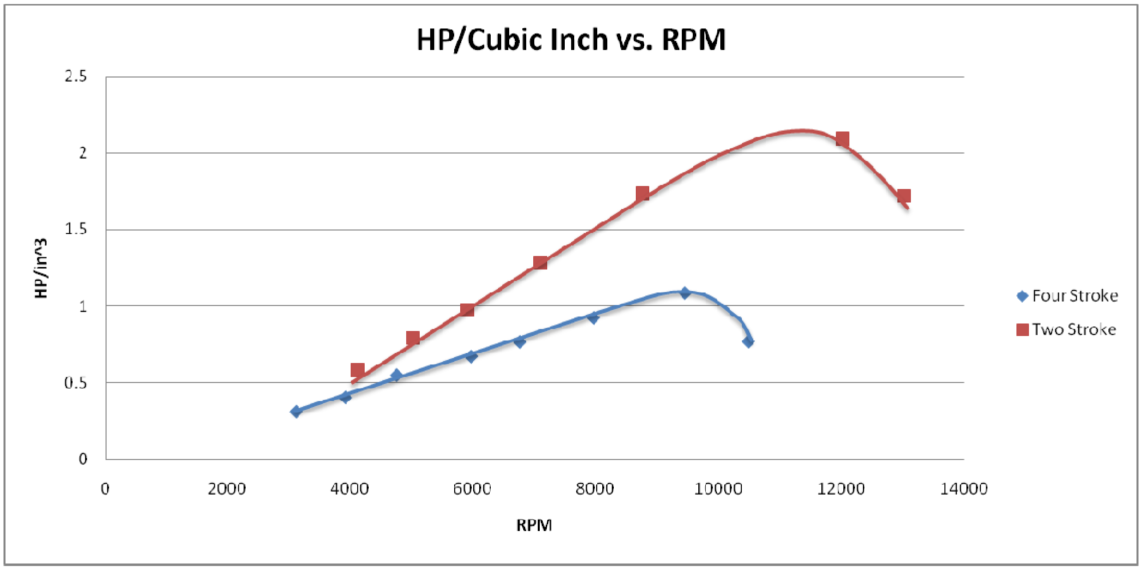

Figure 107 - Horsepower per Cubic Inch vs. RPM

The previous plot shows the relative power per cubic inch of both the OS 40 Four Stroke, and the OS 46 LA. As one would expect, the two stroke engine's power curve is 1.95 times the slope of the four stroke engine. But, that does not necessarily mean that at any RPM the two stroke is twice as powerful. Perhaps due to the use of bushings instead of bearings, or other mechanical reasons, the two stoke engine's zero power speed is much higher than that of the four stroke engine. This shifts the power curve of the two stroke engine down, minimizing its power advantage at low RPM's. To look at the difference in cycle power, BMEP should be considered as shown below.

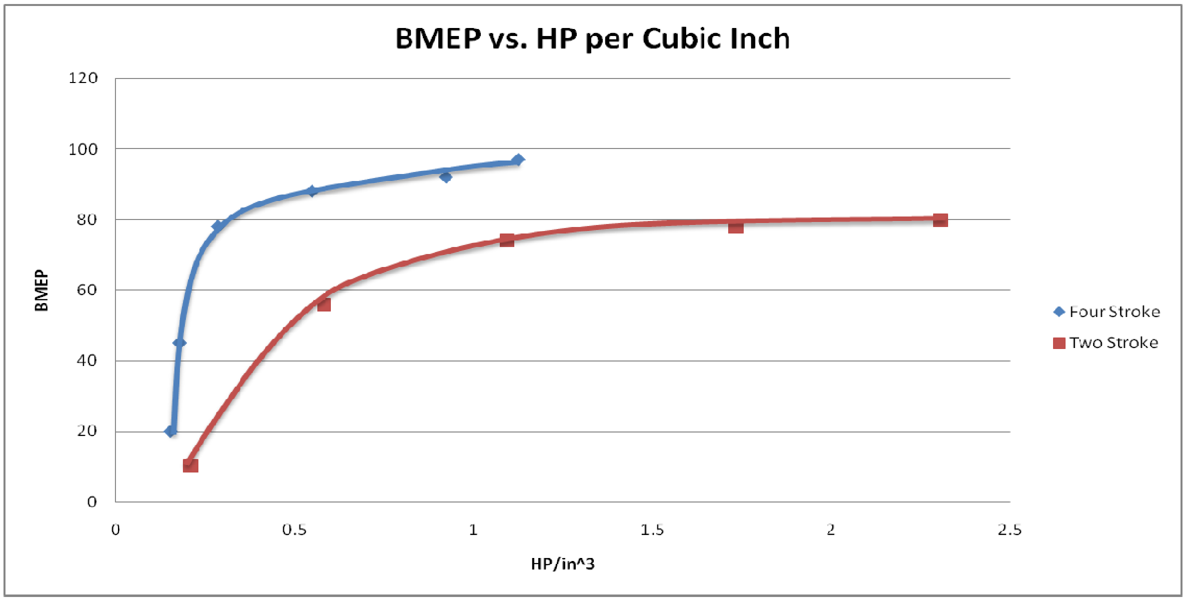

Figure 108 - Brake Mean Effective Pressure vs. Horsepower

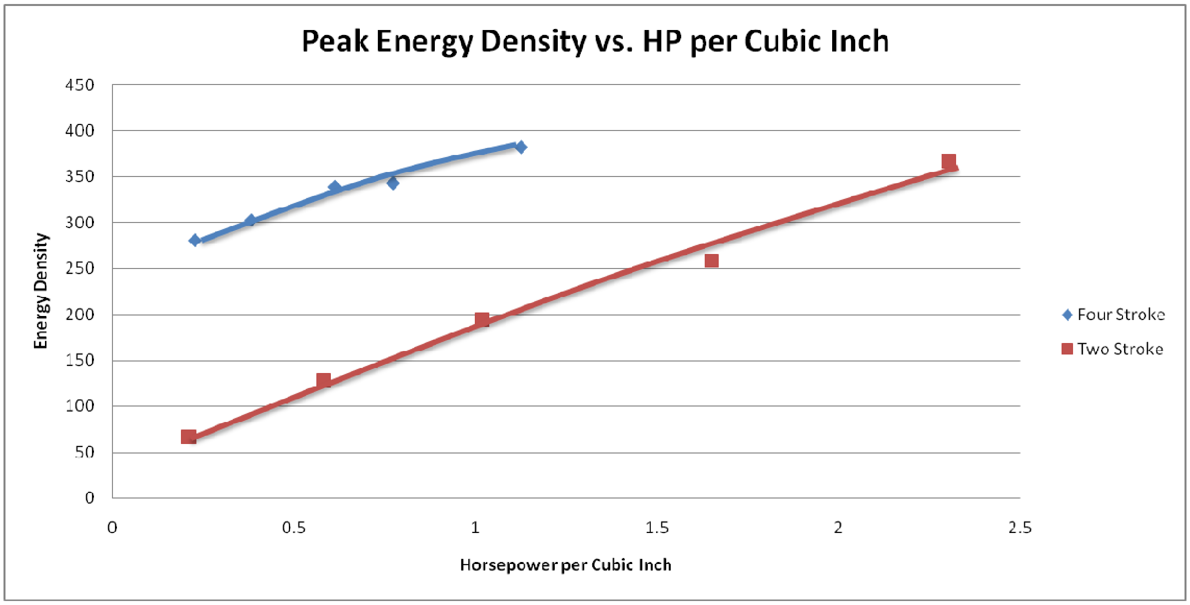

Figure 109 - Peak Energy Density vs. Horsepower per Cubic Inch

The above plot shows the peak energy densities for the tested two and four stroke engines. One can see that under ideal maximum power conditions, the two stroke engine can produce similar energy densities to four strokes when operating a peak horsepower. It is of no surprise that four stroke engine outperforms the two stroke at low speed due to its superior cycle control. The very intriguing thing is the similarity between the slopes of the two and four stroke curves. In an ideal model, one would expect the energy density to be constant no matter the output power. Variance in the cycle efficiency of a two stroke engine would be expected because of scavenging changes, but for the four stroke engine to follow a similar efficiency slope is surprising. The compression ratio is not horsepower dependent, all presented points are at optimal mixtures, which leaves only scavenging, heat loss, and glow ignition effects as possible causes. The extremely different flow mechanisms in each engine should rule out scavenging as the cause of similar slopes. If the reduction in maximum energy density was a result of scavenging, one would expect a two and four stroke engine to have vastly dissimilar plots. Heat loss is also an unlikely reason for the similarity, as even a large change in heat loss could never produce the seven fold energy density increase the two stroke engine exhibits. This leaves glow plug ignition as the only possibility. As volumetric power decreases, so does the heat flow, which would lower the average temperature of the glow plug, in turn changing the ignition angle of the fuel. In addition, some fuel is undoubtedly burned immediately upon contact with the hot glow plug in a very inappropriate engine angle, higher output power correlates to higher engine speed which in turn means shorter amounts of time for fuel to burn itself wastefully on the exposed glow plug. Verification of this theory should come from duplicating either engine's operation with a spark ignition system that would ignite at the same angle independent of cylinder temperature, ambient pressure, or other environmental factors. If one consults the energy density vs. horsepower plot for the Coleman fuel powered engine below, the operating energy density is rather independent of output horsepower leading one to believe that glow plug ignition is to blame for the reduction of efficiency with output power.

OS 0.40 Four Stroke Spark Ignition Coleman Fuel

Tests were concluded after the engine's bearings were damaged from lack of lubrication at the first test point of 7000 RPM. Output power, and energy density in the following tables will represent the lower limit of the capability of a properly lubricated engine.

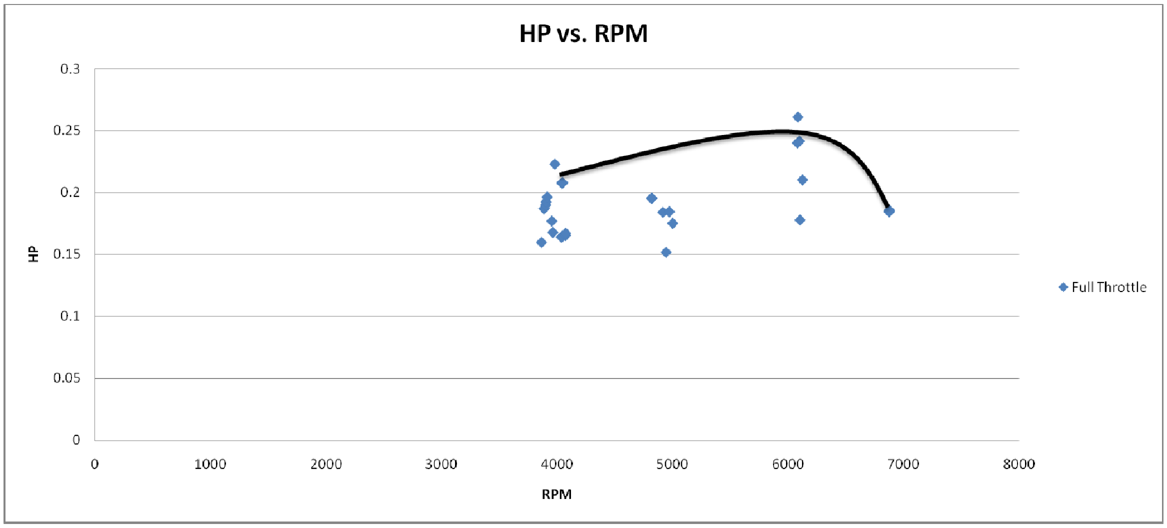

Figure 110 - Horsepower vs. RPM - OS 40 FS - Coleman Fuel - Spark Ignition

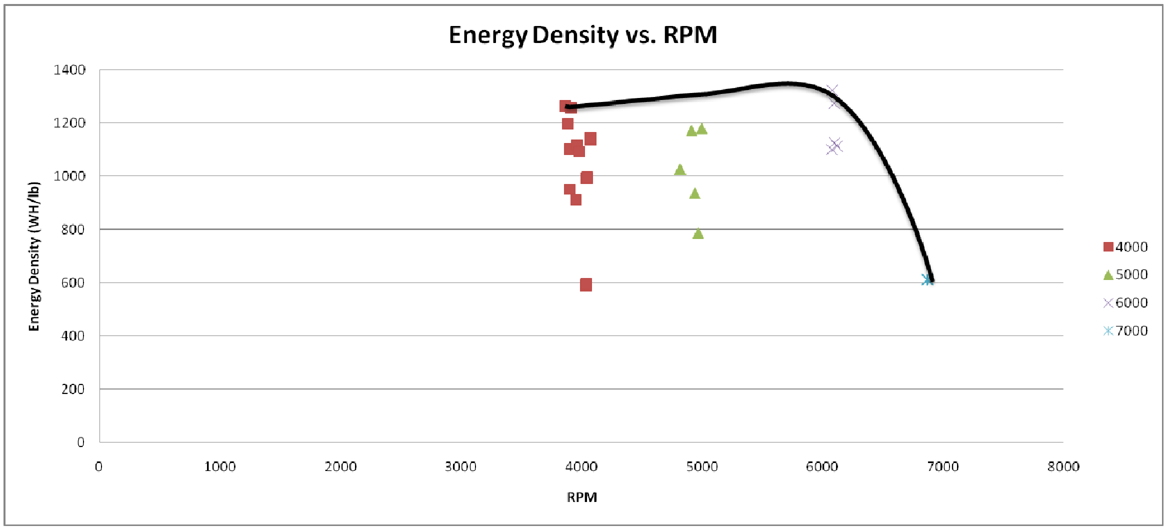

Figure 111 - Energy Density vs. RPM - OS 40 FS - Coleman Fuel - Spark Ignition

The drop in power from 6000 to 7000 RPM should be ignored, as that power drop is due to the bearings in the engine going out due to lack of lubrication. The OS 40 FS engine is designed to take un-combusted oil from the cylinder and let that pass into the crank case. Crankcase pressure in turn circulates that oil through both main bearings, the cam housing, and up the pushrod sleeves into the cylinder head to lubricate the rockers.

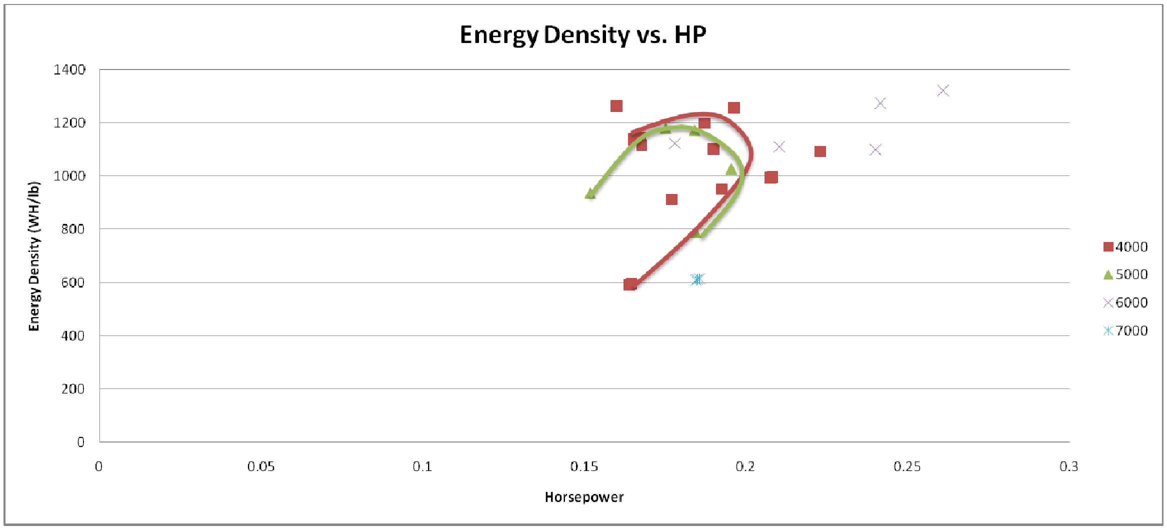

Figure 112 - Energy Density vs. Horsepower - OS 40 FS - Coleman Fuel - Spark Ignition

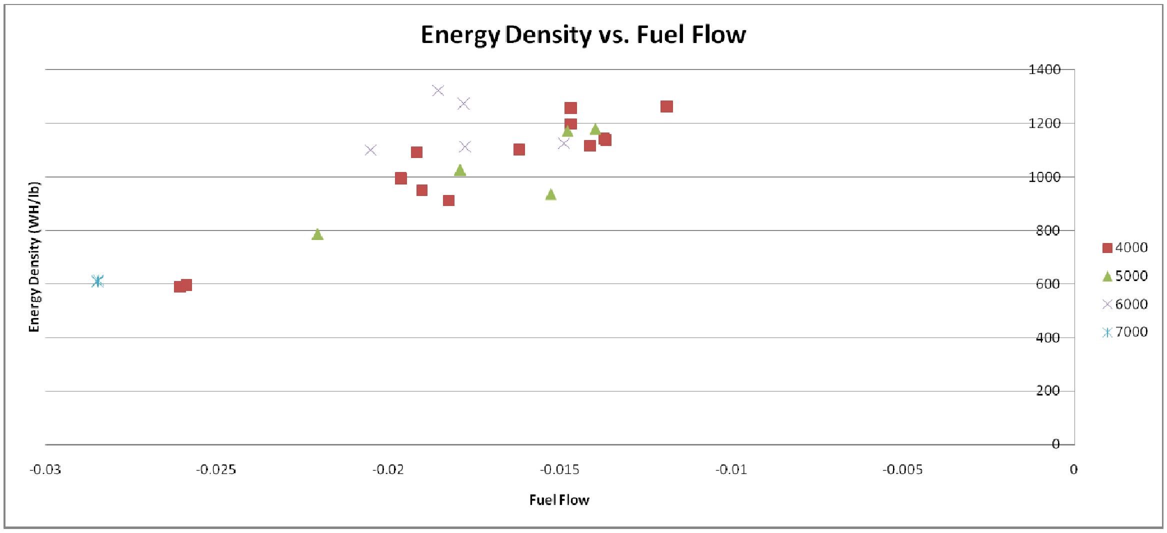

Figure 113 - Energy Density vs. Horsepower - OS 40 FS - Coleman Fuel - Spark Ignition

Typical energy density vs. horsepower relations are only visible for 4000 and 5000 RPM. At 6000 RPM, time dependent bearing friction reduced horsepower as the test was conducted, and as such the normal power to efficiency relation does not appear. While horsepower begins to drop with rich operation at 4000 RPM, the smallest fuel flow rate that the present carburetor would provide did not result in a lean enough run to expose the energy density peak. For testing such small flow rates, a real time flow rate sensor would be invaluable.

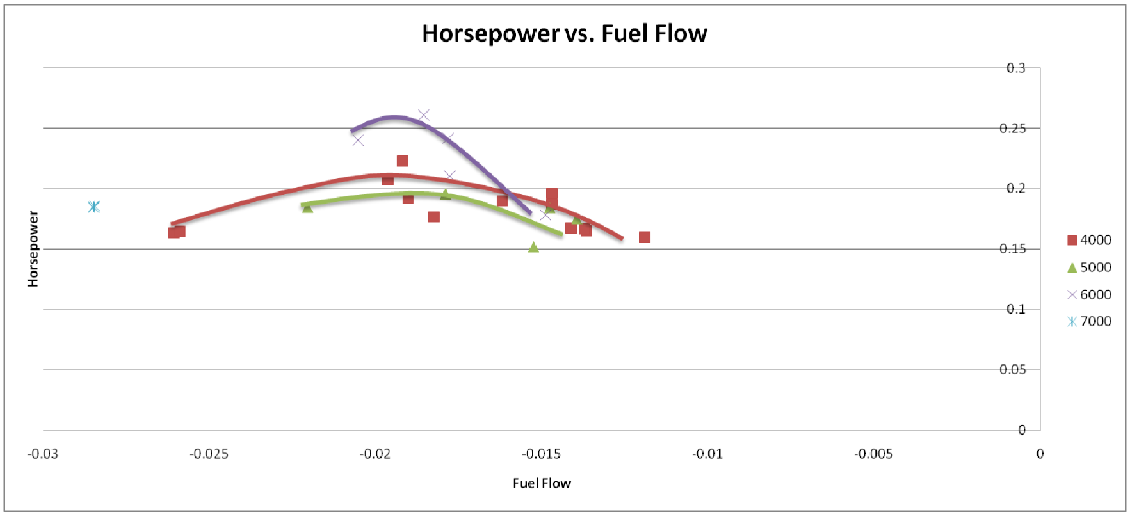

Figure 114 - Horsepower vs. Fuel Flow - OS 40 FS - Coleman Fuel - Spark Ignition

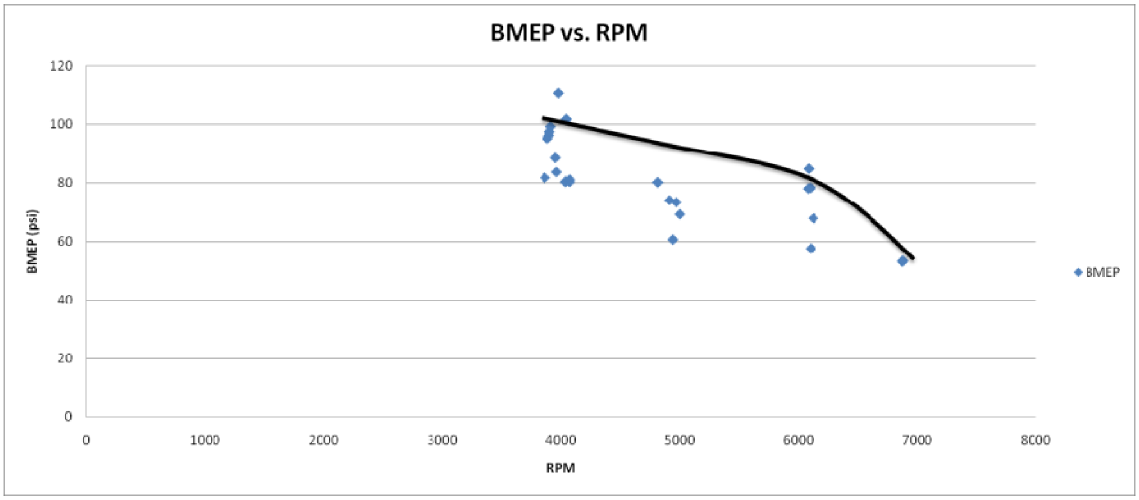

Figure 115 - BMEP vs. RPM - OS 40 FS - Coleman Fuel - Spark Ignition

Typical relations between maximum horsepower and fuel flow exist, and produce a surprisingly high BMEP compared to the OS 40 FS run on Glow fuel even with the significantly smaller carburetor intake. It is uncertain if BMEP is decreasing with RPM due to increased pumping losses from the small throat, or increased frictional losses from the failing bearings.

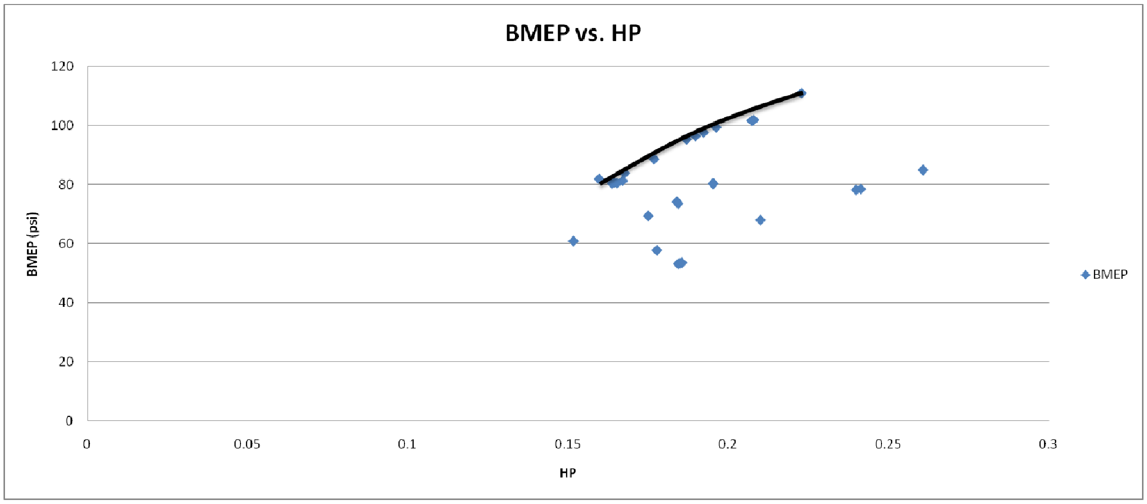

Figure 116 - BMEP vs. HP - OS 40 FS - Coleman Fuel - Spark Ignition

The Death of an Engine

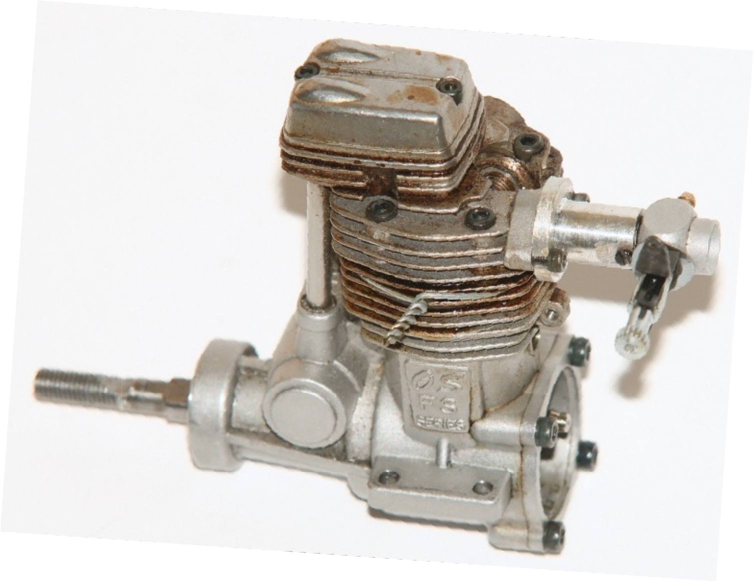

Initially, repeatability data was being taken on a modified OS 40 four stroke engine with ignition system set to 30 degrees before top dead center running pure Coleman fuel. This engine achieved very high energy densities, and proved the theory proposed that an internal combustion engine could produce three times the energy density of fuels cells. The first two data runs produced points that were quite similar to one another, except that the longer the engine was run, the lower the horsepower output, and lower the energy density went. On the third test, the beginning few points corresponded with the second run, but each of the final three data points produced lower power, and became less efficient. Shortly after the final data point of the third run, the engine died after the bearings had frozen from becoming too hot. The engine could not be turned at all immediately after the test. Thirty minutes later, the bearings had cooled enough to allow the engine to spin again, but tests on that engine were concluded, and the lower temperature glow fuel repeatability tests begun. The data taken on the modified OS 40 engine is particularly interesting when viewed in reference to time, as one can easily see the engine's mechanical efficiency decreasing due to heat damage of the main bearing. Arrows in the data below show the order in which points were taken.

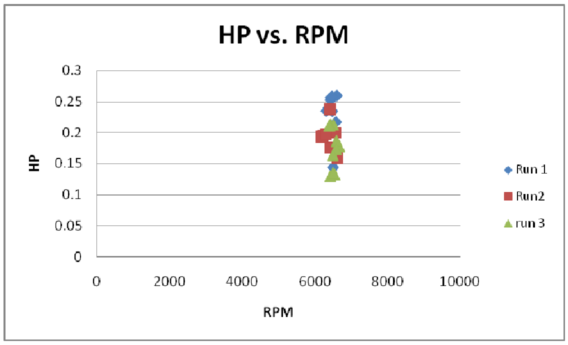

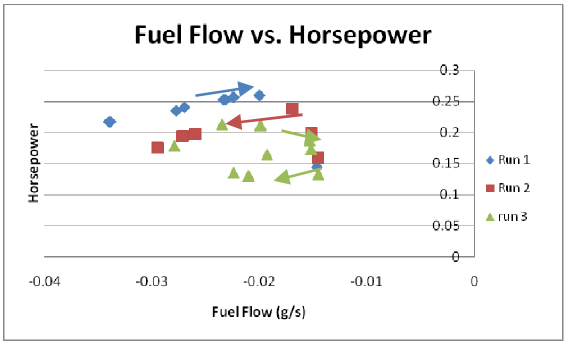

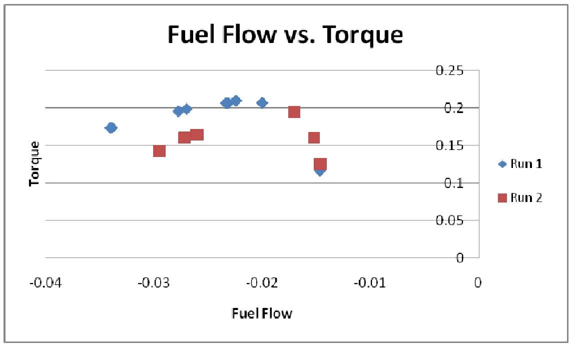

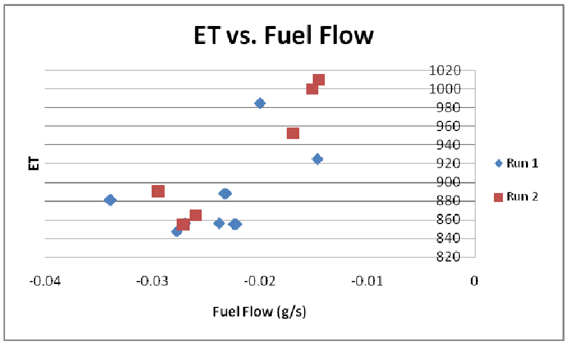

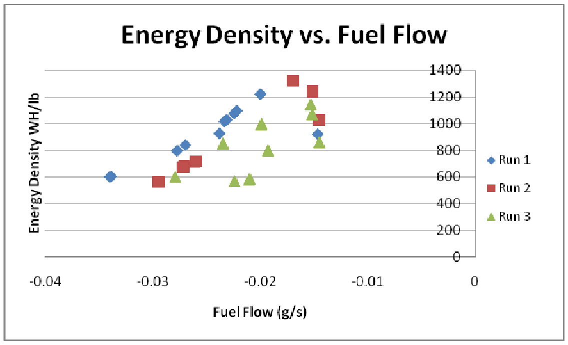

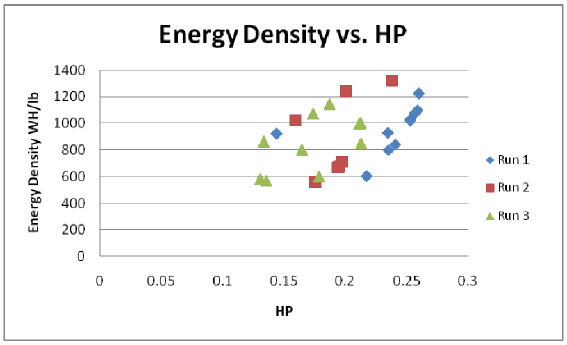

Modified OS 40 FS

After using a stock engine for a considerable amount of the dynamometers test runs, time was devoted to modifying the OS 40 enough to let it run on Coleman fuel. Coleman fuel is primarily naphtha which is a very long chain hydrocarbon, a natural lubricant, and has a very high energy density. The engine in its stock form would not run reliably on Naphtha, as the required flow rate was too low for the stock glow fuel carburetor to meter properly. A brass fuel orifice was drilled into the side of the stock engine carburetor, and although the orifice size was considerably smaller than the glow fuel Carburetor's the mixture was still too rich and the engine would not run smoothly. Finally a carburetor from a 0.01 cubic inch motor was used, and with careful adjustment of the very tightly tapered needle valve the engine sprang to life. Initially, the engine would not run lower than 4000 RPM, the mixture would lean out uncontrollably, and the cycle would shut down. The problem was traced to slop in the carburetor so small one could barely feel the movement at all. With the engine running, if the carb needle was pulled outward, the engine would idle beautifully down to 3000 RPM. If one did not apply outward pressure on the needle valve, the engine died immediately. After placing a wave washer to hold the needle valve out, engine testing resumed on the high efficiency engine. Initial tests showed the engine to reach energy densities up to 1500 WH/lb, confirming the initial calculations on the maximum energy density of small engines. Further efficiency increases can undoubtedly be achieved with changes to decrease intake losses, increase mechanical efficiency, and modifying the engine to tolerate the much higher operating temperatures.

Dual Mode Gas - Electric Engine

The dynamometer was specifically designed to facilitate hybrid engine research, where an electric motor would be used to govern the power output to the propeller. Under launch loads, the electric motor would provide additional torque to supplement power to the engine and create greater thrust than the engine alone could provide. Additionally the motor would enable the aircraft to temporarily shut its engine down, glide using available atmospheric energy, and then restart whenever the ground becomes threatening. Three basic drive methods are available to the motor/generator: permanent coupling, one way bearing coupling, and clutched connection. The simplest solution would be a permanent shaft coupling. This would allow the engine to be restarted at will, and power could be taken off the engine shaft to charge the onboard battery and run onboard systems. A one way bearing in the coupling would either allow the motor to add or subtract power, but never both. A bearing configured to drive the engine would allow in flight restart, and supplemental power from the battery, but would be incapable of charging the onboard battery. A bearing configured to charge the onboard battery would never be able to start the engine, but would allow precise control of engine RPM. The best method of engine control would be a clutched motor connection mechanism. This would allow the motor to add or subtract torque, restart the engine, or power the aircraft solely on its own power. A bi-stable centripetal clutch as shown below would allow the motor to be selectively engaged or disengaged from the engine.

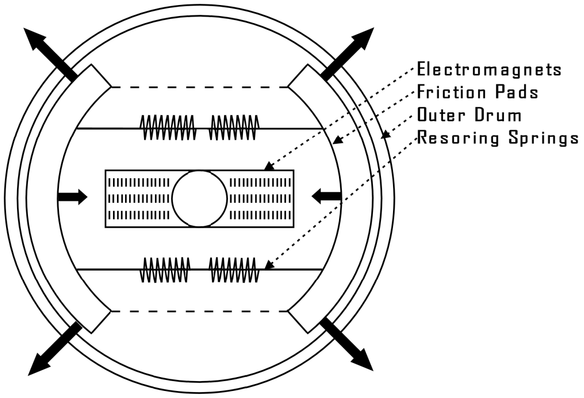

Figure 117 - Conceptual Bi-Stable Electromagnetic Clutch.

The inner assembly of the above clutch would rotate with the electric motor, and the outer drum would be permanently mounted on the engine shaft. To start the engine, the motor would simply spin up with the electromagnets disengaged, allowing the outer pads to overpower the springs and contact the drum as in a typical centripetal clutch. To disengage the motor from the engine, the electromagnets would be temporarily energized to draw the pads away from the drum. The motor would then brake itself to a stop, at which point the springs would exert enough force to counteract gravity and hold the pads out of contact with the drum. Variations on this design would include mechanical torque transfer instead of pure frictional, and alternative methods of forcing the friction pads out of contact with the outer drum. The electromagnets could be moved to the outside, and permanent magnets placed on the friction pads. This would simplify wiring and construction.

The capability to restart an engine would be the main benefit of a dual mode system. While one could power an aircraft solely from stored energy from engine operation. The specific power of batteries is less than that of engines, making such a system heavier than a simply engine alone. For bursts of high power batteries can greatly overextend themselves, making the large torque's of re-starting, or temporary takeoff loads a preferable alternative to sustained electric operation. To further decrease the torque and associated weight required to restart an engine, one could hold the exhaust valve of the engine open with a solenoid until the engine reaches an appropriate starting RPM. This would eliminate pumping losses while trying to start an engine, and only the frictional losses would have to be counteracted by the electric motor.

For extreme low power aircraft, a pulsed power flight profile may result in longer runtimes. Testing has shown the efficiency of engines to decrease as their RPM and output power drops. This means that for aircraft that only require a mean of 20-40 watts to fly, that the engine would be forced into non-optimal conditions if it ran at all. A controller that would oscillate an aircraft around its set altitude could keep the mean power consumption of the airplane at its optimal point, and simultaneously let the engine operate at its maximum energy density horsepower. By starting the engine and running at maximum energy density to climb rapidly without gaining excessive airspeed, then shutting it off and gliding until the restart altitude, one has effectively applied pulse width modulation principles to aircraft. The airplane would maintain its maximum L/D or power factor depending on its purpose, while its engine provides intermittent power at its optimal operating condition. While some losses would occur from constantly stopping and restarting the engine, it would most likely provide a higher energy density than throttling or scaling the engine down even more. This flight profile is only possible with restart, and would be key to providing the very long flight times predicted in the aircraft performance section of this paper.

Dual Mode Power and Energy Density Tradeoff

Any dual mode system is inherently a compromise between two opposing energy systems, but the decrease in cruise endurance to accommodate a dual mode silent running propulsion system is very severe. The chart below uses test data from the modified OS 40 FS given in this document. The engine was shown to produce 230 watts at an energy density of 1320 WH/lb. Lithium polymer batteries in combination with a 0.45 lb motor will provide the remaining 780 watts of power when both modes are engaged. This study only considers shaft energy density and power, which results in the electric motor receiving a further handicap for the purposes of accurate comparisons. An 80 percent motor efficiency, and 95 percent speed controller efficiency was assumed which reduced the energy density of lithium polymer batteries to 57 WH/lb. For a ten pound energy system, the carpet plot below shows that moving from a dual mode system for takeoff and restart only, to a system that could provide thirty minutes of full power cuts the endurance of the vehicle to a third of its original capability. One can easily see that the slope of all dual mode curves roughly follows that of the 100% engine energy curve. This is because the relative energy density of lithium polymer batteries after motor and speed controller losses is so low that one can simply think of the amount of battery weight necessary to provide the supplemental power as being lost to the total energy storage of the system.

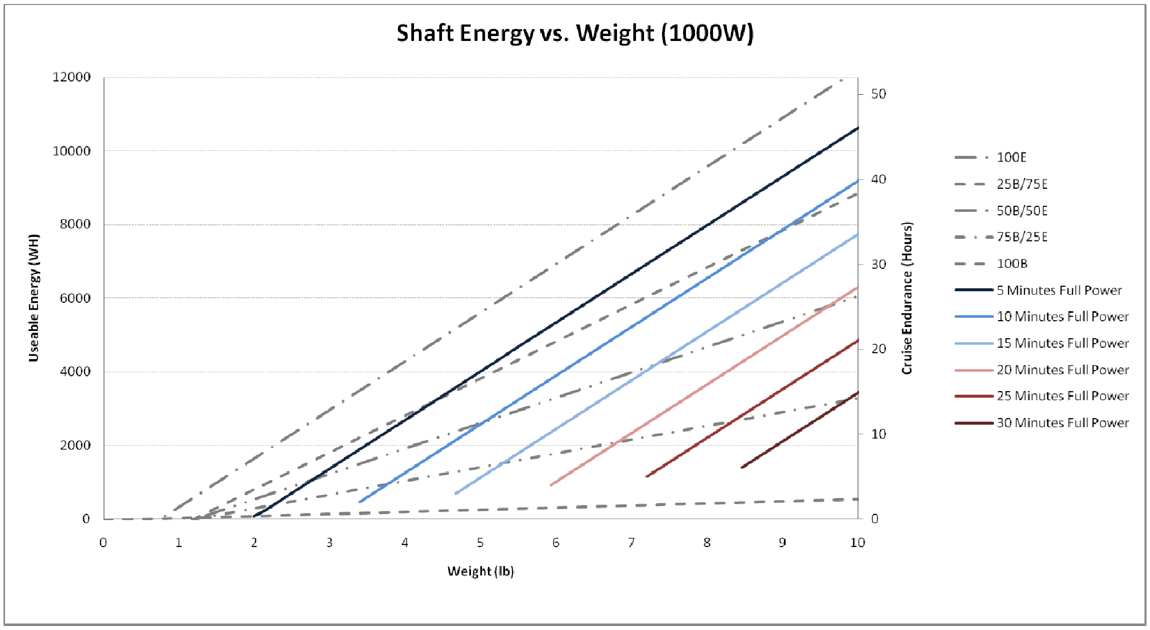

Figure 118 - Shaft Energy vs. Weight (1000W)

The above carpet plot shows the advantage of simply using a larger engine to provide periods of high power. This forces the engine to cruise at low throttle settings which through testing has been shown to significantly reduce efficiency. This makes the ideal small aircraft engine a variable displacement multi-cylinder, or a selective combustion single cylinder engine. Essentially any engine that can reduce its output power without a great loss in efficiency would be preferable to a hybrid system for providing long periods of high power. If takeoff power is one's only concern, the difference is not so strong, and selection would become application specific.

CHAPTER V

FUTURE IMPROVEMENTS

Electronic Valves

Electronically operated valves would provide some efficiency increase through the reduction of frictional mean effective pressure (FMEP), but would be most beneficial as a method of controlling engine efficiency, output power, and noise. Engine efficiency could be increased from the reduction in FMEP as well as better engine cycle control. Being able to reduce engine output power without having to introduce pumping losses to lower the manifold pressure would also improve partial throttle engine efficiency. Perhaps the most intriguing benefit of an EVIC engine would be its ability to selectively fire the cylinder to maintain RPM. This would allow the engine to provide very low power levels during cruise without suffering a large efficiency loss. Additionally, holding the exhaust valve open during starting eliminates pumping losses which greatly reduces the required torque to start an engine. To reduce noise, one could hold the intake valve open for a portion of the compression stroke to effectively lower the compression ratio, and in turn allow volume for complete expansion of the hot combustion products to atmospheric pressure. This complete expansion cycle would reduce the magnitude of the square wave exhaust note, and also increase efficiency by extracting all useable energy from the hot gas.

Figure 119 - Dave Bowes' Electronic Valve Internal Combustion Engine

Electronic Fuel Flow Control

Testing has proven that simply supplying the proper amount of fuel throughout the engine's operating range is the easiest way to ensure proper operation. Additionally, the in flight modification of fuel maps from an efficiency driven distribution, to a maximum power distribution would allow for optimal operation in each mode. Ideally, one could control fuel based off an oxygen sensor in the exhaust to ensure complete combustion while not running the engine too lean. The most direct method of electronically metering fuel flow would be to have a servo controlled needle valve connected to a microcontroller that would adjust the valve setting based on engine RPM and air temperature. The most advanced method would ultrasonically atomize fuel in a closed loop with oxygen, RPM, and detonation sensors. This active loop would be capable of automatically adjusting fuel flow for changes in atmospheric conditions including density decreases with altitude. There is no greater improvement to small engines than properly metering their fuel.

Lean Cycle Operation

As the operating fluid's properties in an engine more closely approximates that of 100% air, the theoretical cycle efficiency increases as described in the chart below (Taylor).

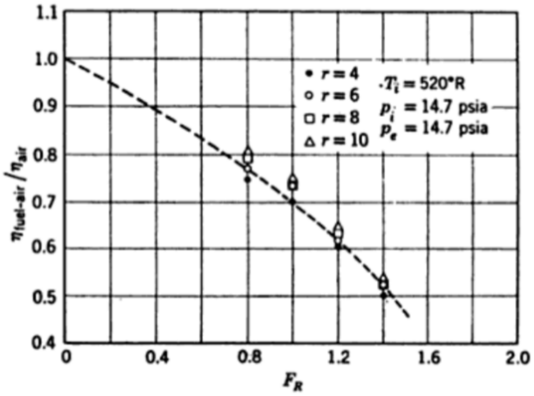

Figure 120 - Increse in theoretical efficiency vs. Fuel to Air Ratio (Taylor)

Maintaining combustion while running the engine very lean becomes the major difficulty in reaching the higher efficiency levels. Quenching of the flame front due to increase surface area of small engines, and lower heat input per cycle is one of the main limitations of lower fuel to air ratio's. Additionally, venturi type carburetors already have difficulty in delivering such small fuel flow rates. Such simple carburetors have a distinct lower flow rate limit where their fuel stream becomes unsteady, and poorly atomized. Multiple spark plugs, ultrasonic atomization, and increased cylinder turbulence would all help the engine maintain combustion in very lean situations.

Air Flow Sensor

Presently the dynamometer is incapable of providing true air to fuel ratio information. One could assume that airflow corresponds to swept volume, but understanding the true scavenging ratio of an engine as well as any speed dependent flow losses would be valuable information. Fitting an intake plenum to the test engine with a TSI 40211 air mass flow sensor as seen in the Menon dynamometer would allow true scavenging and air to fuel ratio measurements.

Multiple Thermocouple Amplifier

Presently, a single channel thermocouple amplifier and cold junction compensator is used to take exhaust measurements. The addition of a multichannel thermocouple reading device would allow lab view to automatically log various temperatures across the engine. This data will be invaluable for any design work to increase the temperature tolerance of the engine.

Bi Directional Load Cell Protection

A system to transfer both tension and compression to the load cell, while also insuring the maximum force stays below 250 lbs under any circumstances would further decrease systematic error due to the current asymmetric spring. Additionally a high modulus connector in addition to lowering the rotational inertia would move the resonant frequency out of the operational range of the dynamometer.

RPM hold controller

Currently, a large portion of data scatter is due to the operators inability to hold RPM constant while monitoring all other aspects of the dynamometer. As described previously, a PI controller was successfully implemented at low rates, but true worry free control of engine RPM will only be capable with a faster updating loop. A microcontroller based system was coded and put together, but never applied to the dynamometer. Application of said system would be fast and reduce the strain on the dynamometer operator.

Instantaneous Fuel Flow Sensor

Presently the fuel flow sensor is the last measurement to converge. The mass based system's uncertainty is proportional to the amount of fuel burned, and for very low fuel flow rates this measurement can take up to five minutes before it is sufficiently converged. The addition of an accurate instantaneous fuel flow measurement gauge would expedite efficiency tests, and also help to statistically reduce fuel flow uncertainty.

High Temperature Materials

When the OS 40 FS was modified to operate on Naphtha fuel exhaust temperatures reached 1020 degrees at 6500 RPM. The melting point of aluminum is 1200 degrees F, less than 200 degrees greater than the hottest part of the engine. Additionally that modified engine eventually died from the bearings overheating. Ceramic bearings would tolerate higher temperatures, but still would benefit from a dedicated oil system. As theoretical engine efficiency relies on large temperature differentials, a high temperature cylinder head and sleeve would help to increase overall efficiency and reduce wear. One must be careful to thermally insulate the intake manifold and carburetor from the hot area of the engine so that the incoming air charge is not preheated too severely. High temperature steel's should be investigated for the hot regions of the engine.

Round Calibration Plate

The deflection of the torque arm during calibration introduces some systematic error in the final measurement. A round calibration disk would ensure that as the torque arm deflected, the measurement distance remained the same. Additionally, the uncertainty involved with finding the center of the torque shaft would be reduced by precision cutting the outer surface.

Deep Groove Ball Bearings

Needle bearings were selected to support the torque shaft of the dynamometer because of their naturally low rolling resistance. However, poor machining has resulted in a significant amount of slop in the restraint of the torque shaft. Also the needle bearings do not constrain the torque shaft axially, which requires additional points of contact that add further systematic error. Using deep groove ball bearings with an inner race press fit against the 2" torque shaft would eliminate the need for axial restraint, while reducing overall systematic error.

Controllable Spark Advance

When configuring an engine, setting the spark advance properly is essential to maximizing efficiency and BMEP. Currently if one wishes to adjust the ignition angle, the flywheel must be loosened from the engine output shaft and readjusted. This is a tedious and time consuming task. A simple electronic circuit to apply a delay between the top dead center hall effect trigger, and the signal to the ignition system could be used to vary ignition angle while the engine is running. This would allow the user to create various plots vs. ignition angle.

Rectification

An essential component of any hybrid system will be efficient rectification of the generated power. Brushed DC motors can be used to automatically rectify the power, but are quite inefficient, and wear with time. Brushless motors are preferred, but will require rectification of their three phase power output. If one is seeking an extremely low KV generator, single pole motor options exist that would theoretically reduce the mass of the motor by 3 times when compared to a three phase brushless motor of equivalent KV. The efficient rectification of single phase power is somewhat more difficult.

Three phase diode based rectifiers are simple to use, but relatively inefficient. If the power passing through a diode based rectifier is assumed to be reduced by 1.2 volts, the efficiency curve at 100% duty cycle is as follows:

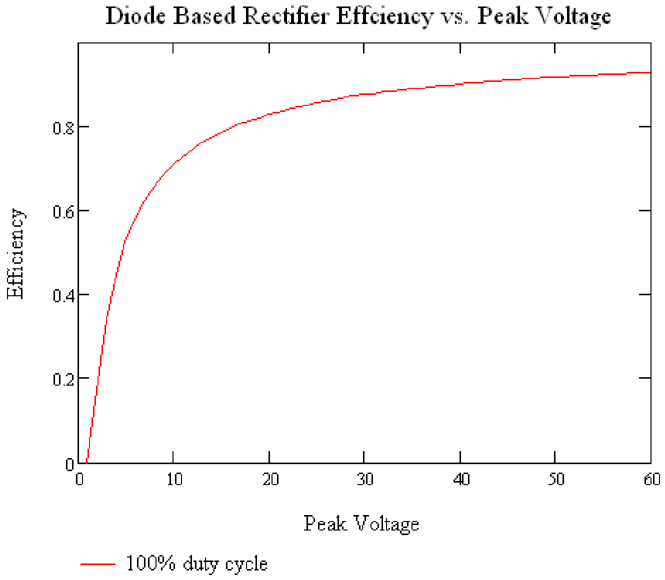

Figure 121 - Efficiency of Diode Based Rectifier at 100% Duty Cycle vs. Peak Voltage

The higher performance, but more complicated alternative to diode based rectification, is triggered MOSFET rectification. MOSFET's have very low resistances and therefore can operate with high efficiency even at high currents. They do not automatically restrict reverse current flow, and as such must be actively triggered with logic level inputs. The easiest way to achieve this would be to utilize infinite gain op amps in comparator mode against ground. When the voltage from the motor is higher than ground, the appropriate MOSFET will be triggered to allow the voltage to pass. When the opposite condition is true, a separate comparator will trigger a MOSFET to invert the voltage connection and therefore rectify the signal. Additionally, a low power diode based rectifier could be used in conjunction with a high value capacitor to power the op-amp logic circuit. This way the active rectifier can be self starting even in circumstances where the main battery is dead.

The efficiency of a high power 24 milliohm MOSFET was calculated vs. load resistance giving the following results. One can see that a MOSFET based rectifier's efficiency is virtually independent of the peak voltage supplied, while a Diode based rectifier is heavily dependent on peak supply voltage. Also, the coupling of a MOSFET with a low resistance load will result in much higher circuit currents. Since the power losses of a MOSFET are exponential, while the power losses of Diodes are linear, for a given current the diode option will again become more efficient.

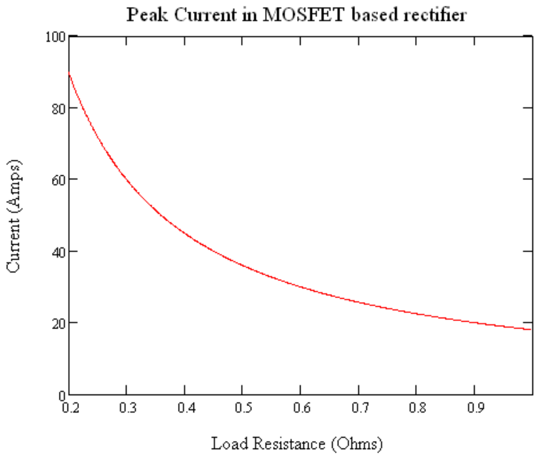

Figure 122 - Current in MOSFET vs. Load Resistance

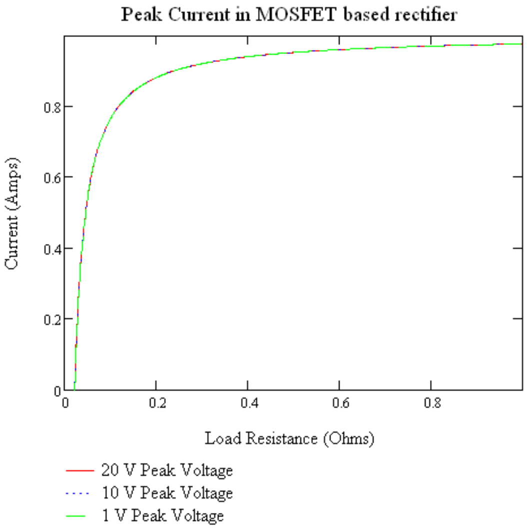

Figure 123 - Efficiency of MOSFET vs. Load Resistance

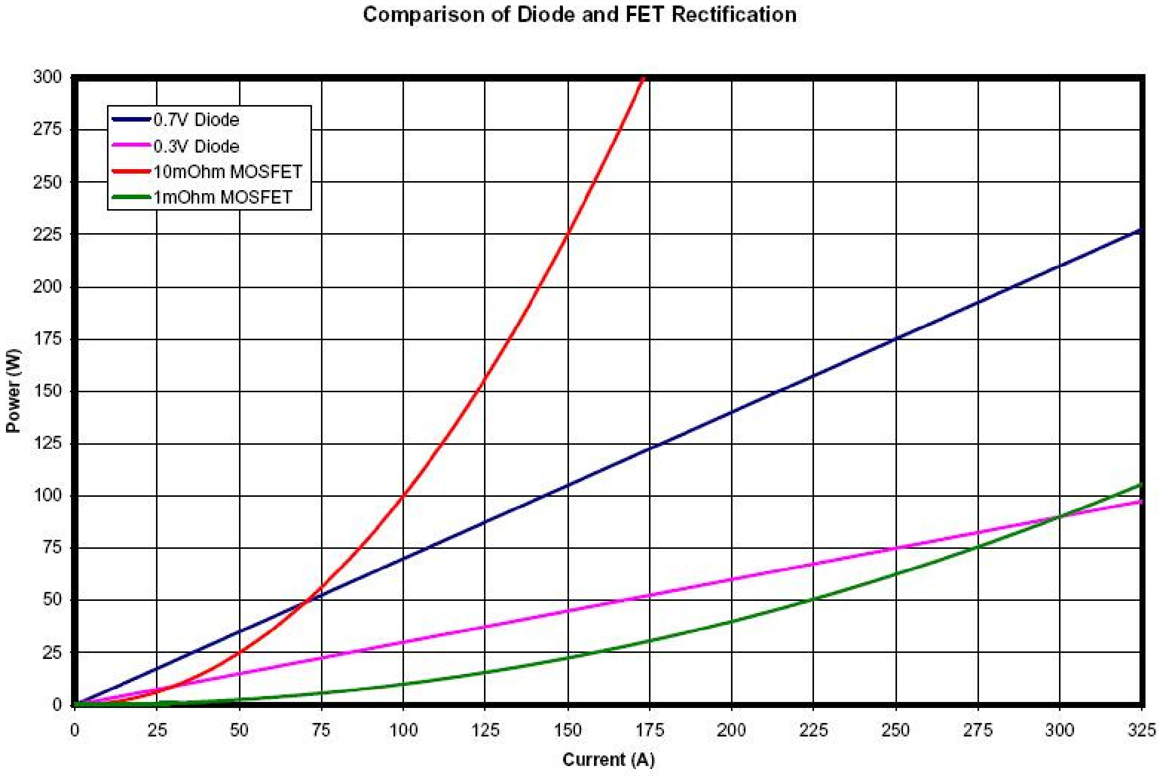

Figure 124 - Comparison of Dissipated Power in Diode vs. MOSFET Devices. (Hanlon, Jon)

APPENDICES

Aircraft Performance

The true purpose of all the dynamometer work, and all the energy density study work is to increase the maximum performance of various aircraft classes. The benefits of high efficiency combustion engines have been realized since the second world war in large aircraft, and have continued into increasingly smaller scales ever since. The following sections present a brief conceptual example of the effect a miniature high efficiency engine would have on various UAV classes. All calculations are performed with a modified AG12 airfoil created by Mark Drela, and modified for higher lift coefficients by the Author. This airfoil is by no means optimized for the duration and range task, but provides a general high performance, low Reynolds number airfoil. An automatic CL and Reynolds number interpolation routine was used to determine Cd.

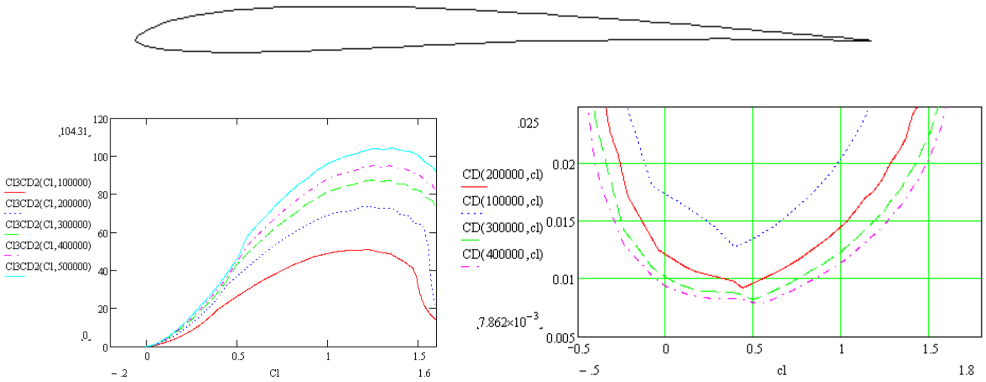

Figure 125 - Unmodified AG12 by Mark Drela

Ten Pound Man Portable (Optimized 20% Nitro Methane Engine)

Assumptions:

- 350 WH/lb Energy Density [OS 40 FS on Glow Fuel]
- Standard Atmosphere
- 3 lb payload
- 0.5 lb propulsion allowance (propeller, gearbox)
- 70% Efficient Propeller
- 20 Watt Autopilot and Payload Allowance
- 1.25 lb Buy in Weight
- 1000 ft ASL Cruise
- 32 in^2frontal area with 0.3 CD
- AR<12
- b<10 ft
- Stall < 30 fps
- Wing Weight Model = 0.35*S with an additional 1 lb for Fuselage Weight

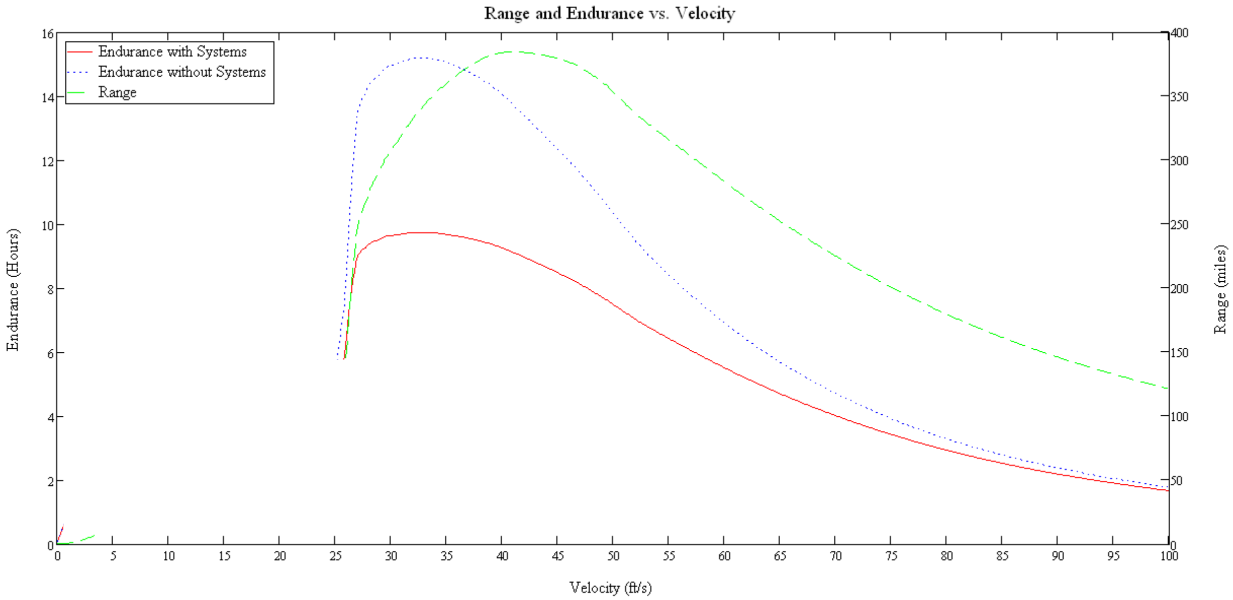

- 9.5 Hour Endurance
- 375 Mile Range
- 9.6 ft Wingspan
- 7.7 $\text{ft}^2$of wing
- 32 ft/s optimal cruising speed
- 1.55 lbs of fuel
- 10 lb takeoff weight

For the sake of being conservative, the change in weight due to fuel burn is not included in this prediction. Actual flight time and range will be greater than that predicted.

Ten Pound Man Portable (battery only)

Assumptions:

- 160 WH/lb Energy Density [SION published data]
- Standard Atmosphere
- 3 lb payload
- 0.5 lb propulsion allowance (propeller, gearbox)
- 50% Efficient transmission of energy between battery and flow
- 20 Watt Autopilot and Payload Allowance
- 0 lb Buy in Weight
- 1000 ft ASL Cruise
- 32 in^2frontal area with 0.3 CD
- AR<12
- b<10 ft
- Stall < 30 fps
- Wing Weight Model = 0.35*S with an additional 1 lb for Fuselage Weight

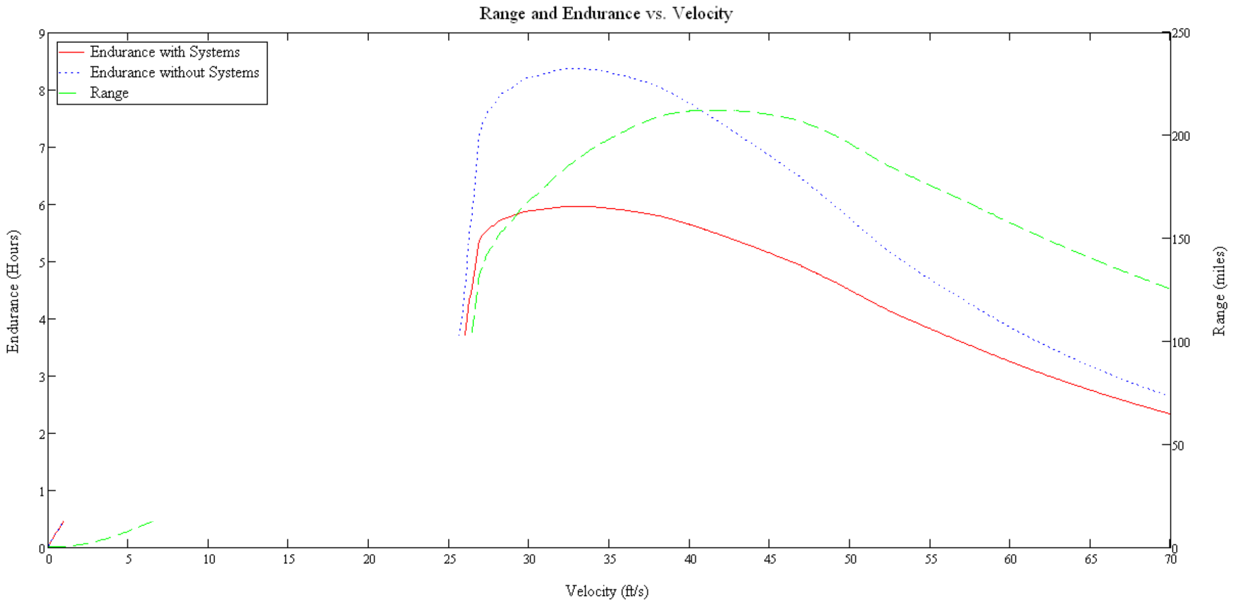

- 6 Hour Endurance
- 212 Mile Range
- 9.8 ft Wingspan
- 8 $ft^2$of wing
- 32.75 ft/s optimal cruising speed
- 2.6 lbs of fuel
- 10 lb takeoff weight

Although the SION battery based aircraft stores a similar amount of fuel to the RC engine airplane, the reduced propulsive efficiency from the motor and speed controller reduce its endurance by 3.5 hours.

Ten Pound Man Portable (Optimized Gas Engine)

Assumptions:

- 1400 WH/lb Energy Density [Conservative Naphtha test data]
- Standard Atmosphere
- 3 lb payload
- 0.5 lb propulsion allowance (propeller, gearbox)
- 70% Efficient Propeller
- 20 Watt Autopilot and Payload Allowance
- 1.25 lb Buy in Weight
- 1000 ft ASL Cruise
- 32 in^2 frontal area with 0.3 CD
- AR<12
- b<10 ft
- Stall < 30 fps
- Wing Weight Model = 0.35*S with an additional 1 lb for Fuselage Weight

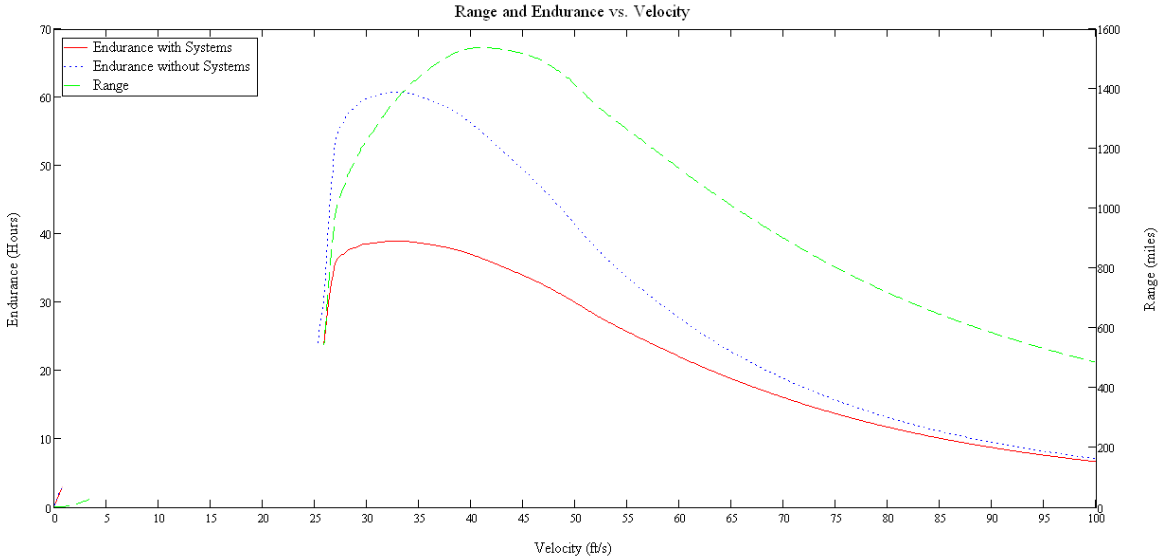

- 39 Hour Endurance
- 1500 Mile Range
- 9.6 ft Wingspan
- 7.7 ft^2 of wing
- 32 ft/s optimal cruising speed
- 1.55 lbs of fuel
- 10 lb takeoff weight

For the sake of being conservative, the change in weight due to fuel burn is not included in this prediction. Actual flight time and range will be greater than that predicted.

F5 FAI World Record Class [Dragonfly Optimization Calibration Point]

Assumptions:

- 70 WH/lb Energy Density [Lithium Polymer]
- Standard Atmosphere
- 0 lb payload
- 0.5 lb propulsion allowance (propeller, gearbox)
- 50% Efficient Propulsion (battery to flow)
- 10 Watt Autopilot and Payload Allowance
- 0 lb Buy in Weight
- 1000 ft ASL Cruise
- 9 in^{2}frontal area with 0.1 CD
- AR<21
- b<20 ft
- Stall < 50 fps
- Wing Weight Model = 0.2*S with an additional 1 lb for Fuselage Weight

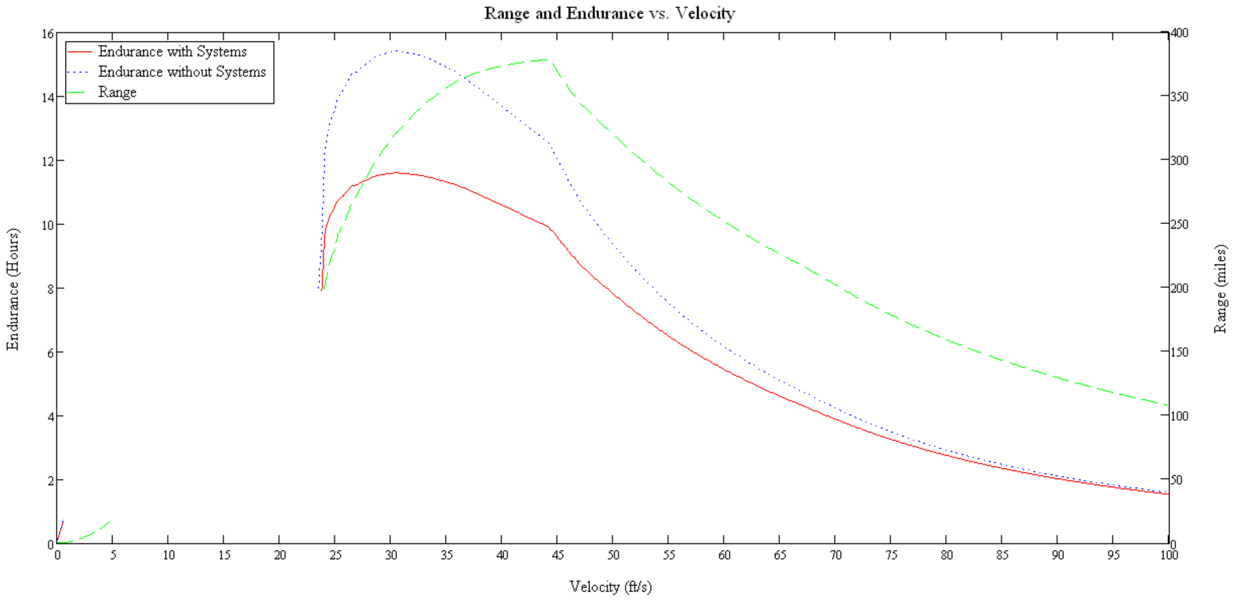

- 11.6 Hour Endurance
- 375 Mile Range
- 14 ft Wingspan
- 9.8 ft^{2}of wing
- 31 ft/s optimal cruising speed
- 6.9 lbs of battery
- 11.02 lb takeoff weight

Actual Dragonfly Specifications:

- 12.25 Hour Endurance
- 14 Ft Span
- 10 ft^{2}of wing
- 20-25 mph cruise
- 6.7 lb of battery
- 11.02 takeoff weight

F5 FAI World Record Class [Endurance Optimization]

Assumptions:

- 1400 WH/lb Energy Density [Conservative Naphtha test data]
- Standard Atmosphere
- 0 lb payload
- 0.5 lb propulsion allowance (propeller, gearbox)
- 70% Efficient Propeller
- 10 Watt Autopilot and Payload Allowance
- 1.25 lb Buy in Weight
- 1000 ft ASL Cruise
- 9 in^2frontal area with 0.1 CD
- AR<25
- b<20 ft
- Stall < 50 fps
- Wing Weight Model = 0.2*S with an additional 1 lb for Fuselage Weight

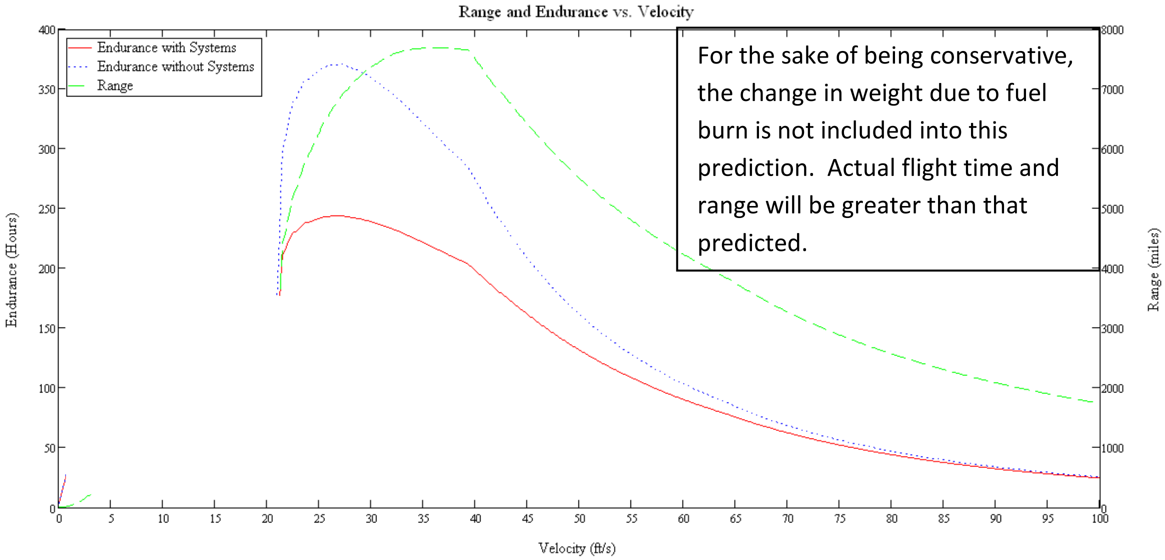

For the sake of being conservative, the change in weight due to fuel burn is not included into this prediction. Actual flight time and range will be greater that predicted.

- 243 Hour Endurance
- 7600 Mile Range
- 18 ft Wingspan
- 13.3$\text{ft}^2$of wing
- 27 ft/s optimal cruising speed
- 5.1 lbs of fuel
- 11.02 lb takeoff weight

Performance model is very sensitive to slight variations in required power for such long endurance aircraft. Predicted power consumption of 30 watts is on the lower end of believability even though engines avoid motor and speed controller losses. Even half the performance would still best the current records of 33.5 hours.

F5 FAI World Record Class [Range Optimization]

Assumptions:

- 1400 WH/lb Energy Density [Conservative Naphtha test data]
- Standard Atmosphere
- 0 lb payload
- 0.5 lb propulsion allowance (propeller, gearbox)
- 70% Efficient Propeller
- 10 Watt Autopilot Allowance
- 1.25 lb Buy in Weight
- 10,000 ft ASL Cruise
- 9 in^2frontal area with 0.1 CD
- AR<25
- b<20 ft
- Stall < 50 fps
- Wing Weight Model = 0.3*S with an additional 1 lb for Fuselage Weight

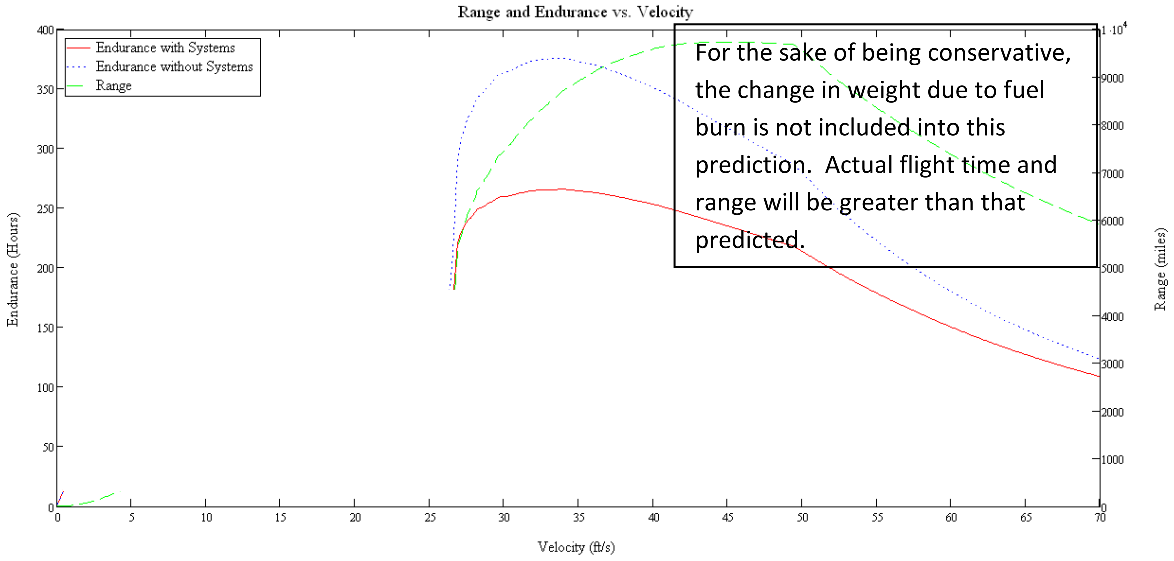

For the sake of being conservative, the change in weight due to fuel burn is not included into this prediction. Actual flight time and range will be greater than that predicted.

- 230 Hour Endurance
- 9700 Mile Range
- 14.8 ft Wingspan
- 8.9 $ft^2$of wing
- 45 ft/s optimal cruising speed
- 6.5 lbs of fuel
- 11.02 lb takeoff weight

Unlimited Class [Range Optimization]

Assumptions:

- 1400 WH/lb Energy Density [Conservative Naphtha test data]
- Standard Atmosphere
- 0 lb payload
- 0.5 lb propulsion allowance (propeller, gearbox)
- 70% Efficient Propeller
- 10 Watt Autopilot and Payload Allowance
- 1.25 lb Buy in Weight
- 1000 ft ASL Cruise
- 9 in^2frontal area with 0.1 CD
- AR<25
- b<100 ft
- Stall < 100 fps
- Wing Weight Model = 0.3*S with an additional 1 lb for Fuselage Weight

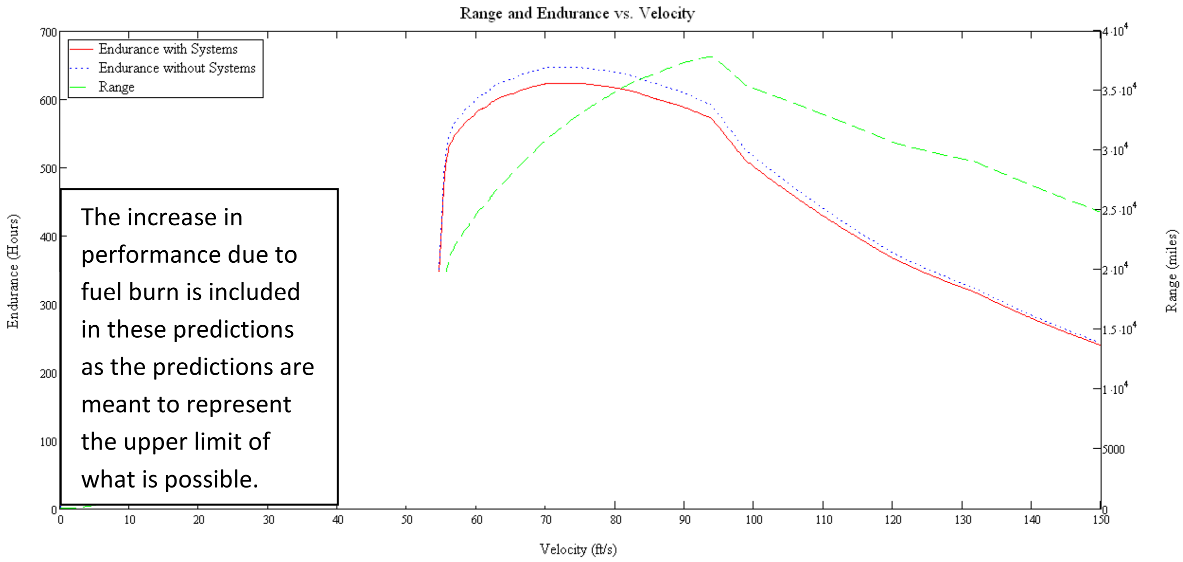

The increase in performance due to fuel burn is included in these predictions as the predictions are meant to represent the upper limit of what is possible.

- 320 Hour Endurance
- 37,800 Mile Range
- 20.7 ft Wingspan
- 17.1 $ft^2$of wing
- 90 ft/s optimal cruising speed
- 63.3 lbs of fuel
- 73.6 lb takeoff weight

Performance model is very sensitive to slight variations in required power for such long endurance aircraft. Predicted power consumption has an extreme effect on performance. 37,800 miles is nearly 1.5 times longer than the current absolute aviation world record of 25,700 miles set by Steve Fossett.

Unlimited Class [Endurance Optimization]

Assumptions:

- 1400 WH/lb Energy Density [Conservative Naphtha test data]
- Standard Atmosphere
- 0 lb payload
- 0.5 lb propulsion allowance (propeller, gearbox)
- 70% Efficient Propeller
- 10 Watt Autopilot and Payload Allowance
- 1.25 lb Buy in Weight
- 1000 ft ASL Cruise
- 9 in^2frontal area with 0.1 CD
- AR<25
- b<100 ft
- Stall < 100 fps
- Wing Weight Model = 0.3*S with an additional 1 lb for Fuselage Weight

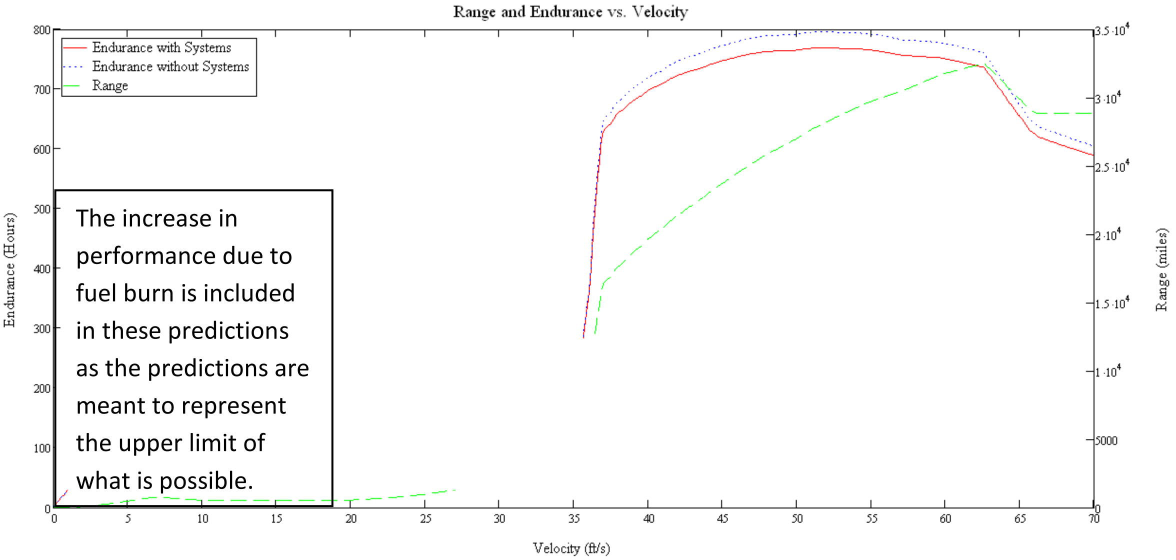

The increase in performance due to fuel burn is included in these predictions as the predictions are meant to represent the upper limit of what is possible.

- 768 Hour Endurance
- 33629 Mile Range
- 40.5 ft Wingspan
- 65.5 $ft^2$of wing
- 51.4 ft/s optimal cruising speed
- 100.5 lbs of fuel
- 125.4 lb takeoff weight

The performance model is very sensitive to slight variations in required power for such long endurance aircraft. Predicted power consumption has extreme effects on range and endurance. 768 hours (32 days) would make this the longest flying aircraft ever in any class, beating Dick Rutan and Jeana Yeager's record by 552 hours. Even if power consumption is twice as high as predicted, it would still become the absolute record.

GLOW FUEL FLOW RATE ROTAMETER CHART

Value	Left	Right	Value	Left	Right	Value	Left	Right
1	0.008	-0.006	51	0.022	-0.027	101	0.036	-0.070
2	0.008	-0.006	52	0.022	-0.027	102	0.036	-0.071
3	0.009	-0.006	53	0.022	-0.028	103	0.036	-0.073
4	0.009	-0.007	54	0.023	-0.029	104	0.036	-0.074
5	0.009	-0.007	55	0.023	-0.029	105	0.037	-0.075
6	0.010	-0.007	56	0.023	-0.030	106	0.037	-0.076
7	0.010	-0.007	57	0.024	-0.031	107	0.037	-0.077
8	0.010	-0.008	58	0.024	-0.032	108	0.037	-0.078
9	0.010	-0.008	59	0.024	-0.032	109	0.038	-0.079
10	0.011	-0.008	60	0.024	-0.033	110	0.038	-0.081
11	0.011	-0.008	61	0.025	-0.034	111	0.038	-0.082
12	0.011	-0.009	62	0.025	-0.034	112	0.039	-0.083
13	0.012	-0.009	63	0.025	-0.035	113	0.039	-0.084
14	0.012	-0.009	64	0.025	-0.036	114	0.039	-0.085
15	0.012	-0.010	65	0.026	-0.037	115	0.039	-0.087
16	0.012	-0.010	66	0.026	-0.037	116	0.040	-0.088
17	0.013	-0.010	67	0.026	-0.038	117	0.040	-0.089
18	0.013	-0.011	68	0.027	-0.039	118	0.040	-0.090
19	0.013	-0.011	69	0.027	-0.040	119	0.041	-0.092
20	0.013	-0.011	70	0.027	-0.041	120	0.041	-0.093
21	0.014	-0.012	71	0.027	-0.042	121	0.041	-0.094
22	0.014	-0.012	72	0.028	-0.042	122	0.041	-0.095
23	0.014	-0.012	73	0.028	-0.043	123	0.042	-0.097
24	0.015	-0.013	74	0.028	-0.044	124	0.042	-0.098
25	0.015	-0.013	75	0.028	-0.045	125	0.042	-0.099
26	0.015	-0.014	76	0.029	-0.046	126	0.042	-0.101
27	0.015	-0.014	77	0.029	-0.047	127	0.043	-0.102
28	0.016	-0.014	78	0.029	-0.048	128	0.043	-0.103
29	0.016	-0.015	79	0.030	-0.048	129	0.043	-0.105
30	0.016	-0.015	80	0.030	-0.049	130	0.044	-0.106
31	0.016	-0.016	81	0.030	-0.050	131	0.044	-0.107
32	0.017	-0.016	82	0.030	-0.051	132	0.044	-0.109
33	0.017	-0.017	83	0.031	-0.052	133	0.044	-0.110
34	0.017	-0.017	84	0.031	-0.053	134	0.045	-0.112
35	0.018	-0.018	85	0.031	-0.054	135	0.045	-0.113
36	0.018	-0.018	86	0.031	-0.055	136	0.045	-0.114
37	0.018	-0.019	87	0.032	-0.056	137	0.045	-0.116
38	0.018	-0.019	88	0.032	-0.057	138	0.046	-0.117
39	0.019	-0.020	89	0.032	-0.058	139	0.046	-0.119
40	0.019	-0.020	90	0.033	-0.059	140	0.046	-0.120
41	0.019	-0.021	91	0.033	-0.060	141	0.047	-0.122
42	0.019	-0.021	92	0.033	-0.061	142	0.047	-0.123
43	0.020	-0.022	93	0.033	-0.062	143	0.047	-0.125
44	0.020	-0.023	94	0.034	-0.063	144	0.047	-0.126
45	0.020	-0.023	95	0.034	-0.064	145	0.048	-0.128
46	0.021	-0.024	96	0.034	-0.065	146	0.048	-0.129
47	0.021	-0.024	97	0.034	-0.066	147	0.048	-0.131
48	0.021	-0.025	98	0.035	-0.067	148	0.048	-0.132
49	0.021	-0.026	99	0.035	-0.068	149	0.049	-0.134
50	0.022	-0.026	100	0.035	-0.069	150	0.049	-0.135

COLEMAN FUEL FLOW RATE ROTAMETER CHART

Value	Left	Right	Value	Left	Right	Value	Left	Right
1	-0.001	-0.008	51	-0.013	-0.043	101	-0.032	-0.125
2	-0.001	-0.009	52	-0.014	-0.044	102	-0.033	-0.128
3	-0.001	-0.009	53	-0.014	-0.045	103	-0.033	-0.131
4	-0.002	-0.010	54	-0.014	-0.046	104	-0.034	-0.134
5	-0.002	-0.010	55	-0.015	-0.047	105	-0.034	-0.137
6	-0.002	-0.011	56	-0.015	-0.048	106	-0.035	-0.140
7	-0.002	-0.011	57	-0.015	-0.049	107	-0.035	-0.143
8	-0.002	-0.012	58	-0.016	-0.050	108	-0.036	-0.146
9	-0.002	-0.013	59	-0.016	-0.051	109	-0.036	-0.149
10	-0.003	-0.013	60	-0.016	-0.052	110	-0.037	-0.153
11	-0.003	-0.014	61	-0.017	-0.054	111	-0.037	-0.156
12	-0.003	-0.014	62	-0.017	-0.055	112	-0.038	-0.160
13	-0.003	-0.015	63	-0.017	-0.056	113	-0.038	-0.163
14	-0.004	-0.016	64	-0.018	-0.057	114	-0.038	-0.167
15	-0.004	-0.016	65	-0.018	-0.058	115	-0.039	-0.170
16	-0.004	-0.017	66	-0.018	-0.059	116	-0.039	-0.174
17	-0.004	-0.018	67	-0.019	-0.061	117	-0.040	-0.178
18	-0.004	-0.018	68	-0.019	-0.062	118	-0.040	-0.182
19	-0.005	-0.019	69	-0.019	-0.063	119	-0.041	-0.186
20	-0.005	-0.019	70	-0.020	-0.065	120	-0.041	-0.190
21	-0.005	-0.020	71	-0.020	-0.066	121	-0.042	-0.195
22	-0.005	-0.021	72	-0.021	-0.067	122	-0.042	-0.199
23	-0.006	-0.021	73	-0.021	-0.069	123	-0.043	-0.203
24	-0.006	-0.022	74	-0.021	-0.070	124	-0.043	-0.208
25	-0.006	-0.023	75	-0.022	-0.072	125	-0.044	-0.213
26	-0.006	-0.023	76	-0.022	-0.073	126	-0.044	-0.217
27	-0.007	-0.024	77	-0.022	-0.075	127	-0.045	-0.222
28	-0.007	-0.025	78	-0.023	-0.076	128	-0.045	-0.227
29	-0.007	-0.026	79	-0.023	-0.078	129	-0.046	-0.232
30	-0.007	-0.026	80	-0.024	-0.080	130	-0.047	-0.237
31	-0.008	-0.027	81	-0.024	-0.081	131	-0.047	-0.242
32	-0.008	-0.028	82	-0.024	-0.083	132	-0.048	-0.248
33	-0.008	-0.028	83	-0.025	-0.085	133	-0.048	-0.253
34	-0.008	-0.029	84	-0.025	-0.087	134	-0.049	-0.259
35	-0.009	-0.030	85	-0.026	-0.089	135	-0.049	-0.265
36	-0.009	-0.031	86	-0.026	-0.091	136	-0.050	-0.270
37	-0.009	-0.031	87	-0.026	-0.093	137	-0.050	-0.276
38	-0.010	-0.032	88	-0.027	-0.095	138	-0.051	-0.282
39	-0.010	-0.033	89	-0.027	-0.097	139	-0.051	-0.289
40	-0.010	-0.034	90	-0.028	-0.099	140	-0.052	-0.295
41	-0.010	-0.035	91	-0.028	-0.101	141	-0.052	-0.301
42	-0.011	-0.035	92	-0.029	-0.103	142	-0.053	-0.308
43	-0.011	-0.036	93	-0.029	-0.105	143	-0.054	-0.315
44	-0.011	-0.037	94	-0.029	-0.108	144	-0.054	-0.321
45	-0.012	-0.038	95	-0.030	-0.110	145	-0.055	-0.328
46	-0.012	-0.039	96	-0.030	-0.112	146	-0.055	-0.335
47	-0.012	-0.040	97	-0.031	-0.115	147	-0.056	-0.343
48	-0.012	-0.041	98	-0.031	-0.117	148	-0.056	-0.350
49	-0.013	-0.041	99	-0.032	-0.120	149	-0.057	-0.358
50	-0.013	-0.042	100	-0.032	-0.123	150	-0.058	-0.365

References

Anderson, Gary. "Fundamental Physics of Micro Air Vehicles: Challenges and Opportunities." Mechanical Sciences DivisionUS Army Research Office (2005).

Annen, Kurt D., David B. Stickler, and Jim Woodroffe. "Glow Plug-Assisted HCCI Combustion in a Miniature Internal Combustion Engine (MICE) Generator." 44th AIAA Aerospace Sciences Meeting and Exhibit. Aerodyne Research, Inc., Billerica, MA 01821.

Annen, Kurt D., David B. Stickler, and Jim Woodroffe. "HIGH ENERGY DENSITY ELECTRIC POWER FOR UAV/UGV PROPULSION USING A MINIATURE IC ENGINE (MICE)." 2nd AIAA "Unmanned Unlimited" Systems, Technologies, and Operations (2003).

Astroflight. Bob Boucher. 02 July 2009 <http://www.astroflight.com>.

Bell, Lon E. "Alternate Thermoelectric Thermodynamic Cycles with Improved Power Generation Efficiencies." BSST, LLC.

Colozza, Anthony J. "Hydrogen Storage for Aircraft Applications Overview." NASA/CR?2002-211867.

Corum, J. M., R. L. Battiste, K. C. Liu, and M. B. Ruggles. "Basic Properties of Reference Crossply Carbon-Fiber Composite." Oak Ridge National Laboratory.

Dahm, Werner, Jun Ni, Kevin Mijit, James Mayor, George Qiao, Stephen W. Dyer, Anish G. Menjamin, Yongxian Gu, Yong Lei, and Melody L. Papke. "Micro

Internal Combustion Swing Engine (MICSE) for Portable Power Generation Systems." AIAA Aerospace Sciences Meeting (2002).

Demler, Roger. "Power for the Soldier: Small Engine Prospects." Foster-Miller Inc.

Diehl, G. M. Think Quiet.

DYNO-mite Dynamometer. 02 July 2009 <http://www.land-and-sea.com>.

Enduroflight Team. Design of a Sub-Scale Unmanned Aerial Vehicle.

Fairbanks, John. "DOE?s Launch of High-Efficiency Thermoelectrics Projects." Office of FreedomCAR and Vehicle Technologies Program. U.S. Department of Energy.

Fu, Kelvin, Aaron J. Knoblock, Fabian C. Martinez, David C. Walther, Carlos Fernandez-Pello, Al P. Pisano, Dorian Liepmann, Kenji Miyaska, and Kaoru Maruta. "DESIGN AND EXPERIMENTAL RESULTS OF SMALL-SCALE ROTARY ENGINES." ASME International Mechanical Engineering Congress and Exposition (2001).

Gerendas, Miklos, and Ralph Pfister. "Development of a Very Small Aero-Engine." ASME International Gas Turbine and Aeroengine Technical Congress and Exposition (2000).

Glassock, Richard, Jane Hung, Luis F. Gonzalez, and Rodney A. Walker. "Design, Modelling and Measurement of Hybrid Powerplant for Unmanned Aerial Systems (UAS)." 5th Australasian Congress on Applied Mechanics (2007).

Glassock, Richard R. "Multimodal Hybrid Powerplant for Unmanned Aerial Systems (UAS) Robotics." Australian Research Centre for Aerospace Automation.

Greenman, Matthew D. Design and Construction of a Miniature Internal Combustion Engine. Diss. Massachusetts Institute of Technology, 1996.

Halsey, David G., and David A. Fox. "Closed Brayton Cycle (CBC) Power Generation from an Electric Systems Perspective." Hamilton Sundstrand.

"High Performance Free-Piston Stirling Engines."

"High Power Lithium Ion ANR26650M1." A123Systems.

Huth, James, and Josh Collins. "Diesel Fuel-to-Electric Energy Conversion Using Compact, Portable, Stirling Engine-Based Systems." Japan Society of Mechanical Engineers (2007).

Huth, James, S. Y. Kim, Ezekiel Holliday, Andrew Buffalino, Alessandro Gomez, and Subir Roychoudhury. "DEVELOPMENT OF A WEARABLE JP8-FUELED SOLDIER POWER SOURCE."

Jiang, Joe-Air, Tsong-Liang Huang, Ying-Tung Hsiao, and Chia-Hong Chen. "Maximum Power Tracking for Photovoltaic Power Systems." Tamkang Journal of Science and Engineering 8 (2005): 147-53.

Jovanovic, Velimir, Daniel Krommenhoek, Saeid Ghamaty, and John Bass. "HIGH COEFFICIENT OF PERFORMANCE QUANTUM WELL THERMOELECTRIC NANO COOLER." Proceedings of IPACK2007.

Kushch, Aleksandr S., John C. Bass, Saeid Ghamaty, and Norbert B. Elsner. "Thermoelectric Development at Hi-Z Technology." Hi-Z Technology, Inc.

"Lithium Sulfur Rechargeable Battery Data Sheet." SION power inc.

Load Cell, Torque Sensor, Force Sensor, Pressure Sensor, Custom Load Cell & related instruments. 02 July 2009 <http://www.futek.com>.

Load Cells. 02 July 2009 <http://www.transducertechniques.com>.

"Logistics-Fueled, Man-Portable Generator Sets for Soldier Power, Battery Charging and APU Needs." International Soldier Systems Conference (2004).

Ludwiczak, Damian R., Dzu K. Le, Anne M. McNelis, Albert C. Yu, Sergey Samorezov, and Dave S. Hervol. "Validation of a 2 kWe Closed-Brayton-Cycle Power Conversion System Mechanical Dynamics Model."

Martini, William R. STIRLING ENGINE DESIGN MANUAL. 1978.

Menon, Shyam K. Performance measurement and scaling in small internal combustion engines. Thesis. 2006.

Menon, Shyam, Nathan Moulton, and Christopher Cadou. "Development of a Dynamometer for Measuring Small Internal-Combustion Engine Performance." JOURNAL OF PROPULSION AND POWER 23 (2007): 194-202.

"[Micro and Precision Engineering Research Group] Microturbine for electric power generation." [Departement Werktuigkunde] Home page Department Mechanical Engineering. 02 July 2009 <http://www.mech.kuleuven.be/micro/topics/turbine/>.

Misra, Ajay K. "Overview of NASA Program on Development of Radioisotope Power Systems with High Specific Power." 4th International Energy Conversion Engineering Conference and Exhibit (2006): 26-29.

National Research Council. Meeting the Energy Needs of Future Warriors.

Peirs, J., F. Verplaetsen, F. Norman, and S. Lefever. "Development of a Micro Gas Turbine For Electric Power Generation." Katholieke Universiteit Leuven.

Pengra, David B., and Thomas L. Dillman. "Notes on Data Analysis and Experimental Uncertainty."

Raine, Robert R., Keri Morle, and Gordon Otte. "A Cost-Effective Teaching and Research Dynamometer for Small Engines." Int. J. Engng Ed 18 (2002): 50-57.

Rogowski, A. R. Elements of Internal Combustion Engines. 1953.

Rudakevych, Pavlo, and Brian Yamauchi. "A man portable hybrid UAV/UGV system." IRobot.

Battery Specification Sheet Sanyo. 2003.

Shaltens, R. K., L. S. Mason, and J. G. Schreiber. "STIRLING RADIOISOTOPE POWER SYSTEM AS AN ALTERNATIVE FOR NASA?S DEEP SPACE MISSIONS." Innovative Approaches to Outer Planetary Exploration 2001?2020. NASA Glenn Research Center.

Sher, Eran, and Diana Levinzon. "Scaling-Down of Miniature Internal Combustion Engines: Limitations and Challenges." Heat Transfer Engineering 26 (2005): 1-4.

Shin, Younggy, Syng-ho Chang, and Sam-Ok Koo. "Performance test and simulation of a reciprocating engine for long endurance miniature unmanned aerial vehicles." Department of Mechanical Engineering, Sejong University, Seoul, South Korea. Smart UAV Systems Department, Korea Aerospace Research Institute, Daejeon, South Korea.

Slack, Glen A., and Moayyed A. Hussain. "The Maximum Possible Conversion Efficiency of Silicon Germanium Thermoelectric Generators." GeneraI Electric R&D Center (1991).

Sookdeo, Troy. PERFORMANCE MEASURMENT, SIMULATION, AND ANALYSIS OF THE COX TEE DEE 0.010, THE WORLD?S SMALLEST PRODUCTION INTERNAL COMBUSTION ENGINE. Thesis. 2006.

Taylor, Charles F. The Internal-combustion Engine In Theory And Practice. Vol. 1.

Tudron, Frank B., James R. Akridge, and Vincent J. Puglisi. "Lithium-Sulfur Rechargeable Batteries: Characteristics, State of Development, and Applicability to Powering Portable Electronics." Sion Power Corporation.

Vashaee, Daryoosh, and Ali Shakouri. "Improved Thermoelectric Power Factor in Metal-Based Superlattices." PH YSICAL REVIEW LETTERS 92 (2004).

Yoshida, Kazushi, Shigeaki Tomonari, Hirokazu Yoshioka, Shuji Tanaka, Daisuke Satoh, and Masayoshi Esashi. "HIGH ENERGY DENSITY MINIATURE ELECTRICAL AND THERMAL POWER SOURCE USING CATALYTIC COMBUSTION OF BUTANE." Matsushita Electric Works Ltd. Department of Mechanical and Precison Engineering, Tohoku University.

Yoshida, Kazushi, Shuji Tanaka, Shigeaki Tomonari, Daisuke Satoh, and Masayoshi Esashi. "High-Energy Density Miniature Thermoelectric Generator Using Catalytic Combustion." JOURNAL OF MICROELECTROMECHANICAL SYSTEMS 15 (2006): 195-203.

VITA

THOMAS CHADWICK HAYS

Candidate for the Degree of

Master of Science

Thesis: HIGH ENERGY DENSITY PROPULSION SYSTEMS AND SMALL ENGINE DYNAMOMETER

Major Field: Mechanical and Aerospace Engineering

Biographical:

Education:
Completed the requirements for the Master of Science in Mechanical and Aerospace Engineering at Oklahoma State University, Stillwater, Oklahoma in July, 2009.

Bachelor of Science in Mechanical and Aerospace Engineering from Oklahoma State University, Stillwater, Oklahoma
May 2007

Experience:
Six months experience with Lockheed Martin across two internships.

Name: Thomas C. Hays Date of Degree: July 2009

Institution: Oklahoma State University Location: Stillwater, Oklahoma

Title of Study: HIGH ENERGY DENSITY PROPULSION SYSTEMS AND SMALL ENGINE DYNAMOMETER

Pages in Study: 196 Candidate for the Degree of Master of Science

Major Field: Mechanical and Aerospace Engineering

Scope and Method of Study:

This study investigates all possible methods of powering small unmanned vehicles, provides reasoning for the propulsion system down select, and covers in detail the design and production of a dynamometer to confirm theoretical energy density calculations for small engines. Initial energy density calculations are based upon manufacturer data, pressure vessel theory, and ideal thermodynamic cycle efficiencies. Engine tests are conducted with a braking type dynamometer for constant load energy density tests, and show true energy densities in excess of 1400 WH/lb of fuel.

Findings and Conclusions:

Theory predicts lithium polymer, the present unmanned system energy storage device of choice, to have much lower energy densities than other conversion energy sources. Small engines designed for efficiency, instead of maximum power, would provide the most advantageous method for powering small unmanned vehicles because these engines have widely variable power output, loss of mass during flight, and generate rotational power directly.

Theoretical predictions for the energy density of small engines has been verified through testing. Tested values up to 1400 WH/lb can be seen under proper operating conditions. The implementation of such a high energy density system will require a significant amount of follow-on design work to enable the engines to tolerate the higher temperatures of lean operation. Suggestions are proposed to enable a reliable, small -engine propulsion system in future work. Performance calculations show that a mature system is capable of month long flight times, and unrefueled circumnavigation of the globe.

ADVISER’S APPROVAL: Dr. Andrew S. Arena